

1 **Title:** Glymphatic flow resistance in humans measured by multifrequency impedance dispersion

2
3 **Authors:** Paul Dagum, MD, PhD¹; Laurent Giovangrandi, PhD¹; Swati Rane Levendovszky,
4 PhD²; Jake J. Winebaum¹; Tarandeep Singh, MS¹; Yeilim Cho, MD³; Robert M. Kaplan, PhD⁴;
5 Michael S. Jaffee, MD⁵; Miranda M. Lim, MD, PhD^{6,7,8}; Carla Vandeweerd^{9,10}, PhD; Jeffrey J.
6 Iliff, PhD^{3,11,12}

7
8 **Affiliations:** ¹Applied Cognition Inc, Redwood City, CA; ²Department of Radiology, University of
9 Washington School of Medicine, Seattle, WA; ³VISN 20 NW Mental Illness Research, Education
10 and Clinical Center, VA Puget Sound Healthcare System, Seattle, WA; ⁴Clinical Excellence
11 Research Center, Stanford University School of Medicine, Stanford, CA; ⁵ Department of
12 Neurology, University of Florida Health, Gainesville, FL; ⁶VISN 20 Northwest Mental Illness
13 Research, Education and Clinical Center (MIRECC), VA Portland Health Care System,
14 Portland, OR; ⁷Neurology Service, Research Service, VA Portland Health Care System,
15 Portland, OR; ⁸Department of Neurology, Oregon Alzheimer’s Disease Research Center,
16 Oregon Health & Science University, Portland, OR; ⁹University of Florida Health Precision
17 Health Research Center, Clinical and Translational Science Institute, University of Florida,
18 Gainesville, FL; ¹⁰Health Outcomes and Biomedical Informatics, College of Medicine, University
19 of Florida, Gainesville, FL; ¹¹Department of Psychiatry and Behavioral Science, University of
20 Washington School of Medicine, Seattle, WA; ¹²Department of Neurology, University of
21 Washington School of Medicine, Seattle, WA;

22
23 **Corresponding Author:**
24 Paul Dagum, MD, PhD
25 Applied Cognition Inc
26 1629 Main St.
27 Redwood City, CA 94063
28 paul@appliedcognition.com
29 Ph: (415) 378-5456
30

31 **ABSTRACT**

32 Glymphatic function in animal models supports the clearance of brain proteins whose mis-
33 aggregation is implicated in neurodegenerative conditions including Alzheimer's and
34 Parkinson's disease. The measurement of glymphatic function in the human brain has been
35 elusive, limiting its potential in translational research. Here we described a non-invasive
36 multimodal device for the first-in-human continuous measurement of sleep-active glymphatic
37 flow resistance using repeated electrical impedance spectroscopy measurements through two
38 separate clinical validation studies. Device measurements successfully (i) paralleled sleep-
39 associated changes in extracellular volume that regulate glymphatic function, (ii) replicated
40 preclinical findings showing glymphatic function is increased with increasing sleep EEG delta
41 power, and is decreased with increasing sleep EEG beta power and heart rate, and (iii)
42 predicted glymphatic solute exchange measured by contrast-enhanced MRI. The present
43 investigational device permits the continuous and time-resolved assessment of glymphatic flow
44 resistance in naturalistic settings necessary to determine the contribution of glymphatic
45 impairment to risk and progression of Alzheimer's disease, and to enable target-engagement
46 studies that modulate glymphatic function in humans.

47 **Words 11957**

48 **Without methods 5467**

49

50

51

52

53 INTRODUCTION

54 The glymphatic system is a brain-wide network of perivascular pathways along which the
55 cerebrospinal fluid (CSF) surrounding the brain exchanges with brain interstitial fluid, supporting
56 nutrient distribution and waste clearance (**Figure 1a-b**). In animal models, glymphatic function
57 supports the clearance of amyloid beta^{1,2}, tau³⁻⁵, and alpha synuclein^{6,7}, whose mis-aggregation
58 is implicated in the pathogenesis of neurodegenerative conditions including Alzheimer's and
59 Parkinson's disease. Glymphatic function is further postulated to be a mechanism for volume
60 transmission of the neurotransmitters acetylcholine, serotonin and norepinephrine, and of
61 neurohormones regulating brain-body homeostasis⁸. While this system is foundational to brain
62 health and disease, measurement of glymphatic function in the human brain, principally by
63 magnetic resonance imaging (MRI), is conducted in only a handful of academic neuroimaging
64 centers⁹. Without a consistent, reproducible and accessible way of measuring this important
65 neurobiology in humans, the promise of developing therapeutic interventions that target
66 glymphatic function to treat and prevent neurological and psychiatric diseases remains elusive.

67
68 Studies in rodents have demonstrated that glymphatic function is more rapid during sleep
69 compared to the awake state^{2,10}. During periods of wakefulness, the interstitial space is narrow
70 and tortuous, forming a high-resistance pathway that suppresses glymphatic flow, while during
71 sleep fluid shifts from the intracellular compartment into the extracellular (interstitial) space,
72 widening these pathways, and enhancing glymphatic function by ~60% (**Figure 1c-d**).

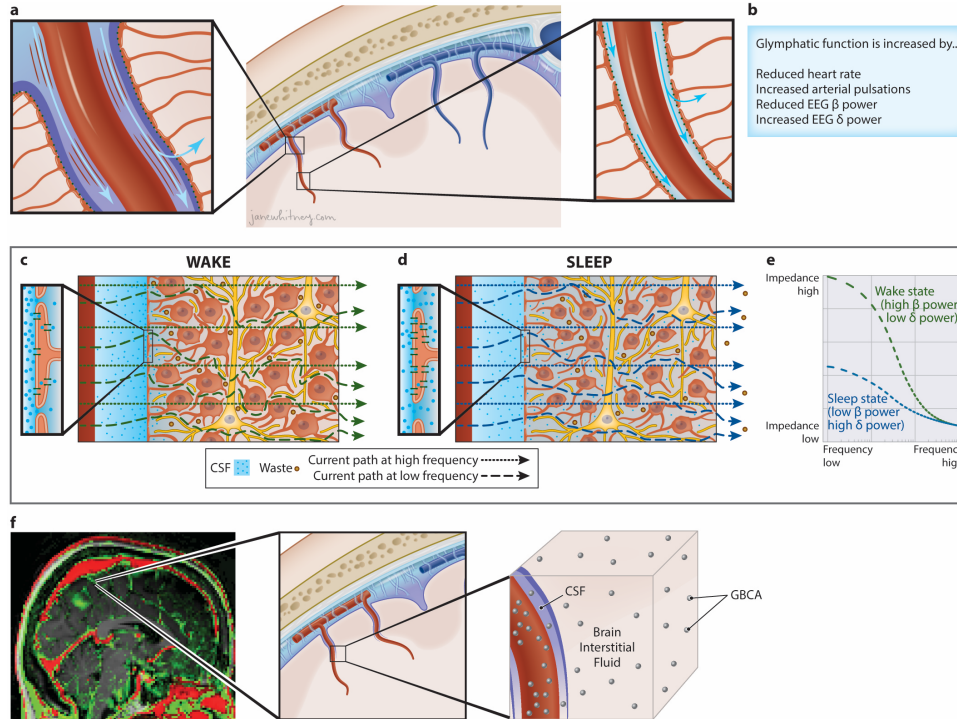
73 Measuring glymphatic function across a range of physiological conditions demonstrated that
74 faster glymphatic exchange is associated with increased electroencephalogram (EEG) delta
75 band power, decreased EEG beta power, and reduced heart rate¹¹. Studies utilizing contrast-
76 enhanced (CE)-MRI to measure solute exchange between the CSF and brain interstitial
77 compartments have confirmed in human participants more rapid glymphatic function during
78 sleep¹², although the poor temporal resolution of this approach¹³⁻¹⁵ has not permitted the

79 relationship between EEG or cardiovascular features and glymphatic function to be defined in
80 the human brain.

81
82 Electrical impedance spectroscopy (EIS) is widely used in medicine for body composition
83 analysis and for monitoring cellular changes in settings including tumors and edema¹⁶⁻¹⁹. When
84 alternating current is injected into tissue, at low frequencies the voltage drop depends primarily
85 on the resistive pathway of the extracellular (interstitial) fluid, while at high frequencies cell
86 membranes behave like capacitors allowing current to also pass relatively freely through the
87 intracellular space (**Figure 1c-e**). This frequency dependence is the β -dielectric dispersion of
88 the underlying tissue and its repeated measurement permits the detection of shifts in the
89 extracellular and intracellular distribution of water within tissue^{17,20}.

90
91 We propose that the biophysics of EIS can be leveraged to measure the fluid shift that occurs
92 with changes in sleep-active glymphatic function. Because intracranial volume is constant, any
93 change in this frequency dependence across repeated EIS measures reflects changes in the
94 resistance of the extracellular space, which is inversely proportional to the extracellular fluid
95 volume (**Figure 1c-e**). Within the brain, the extracellular compartment includes the brain
96 interstitial space (~16% of total volume) and a combination of CSF (~10%) and blood plasma
97 (~6%)²¹. Small diurnal fluctuations occur in blood volume and in the CSF compartments,
98 however these changes are small and offset one another across physiological states^{22,23}. In
99 contrast, sleep-wake differences in glymphatic function are associated with much larger shifts in
100 the intracellular and particularly interstitial volumes². Thus, sleep-wake changes in EIS
101 measures will be sensitized to changes in brain intracellular and interstitial volume, and EIS-
102 based measures of parenchymal resistance (R_P) may represent a novel approach to track
103 sleep-active glymphatic function.

104



105

106 **Figure 1. Detection of sleep-wake changes in glymphatic flow resistance by impedance**
 107 **spectroscopy.** **a**, Glymphatic function involves the influx of cerebrospinal fluid (CSF) influx along
 108 perivascular spaces (PVSs) surrounding penetrating arteries (center). Glymphatic flow is driven by
 109 arterial pulsations and vasomotor oscillations (right). Astrocytic endfoot processes create the barrier
 110 between the PVS and the brain parenchyma, with gaps allowing CSF to exchange through the brain
 111 interstitial space. The endfoot processes are studded with perivascular aquaporin-4 water channels
 112 that also enable water to move into the astrocytes and out to the interstitial space. **b**, Data from
 113 physiological studies in rodents suggest that glymphatic function is increased in conditions of
 114 reduced heart rate, increased vasomotor pulsations, reduced EEG beta power, and increased EEG
 115 delta power (Hablitz et al. 2019). **c**, The interstitial space is dynamically regulated. Under conditions
 116 of low EEG delta power and high EEG beta power common to the awake state, it is narrow and
 117 tortuous, forming a high-resistance pathway that suppresses glymphatic function. When alternating
 118 current is injected into the brain parenchyma, at low frequencies the current cannot penetrate the
 119 capacitive cell membranes and its propagation depends primarily on the resistive pathway of the
 120 interstitial fluid. At high current frequencies, the current readily penetrates the capacitive cell
 121 membranes and its propagation depends on the resistance of the total tissue volume. This frequency
 122 difference is the β -dielectric dispersion of the underlying tissue. If the intracranial volume is constant,
 123 a change in the dielectric dispersion reflects a change in the low-frequency resistance pathway of
 124 the interstitial fluid. **d**, Under high EEG delta power and low EEG beta power common to the sleep
 125 state, fluid shifts from the intracellular compartment into the interstitial space, enhancing glymphatic
 126 function by ~60% in rodent studies (Xie et al. 2013). This widening of interstitial pathways reduces
 127 the current resistance at low-frequencies which reduces the measured dielectric dispersion. **e**, An
 128 impedance-frequency graph shows the change in dielectric dispersion between the two sleep/wake
 129 EEG states. The change in glymphatic flow resistance between these two states is inversely
 130 proportional to the relative change in the dielectric dispersion. **f**, Contrast-enhanced MRI following
 131 intravenous gadolinium-based contrast agent (GBCA) injection shows vascular regions that enhance
 132 immediately ($t=30$ min) upon GBCA injection (red), and CSF and brain parenchymal regions that
 133 enhance late ($t=3$ hrs) after leakage of GBCA first into the CSF and thence into the brain interstitium
 134 (green). A given MRI voxel includes GBCA within the blood, CSF and brain interstitial fluid
 135 compartments.

136

137

138 We developed a wearable investigational device (**Figure 2a-f**) that overcomes several technical
139 challenges surrounding the implementation of EIS as a measure of glymphatic flow resistance.

140 To define the dynamic relationship between R_P , sleep EEG features, and cardiovascular

141 parameters through the course of an overnight period, EIS measurements must be made with

142 high accuracy and temporal resolution. The investigational device performs measurements at

143 frequencies between 1kHz and 256kHz and has a ~3% measurement error in R_P

144 (**Supplemental 4**) enabling it to detect small changes in dispersion between repeated

145 measures. It is important to ensure that device measurements are not affected by changes in

146 electrode impedances that can occur over time, including those caused by the effects of motion

147 on the electrode-skin interface. A non-traditional four-electrode impedance configuration was

148 used with multiple excitation and sense configurations in combination with low-impedance, non-

149 polarizable electrodes. This ensured high-fidelity measurements including at low frequencies

150 due to the reduced sensitivity to motion artifacts, low noise, and stability of the skin-gel-

151 electrode interface. A signal processing approach enabled identification of signal from noise

152 using the real and imaginary parts of the impedance to establish if the measured response is

153 related to the excitation signal or has been distorted by artifact. The device further integrated

154 shielded cables to reduce effects of electromagnetic interferences, both external and internal to

155 the device, and the design minimized stray capacitances affecting higher frequencies. The

156 device is described in more detail in **Methods** and **Supplemental Information** including

157 **Supplemental Figure 2, Supplemental Figure 3** and **Supplemental Tables 7 – 12**. We note

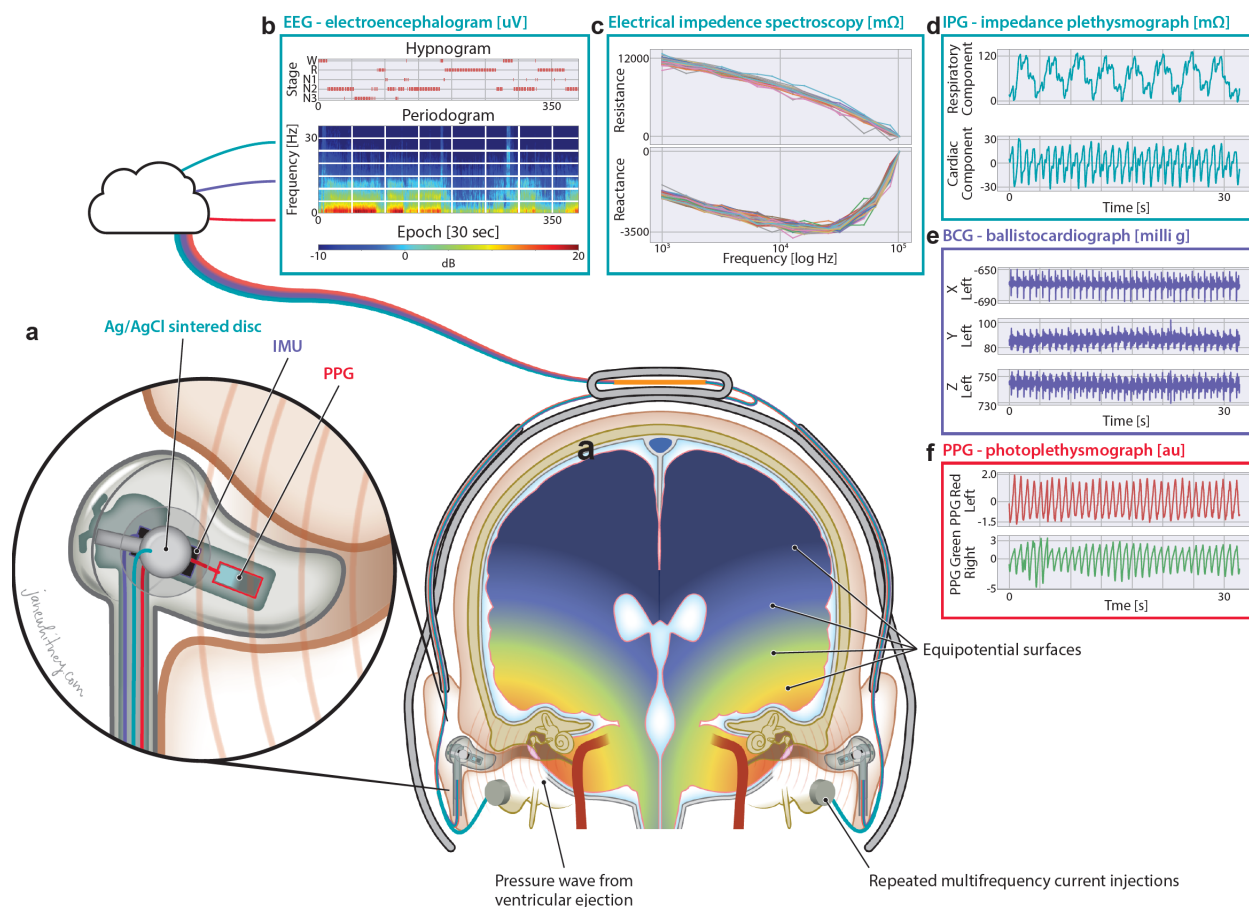
158 that glymphatic flow is determined by the parenchymal resistance to flow and the motive force

159 driving CSF along the perivascular spaces (PVS) into the interstitial compartment. The

160 resistance measured by the device is transcranial with a high temporal resolution of changes in

161 global intracellular to interstitial fluid shifts.

162



163

164 **Figure 2. Technical schematic of investigational device and its output signals.** Data for
 165 this study was acquired with a non-invasive multimodal skin-interfaced wireless device for
 166 continuous measurement of brain parenchymal resistance using repeated electrical impedance
 167 spectroscopy EIS time-multiplexed with EEG and cardiovascular measurements. EEG
 168 differential measurements were made between the two in-ear electrodes and a left mastoid was
 169 used to drive the common mode. These electrodes were shared with the EIS and the two
 170 measurements were time-multiplexed with a pair of analog multiplexers that decoupled EEG
 171 and EIS. The transcranial multi-frequency alternating current injections created an electric field
 172 through the brain and orthogonal equipotential surfaces. **a**, Each in-ear electronics housed PPG
 173 and IMU sensors. **b**, Data from the sensors were stored on the device's FLASH memory and
 174 transferred via a USB port to a cloud signal processing pipeline for offline analysis. Data from a
 175 participant visit is shown, which includes the device EEG periodogram and hypnogram. **c**, The
 176 EIS resistance and reactance frequency plots for this participant reveal an approximate 2000
 177 mOhm change in the dielectric dispersion during the sleep visit. **d**, The IPG respiratory and
 178 cardiac impedance variations are 120 mΩ and 50 mΩ, respectively. **e**, Cardiac ejection of blood
 179 is detected by the in-ear IMUs in the ballistocardiogram. The J peak of the ballistocardiogram
 180 marks the aortic valve opening. **f**, Time delay between the ballistocardiogram and in-ear PPG
 181 measures the pulse-transit time (PTT) to the that ear.

182

183

184 **RESULTS**

185 Data were acquired using the investigational medical device developed by Applied Cognition
186 Inc^{24,25}. Transcranial impedance dispersion is estimated from each EIS measure using a
187 dielectric relaxation model. In addition to EIS measurements, the device measures EEG,
188 photoplethysmogram (PPG), impedance plethysmogram (IPG) and head motion (**Figure 2a-f**).
189 We propose that the change in transcranial impedance dispersion, which we will henceforth
190 term parenchymal resistance R_P ($R_P = R_0 - R_\infty$), reflects shifts in brain intracellular and
191 interstitial compartment fluid volumes that underlie changes in glymphatic function (**Figure 1c-**
192 **e**). **Supplemental 3** contains an intuitive justification of the physiological connection between
193 EIS change and changes in glymphatic function. To test this, we evaluated whether R_P
194 measured with this device in human participants aligned with the central features of glymphatic
195 function described in rodent models^{2,11}.

196

197 ***Study Design***

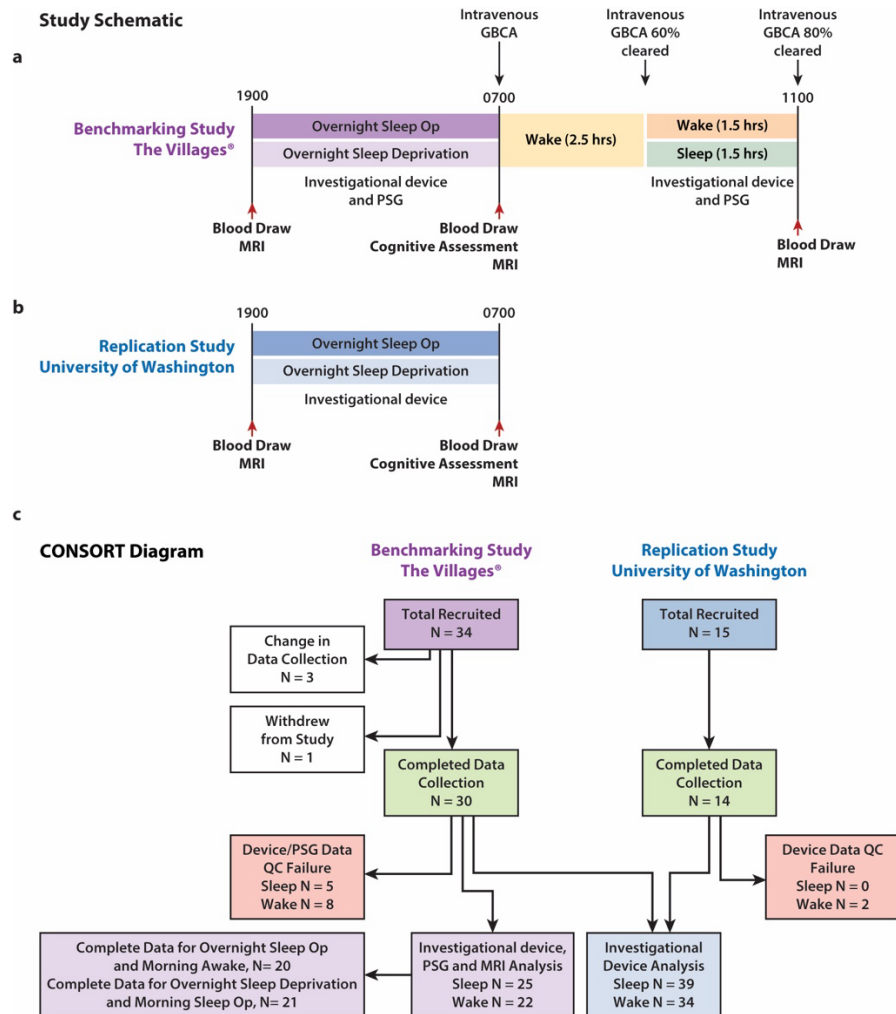
198 We conducted two clinical studies (denoted as “Benchmarking Study” and “Replication Study”)
199 to validate the performance of the device’s R_P measure as a surrogate of glymphatic flow
200 resistance during sleep and wake (**Figure 3**, top). Both studies were cross-over trials where
201 participants wearing the investigational device were subjected to one night of natural sleep and
202 one night spent awake, separated by two or more weeks. The Benchmarking Study was
203 conducted in The Villages® community, an active-lifestyle senior living community in Central
204 Florida where the University of Florida maintains a satellite academic research center, The
205 University of Florida Health Precision Health Research Center (UF Health PHRC). The
206 Benchmarking Study was designed to define the effect of sleep on overnight R_P measurements,
207 as well as the relationship between R_P and glymphatic function. It included overnight device
208 recordings, overnight gold-standard polysomnography (PSG), and morning contrast-enhanced
209 magnetic resonance imaging (CE-MRI) following intravenous gadolinium-based contrast agent

210 (GBCA) administration as a measure of glymphatic function. During the morning period,
211 following pre-contrast MRI scanning, GBCA injection, and immediate post-contrast MRI
212 scanning (totaling 2.5 hours spent awake), participants that were sleep deprived overnight were
213 provided a 1.5 hr sleep opportunity prior to the final MRI scan, while those that slept normally
214 overnight were kept awake during the 1.5 hr period (**Figure 3**, top). We evaluated whether, as
215 predicted from prior rodent studies on the sleep-modulation of glymphatic function^{2,11}, **a)** R_P is
216 reduced in sleeping compared to awake participants, **b)** whether reduced R_P is associated with
217 more rapid CSF-brain interstitial solute exchange measured by CE-MRI, **c)** whether R_P is
218 associated with increasing sleep EEG delta power and decreasing sleep EEG beta power, and
219 **d)** whether reduced R_P is associated with decreasing heart rate. The Replication Study
220 conducted at the University of Washington did not include overnight PSG or morning CE-MRI
221 and had as a primary outcome confirming the effect of sleep state on device-measured R_P , and
222 secondary outcomes confirming the associations between R_P and sleep stages, heart rate, and
223 EEG spectral band power. As noted in the detailed study description in the Methods section,
224 these studies also evaluated novel non-contrast MRI measures of glymphatic function, sleep-
225 sensitive changes in cognitive function, and sleep-sensitive changes in plasma Alzheimer's
226 disease biomarkers across a range of physiological sleep conditions. Those findings will be
227 reported elsewhere.

228

229 **Inclusion and Exclusion Criteria**

230 All studies were performed between October 2022 – June 2023 and were reviewed and
231 approved by University of Florida Institutional Review Board (IRB No. 202201364,
232 Benchmarking Study) and Western Institutional Review Board (IRB No. 20225818, Replication
233 Study). The studies have been registered at ClinicalTrials.gov
234 (<https://clinicaltrials.gov/study/NCT06222385> and <https://clinicaltrials.gov/study/NCT06060054>).
235 Written informed consent was obtained from all study participants during a screening visit, prior



236
237
238
239
240
241
242
243
244
245
246
247
248
249
250
251
252
253
254
255
256

Figure 3. Study schematic and CONSORT diagram for Benchmarking Study and Replication Study. **a**, The Benchmarking Study conducted at The Villages® was designed to define the relationship between parenchymal resistance (R_P) and glymphatic function. Reported here are the overnight and morning device recordings, overnight and morning gold-standard polysomnography (PSG), and morning contrast-enhanced magnetic resonance imaging (CE-MRI) following intravenous gadolinium-based contrast agent (GBCA) administration as a measure of glymphatic function. Primary and secondary outcome data not reported here included blood analysis of amyloid β and tau levels, cognitive assessment, and non-contrast MRI. **b**, The Replication Study conducted at the University of Washington had a primary outcome of confirming the effect of sleep state on device-measured R_P , and secondary outcomes of confirming the associations between R_P and sleep stages, heart rate, and EEG spectral band power. The Replication Study also included secondary outcomes on blood analyses for amyloid β and tau levels, cognitive assessment and non-contrast MRI. **c**, The Benchmarking Study enrolled 34 participants of which 30 completed both visits. Three were censored due to changes in device data collection and sensor locations. One withdrew following the first MRI scan. Of the 30 that completed the study, 5 overnight sleep visits and 8 overnight wake visits failed the data quality control (QC) criteria to provide sufficient artifact free data to yield results. This resulted in 25 sleep and 22 wake device, PSG and MRI complete data sets. Of these, 20 sleep and 21 wake device participants had complete data from both the overnight and morning sleep/wake periods. The Replication Study enrolled 14 participants. All 14 completed the study, of which 3 wake visits failed the data QC criteria and no sleep visit failed. (sleep op, sleep opportunity)

257 to any study activities. Studies were carried out in accordance with the principles of the Belmont
258 Report. The Benchmarking Study enrolled 34 healthy participants 56-66 years of age. The
259 Replication Study enrolled 14 healthy participants 49-63 years of age. Participants were
260 excluded if they had cognitive impairment or clinical depression. Cognitive impairment was
261 assessed using the Montreal Cognitive Assessment²⁶ (MoCA, 28.1 +/- 1.2; range 26, 30) and
262 depression was evaluated using the 15-item Geriatric Depression Scale²⁷ (GDS, 0.7 +/- 1.1;
263 range 0, 4). Participants with a self-reported history of diabetes, hypertension, coronary artery
264 disease, pulmonary disease, neurological disease, depression or anxiety were also excluded
265 from the study, as were participants planning travel to alternate time zones within two weeks of
266 study participation. Participant demographics, MoCA and GDS scores are listed for each study,
267 and for the combined dataset in **Supplemental Table 1**.

268
269 A Consolidated Standards of Reporting Trials (CONSORT) diagram for the Benchmarking Study
270 and Replication Study is provided in **Figure 3** (bottom). Within the Benchmarking Study, the first
271 three participants were removed from analysis because of a design change in the
272 investigational device sensor positions. One participant was unable to complete the first MRI
273 session and withdrew from the study. Of the remaining 30 participants (61.8 ± 2.7 years of age;
274 14 female, 16 male) that completed the Benchmarking Study, five overnight sleep studies and
275 eight overnight wake studies failed data quality control due to excessive artifacts in the
276 recordings, leaving 25 overnight sleep studies and 22 overnight wake studies in the
277 Benchmarking Study with complete device, PSG and MRI data. Excessive movement artifacts
278 during the morning recording periods resulted in the exclusion of data from five additional
279 morning wake and one additional morning sleep opportunity periods, leaving 20 overnight
280 sleep/morning wake and 21 overnight wake/morning sleep opportunity datasets with complete
281 overnight and morning data. All participants enrolled in the Replication Study (55.6 ± 4.6 years

282 of age; 7 female, 7 male) completed the protocol. All overnight sleep data were usable, but
283 three overnight wake studies were removed, two because of excessive artifact and one because
284 of non-compliance with the wake protocol. The higher number of quality control failures in the
285 Benchmarking Study was largely due to the physical challenges caused by simultaneous data
286 acquisition from both PSG and investigational device on the same night. Note that when the
287 investigational device was used in the absence of PSG in the Replication Study, quality control
288 failures were less frequent and restricted to motion artifacts in the awake condition.

289

290 ***Assessment of sleep and wake changes in parenchymal resistance***

291 Study participants underwent one night of normal sleep and one night of sleep deprivation
292 separated by 2-4 weeks. Sleep/wake or wake/sleep visit order was determined by random
293 assignment following informed consent. In the Benchmarking Study, sleep and wake status was
294 confirmed by PSG with anticipated differences in rapid eye movement (REM), and non-REM
295 (NREM: N1, N2, N3) sleep stages observed between sleep and wake conditions. Similar
296 differences were observed in the Replication Study, in which investigational device-based EEG
297 was used to evaluate sleep parameters. EEG was assessed with the investigational device in
298 both the Benchmarking and Replication Studies; these measures were used when combining
299 EEG parameters between both studies. Averaged hypnograms showing sleep stage distribution
300 throughout the overnight sleep period for the Benchmarking and Replication Studies are shown
301 in **Figure 4a-b** (top), respectively. The averaged hypnogram for the overnight and morning
302 periods for the Benchmarking study participants with complete data during both periods is
303 shown in **Figure 4c** (left).

304

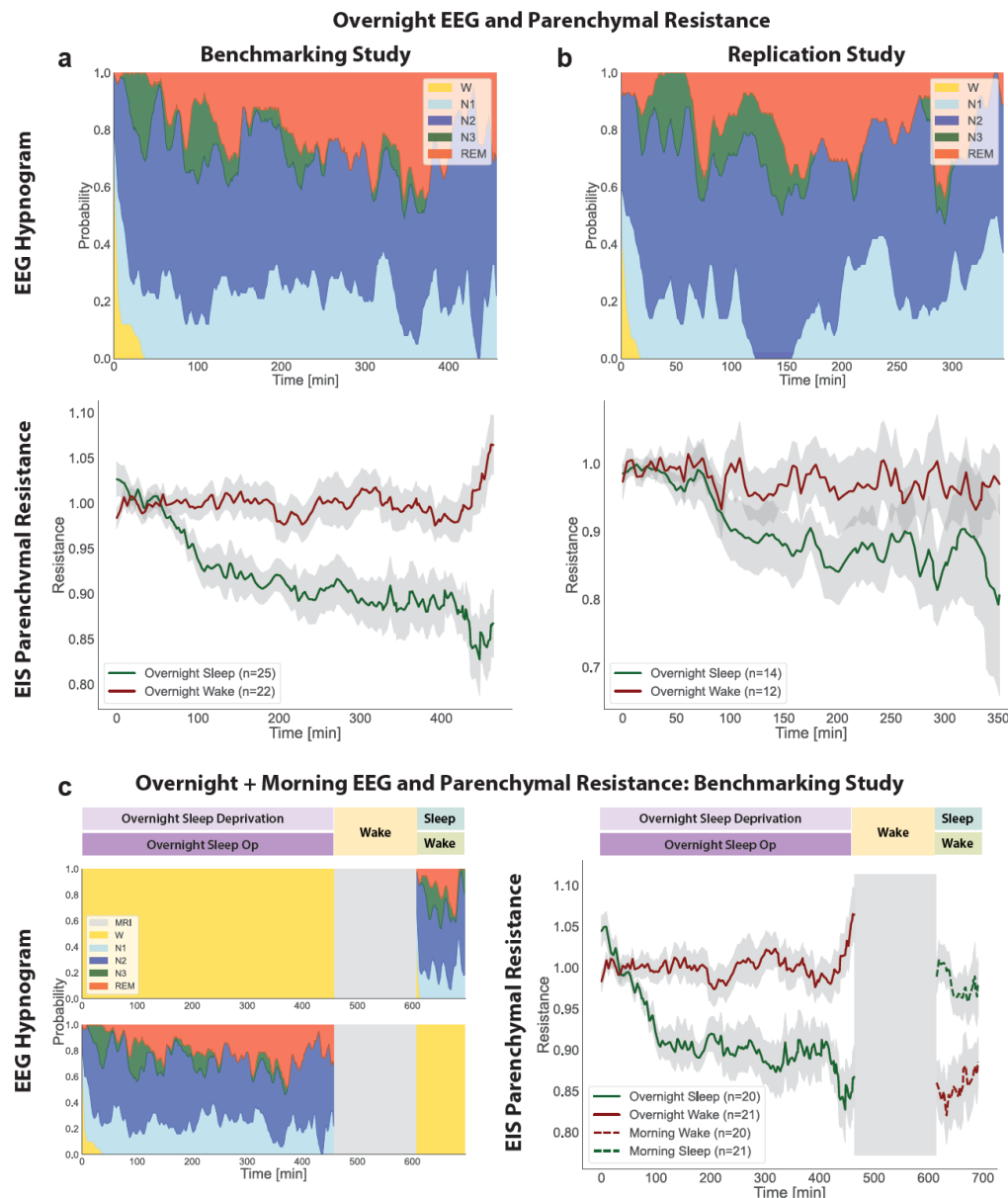
305 During the overnight period R_P was continuously monitored. The results from the Benchmarking
306 Study are provided in **Figure 4a** (bottom), which depicts the mean and standard errors of
307 overnight R_P . Each participant's R_P was normalized to the R_P at onset of the observation period,

308 and linear interpolation was used for missing R_P values within each participant. Compared to the
309 wake condition, overall R_P during sleep was reduced by 8% (Wake 1.00 ± 0.06 , Sleep $0.92 \pm$
310 0.06 , T-test $p < 0.001$). When evaluated through the course of the overnight period, the R_P
311 during the wake period remained largely constant. In contrast, during the sleep period the mean
312 R_P decreased monotonically, reaching at the end of the sleep period a nadir $\sim 20\%$ lower than at
313 onset or under the awake condition. Similar results were observed the Replication Study
314 (**Figure 4b**, bottom). Within the Benchmarking study, participants that were sleep deprived
315 overnight received a 1.5 hr sleep opportunity in the morning. Over this period, R_P began at a
316 higher value (resulting from overnight sleep deprivation) but declined over the 1.5 hr sleep
317 opportunity (**Figure 4c**, right). Among participants that slept overnight but were kept awake in
318 the morning, R_P during the morning period began at a low value (resulting from overnight sleep)
319 but increased over the 1.5 hr period of wakefulness. These data demonstrate across two study
320 populations that R_P remains constant or increases during periods of waking but declines steadily
321 through periods of sleep.

322

323 ***Association between sleep parameters and glymphatic function***

324 Following the overnight sleep periods, participants in the Benchmarking Study underwent CE-
325 MRI for the assessment of glymphatic function. Beginning at 7am, participants underwent a pre-
326 contrast T1-weighted MRI scan, received intravenous GBCA (Gadavist, 0.1 mmol/kg), followed
327 by T1-weighted MRI scans at 7-10 min (T_{10}) and 240 min (T_{240}) post-injection. We evaluated
328 contrast enhancement in eight regions of interest (ROIs): frontal cortical gray and white matter,
329 parietal cortical gray and white matter, temporal cortical gray and white matter, and occipital
330 gray and white matter. Contrast enhancement at the T_{10} time point primarily reflects GBCA
331 within the blood column, while enhancement at the T_{240} time point reflects GBCA leakage into
332 the cerebrospinal fluid (CSF) and into the brain interstitial compartments^{14,15}. Glymphatic
333 function was defined by measuring brain parenchymal contrast enhancement, the % change in



334
 335 **Figure 4. Brain parenchymal resistance is reduced periods of sleep.** **a.** Averaged EEG hypnograms
 336 from the sleep condition are shown for the overnight period of the Benchmarking Study with WASO
 337 excluded in both the hypnograms and sleep R_P (top). Over that period, parenchymal resistance (R_P ,
 338 bottom) remained constant during the awake state (red) but declined gradually in the sleep state (green).
 339 **b.** Similar trends were observed in the Replication Study. **c.** During the morning period of the
 340 Benchmarking Study, participants underwent a 1.5 hr sleep opportunity or period of wakefulness.
 341 Averaged EEG hypnograms for the overnight and morning periods are shown at left. At right, during the
 342 morning awake period, R_P increased gradually (dashed red), while it declined gradually during the sleep
 343 state (dashed green). Parenchymal resistances R_P shown **(a)**, **(b)** and **(c)** are the average across the
 344 participants after normalizing each participant's R_P measurements by their value at onset of the sleep or
 345 wake period. R_P in **(c)** for morning wake is plotted starting at the ending value of overnight R_P for
 346 illustration purposes. Standard error of the means are shown for each plot in light grey. The combined
 347 overnight and morning Benchmarking Study **(c)** includes participants who's overnight and morning data
 348 passed quality controls.
 349

350 T1-weighted signal intensity between 10-240 min post-GBCA injection ($100\% * (T_{240}-T_{10})/T_0$) within each
351 ROI.
352

353 To evaluate different sleep-related contributions to glymphatic function, we developed a general
354 random intercept mixed model with eight ROI groups fit to the T_{10} - T_{240} change in brain
355 parenchymal enhancement. Our **null hypothesis** was that parenchymal contrast, including
356 contrast in the interstitial compartment, was not influenced by sleep variables. Glymphatic
357 function supports the movement of solutes into and out of the brain interstitial compartment, yet
358 brain parenchymal enhancement includes contrast signal from the blood compartment (the
359 initial source of the GBCA) and the CSF compartment (the intermediate space linking the blood
360 and brain interstitium) in addition to the interstitial compartment (**Figure 1f**). Thus, we defined
361 the **null model** to include regressors for vascular and CSF contrast in the mixed model: the T_{10} -
362 T_{240} change in blood signal within the internal carotid artery, and the T_{10} - T_{240} change in CSF
363 signal within the cerebral lateral ventricles. We also included the confounding biological
364 variables of age, gender, and APOE $\epsilon 4$ status in the null model *shown in Supplemental*
365 *(bottom)*. The analyses of EEG powerbands, heart rate and sleep staging were performed on
366 the overnight sleep period recordings. Pulse plethysmography and EEG were acquired
367 concurrently and heart rate, EEG powerbands, sleep stage durations (REM; N1, N2, N3
368 NREM), number of awakenings and wake after sleep onset (WASO) were computed and
369 included independently in the null model (**Supplemental Table 2**), and likelihood ratio tests
370 used to compare the individual predictor model with the null model. Relative EEG delta, theta,
371 alpha and beta powerbands were each expressed as the overnight mean of the powerband
372 normalized to the average powerband value of the first three sleep epochs. Higher EEG delta
373 power (mean 19.12, 95% CI 5.4819, 32.7599; $P=0.0072$), lower EEG alpha (mean -7.28, 95%
374 CI -12.2638, -2.2935; $P=0.0052$) and beta (mean -5.33, 95% CI -7.7859, -2.8728; $P<0.001$)
375 power were significantly associated with greater contrast enhancement. We next evaluated
376 EEG-derived sleep stages within individual mixed models. Neither number of awakenings during

377 the sleep period, nor wake after sleep onset (WASO) were associated with parenchymal
378 contrast enhancement. Lower N1 sleep time was significantly associated with greater
379 parenchymal contrast enhancement (mean -0.1274, 95% CI -0.2130, -0.0420; $P=0.0043$), while
380 N2, N3 and REM sleep time had no significant association with parenchymal enhancement
381 within these individual models (**Supplemental Table 2**). Thus, within individual mixed models,
382 increased overnight EEG delta band power, reduced alpha and beta band power, and reduced
383 time in N1 sleep are each associated with greater glymphatic function, each rejecting the null
384 hypothesis that parenchymal contrast was not influenced by sleep variables (**Supplemental**
385 **Table 2**).

386

387 ***Direct association between parenchymal resistance and glymphatic function***

388 The device R_p values were computed repeatedly throughout the overnight sleep period from
389 each EIS scan. During sleep recordings, the R_p was non-stationary, decreasing throughout the
390 night as shown in **Figure 4a-c**. We observed that lower overnight R_p was significantly
391 associated with higher glymphatic contrast enhancement (mean -38.08, 95% CI -61.34805, -
392 14.8115; $P=0.0018$, **Supplemental Table 2**).

393

394 ***Combined effects of overnight parenchymal resistance, EEG spectral power, and heart*** 395 ***rate on glymphatic function***

396 We next utilized a comprehensive mixed model to define the contributions of R_p , EEG spectral
397 band power, and heart rate to parenchymal contrast enhancement. As in the individual mixed
398 models above, this comprehensive model extended the null model that contains only contrast
399 enhancement in the blood and cerebral ventricles as regressors, and age, APOE4 status, and
400 gender as confounding biological variables. We evaluated the relative delta, theta and beta
401 powerbands, omitting the alpha powerband to avoid multicollinearity in the model. We subjected
402 the model to a backward elimination algorithm with a Wald's p-value threshold of 0.05. **Table 1**

403 provides the full outputs of the analyses for each of the four intervention periods of overnight
404 sleep opportunity, morning sleep opportunity, overnight sleep deprivation and morning awake of
405 the study (**Figure 3**, top).

406

407 In reference to the models selected by backward elimination shown in **Table 1**, as expected,
408 both blood and ventricular CSF contrast enhancement were strongly associated with
409 parenchymal enhancement following the overnight sleep opportunity (blood mean 8.89; 95% CI
410 3.62, 14.16; $P = 0.001$; CSF mean 170.45; 95% CI 143.86, 197.04; $P < 0.001$) and overnight
411 sleep deprivation (blood mean 13.09; 95% CI 7.09, 19.10; $P < 0.001$; CSF mean 162.36; 95%
412 CI 129.54, 195.19; $P < 0.001$). For the overnight sleep opportunity, lower heart rate (mean -
413 54.48, 95% CI -79.51, -29.45; $P < 0.001$) and lower R_p (mean -52.55, 95% CI -74.76, -33.33;
414 $P < 0.001$) predicted greater contrast enhancement. Reduced EEG beta power predicted greater
415 parenchymal enhancement (mean -6.29, 95% CI -8.54, -4.05; $P < 0.001$), while neither delta nor
416 theta power exhibited significant associations within the multivariate model. In the overnight
417 sleep deprivation condition, reduced EEG delta power (mean -20.77, 95% CI -34.34, -7.20; $P =$
418 0.004) and increased theta power (mean 7.89, 95% CI 1.13, 14.64; $P = 0.026$) predicted greater
419 parenchymal enhancement, while neither beta power, heart rate nor R_p showed significant
420 associations within the multivariate model.

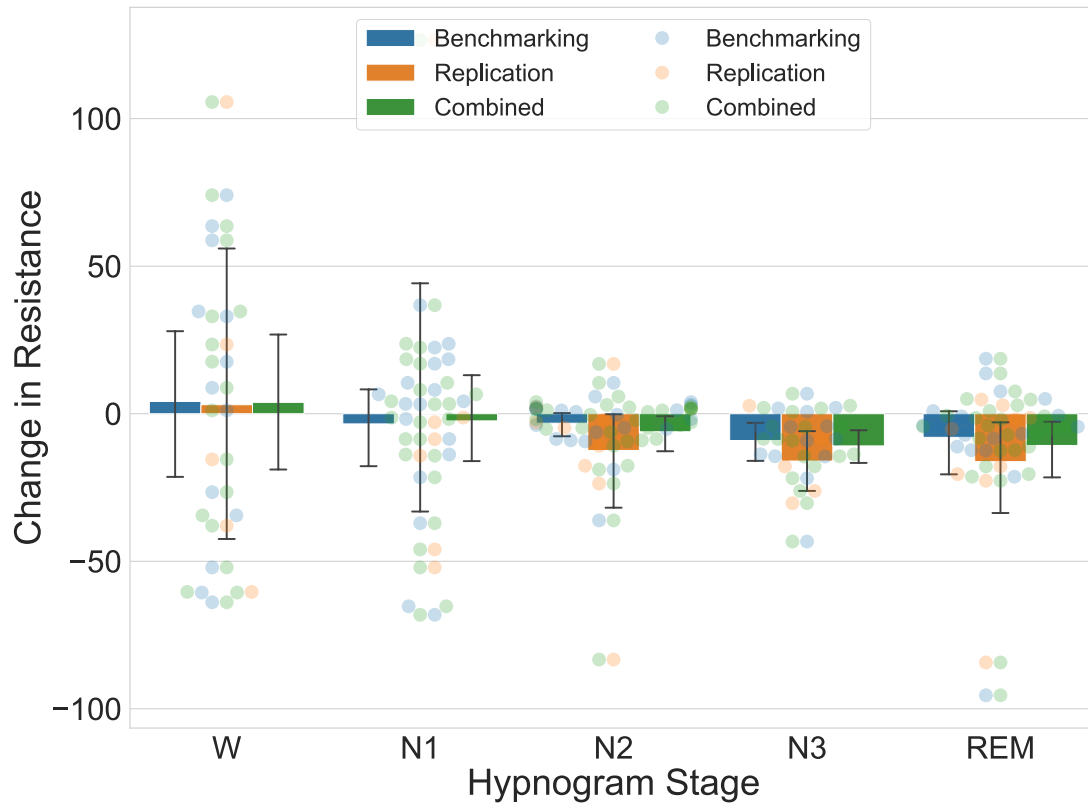
421

422 ***Combined effects of morning parenchymal resistance, EEG spectral power, and heart***
423 ***rate on glymphatic function***

424 As shown in the study schematic (**Figure 3**, top), between 7:10 am and 9:30am (140 min post-
425 injection, T_{140}) participants underwent MRI scanning followed by instrumentation with the
426 investigational device and PSG for the morning sleep opportunity or awake intervention.

427 Because the mean terminal half-life of intravenous GBCA in adults with normal renal function is

428



429
430 **Figure 5. Effect of sleep stages on R_P .** The mean first-order difference ΔR_P is shown by sleep
431 stage and study for the overnight sleep period with 95% confidence intervals. During N2, N3
432 and REM sleep ΔR_P is negative for each study and when combined reaches significance.
433 Benchmarking N2 (mean -3.21, 95% CI -9.07, -0.33; $P = 0.113$), N3 (mean -9.07, 95% CI -
434 17.04, -3.75; $P = 0.005$), REM (mean -8.01, 95% CI -25.64, -1.18; $P = 0.133$). Replication N2
435 (mean -12.46, 95% CI -34.94, -1.49; $P = 0.115$), N3 (mean -16.04, 95% CI -25.32, -5.32; $P =$
436 0.002), REM (mean -16.24, 95% CI -42.19, -4.65; $P = 0.065$). Combined N2 (mean -6.10, 95%
437 CI -14.78, -1.71; $P = 0.04$), N3 (mean -10.91, 95% CI -17.35, -5.93; $P < 0.001$), REM (mean -
438 10.75, 95% CI -23.86, -3.91; $P = 0.023$). Units of ΔR_P are $m\Omega$.
439
440

441 109 min²⁸, the post-injection blood contrast during the morning recordings was 60% cleared by
442 T₁₄₀ and 80% cleared by T₂₄₀. Glymphatic function in the period between T₁₄₀ and T₂₄₀, would
443 therefore dilute existing parenchymal contrast with CSF having 60% to 80% lower contrast
444 concentration, a process analogous to ‘clearance’ of interstitial contrast. Thus, we would expect
445 that an increase in glymphatic function during the period between T₁₄₀ and T₂₄₀ would be
446 reflected as reduced parenchymal contrast enhancement at T₂₄₀ (**Supplemental Figure 1**).

447

448 In reference to the models selected by backward elimination in **Table 1**, once again both blood
449 and ventricular CSF contrast enhancement were strongly associated with parenchymal
450 enhancement following the morning sleep opportunity (blood mean 11.73; 95% CI 7.89, 15.57;
451 P < 0.001; CSF mean 145.25; 95% CI 125.08, 165.42; P<0.001) and awake intervention (blood
452 mean 9.83; 95% CI 5.37, 14.29; P < 0.001; CSF mean 232.52; 95% CI 210.27, 254.77;
453 P<0.001). During the morning sleep opportunity, R_P begins to decrease (**Figure 4c**). Higher
454 EEG delta power (mean -35.94, 95% CI -44.10, -27.78; P < 0.001) and lower R_P (mean 55.35,
455 95% CI 33.01, 77.70; P < 0.001) predicted reduced parenchymal enhancement (greater
456 contrast clearance).

457

458 During the morning awake period, R_P increases from its overnight sleep ending level (**Figure**
459 **4c**). During this intervention, higher EEG delta power (mean -20.98, 95% CI -30.19, -11.77; P <
460 0.001), theta power (mean -15.27, 95% CI -19.51, -11.03; P < 0.001) and beta power (mean -
461 21.38, 95% CI -24.34, -18.43; P < 0.001) predicted greater contrast clearance as did lower heart
462 rate (mean 235.70, 95% CI 201.64, 269.76; P < 0.001) and lower R_P (mean 29.38, 95% CI 5.63,
463 53.13; P < 0.021). These findings are similar to those observed for the morning sleep
464 opportunity and consistent with the explanation that an increase in glymphatic influx of CSF
465 during this period dilutes the ISF contrast concentration and reduces the T₂₄₀ MRI signal
466 intensity.

Table 1. Multivariate models of brain parenchymal contrast enhancement using R_p, HR and EEG power band predictors.

Predictor Period	Fixed Effect Predictors	Full Model			Selected Model			Bootstrap Analysis			
		Estimate	CI	p	Estimate	CI	p	Bootstrap Inclusion Frequency (%)	RMSD Ratio	Relative Conditional Bias (%)	Bootstrap Median
Overnight Sleep Opportunity	Blood CE	10.57	(4.89, 16.25)	<0.001	8.89	(3.62, 14.16)	0.001	100	1.00	-11.89	9.22
	CSF CE	169.37	(141.53, 197.22)	<0.001	170.45	(143.86, 197.04)	<0.001	100	0.96	0.70	171.06
	Age	0.50	(-0.03, 1.04)	0.071	–	–	–	29.8	1.40	63.40	0
	Male Sex	-6.10	(-9.89, -2.31)	0.002	-2.98	(-5.63, -0.34)	0.030	61.0	1.10	-29.97	-3.19
	APOE ε4	5.13	(1.89, 8.37)	0.003	4.29	(1.13, 7.46)	0.010	71.2	0.84	-1.90	4.08
	R _p	-55.47	(-77.74, -33.20)	<0.001	-52.55	(-74.76, -30.33)	<0.001	70.2	1.03	2.38	-49.70
	Delta Power	12.69	(-1.93, 27.32)	0.098	–	–	–	28.0	1.25	-15.65	0
	Theta Power	-8.69	(-18.01, 0.63)	0.075	–	–	–	18.4	1.77	-9.60	0
	Beta Power	-5.21	(-8.11, -2.32)	0.001	-6.29	(-8.54, -4.05)	<0.001	98.4	1.03	14.11	-5.96
Heart Rate	-81.28	(-112.92, -49.63)	<0.001	-54.48	(-79.51, -29.45)	<0.001	93.0	1.63	-26.68	-57.59	
Morning Sleep Opportunity	Blood CE	10.76	6.24, 15.29	<0.001	11.73	(7.89, 15.57)	<0.001	99.6	0.89	3.26	11.30
	CSF CE	154.87	125.96, 183.78	<0.001	145.25	(125.08, 165.42)	<0.001	100.0	1.02	-0.58	151.27
	Age	-1.38	-1.95, -0.81	<0.001	-1.26	(-1.74, -0.79)	<0.001	99.6	1.05	-1.70	-1.33
	Male Sex	-0.36	-2.75, 2.02	0.771	–	–	–	13.6	2.38	425.36	0
	APOE ε4	-2.89	-6.31, 0.53	0.109	-3.94	(-6.74, -1.15)	0.007	53.6	1.17	58.42	-3.17
	R _p	56.58	32.87, 80.29	<0.001	55.35	(33.01, 77.70)	<0.001	98.6	1.03	-5.03	53.67
	Delta Power	-39.36	-51.30, -27.42	<0.001	-35.94	(-44.10, -27.78)	<0.001	100.0	1.03	-2.48	-37.30
	Theta Power	9.01	-6.18, 24.20	0.259	–	–	–	40.0	1.26	74.24	0
	Beta Power	-2.68	-12.06, 6.70	0.585	–	–	–	24.0	1.85	190.46	0
Heart Rate	72.92	44.23, 101.62	<0.001	77.55	(49.74, 105.35)	<0.001	100.0	0.88	5.61	77.21	
Overnight Sleep Deprivation	Blood CE	7.42	-0.407, 15.25	0.076	13.09	(7.09, 19.10)	<0.001	56.6	1.59	72.95	8.57
	CSF CE	199.82	152.77, 246.87	<0.001	162.36	(129.54, 195.19)	<0.001	100.0	1.81	-0.67	193.14
	Age	0.06	-0.60, 0.72	0.871	–	–	–	4.0	2.01	-118.25	0
	Male Sex	-6.53	-10.37, -2.70	0.002	-4.81	(-8.05, -1.57)	0.005	90.8	0.96	1.08	-6.23
	APOE ε4	6.17	-0.71, 13.05	0.093	–	–	–	58.4	1.60	60.69	6.40
	R _p	12.37	-31.98, 56.71	0.600	–	–	–	8.8	1.31	199.07	0
	Delta Power	-31.79	-54.44, -9.13	0.009	-20.77	(-34.34, -7.20)	0.004	85.4	1.24	12.63	-30.78
	Theta Power	19.96	7.38, 32.53	0.003	7.89	(1.13, 14.64)	0.026	83.8	1.45	7.75	19.85
	Beta Power	-17.30	-32.72, -1.89	0.036	–	–	–	62.0	1.26	42.29	-17.71
Heart Rate	-25.01	-63.14, 13.11	0.218	–	–	–	44.2	1.75	97.16	0	
Morning Awake	Blood CE	10.58	5.67, 15.49	<0.001	9.83	(5.37, 14.29)	<0.001	98.0	0.86	-5.59	9.91
	CSF CE	232.82	210.603, 255.04	<0.001	232.52	(210.27, 254.77)	<0.001	100.0	1.07	0.84	233.00
	Age	-0.88	-1.72, -0.04	0.049	-0.72	(-1.43, -0.01)	0.057	63.8	1.14	28.44	-0.81
	Male Sex	0.96	-1.69, 3.61	0.495	–	–	–	20.2	2.18	223.65	0
	APOE ε4	11.02	8.30, 13.74	<0.001	10.54	(8.16, 12.92)	<0.001	100.0	1.63	-2.35	10.62
	R _p	25.30	-0.93, 51.53	0.071	29.38	(5.63, 53.13)	0.021	64.0	1.15	51.96	30.70
	Delta Power	-22.53	-32.67, -12.39	<0.001	-20.98	(-30.19, -11.77)	<0.001	98.6	1.38	-5.75	-21.33
	Theta Power	-15.37	-19.62, -11.134	<0.001	-15.27	(-19.51, -11.03)	<0.001	100.0	1.15	-2.22	-15.00
	Beta Power	-21.09	-24.15, -18.04	<0.001	-21.38	(-24.34, -18.43)	<0.001	100.0	1.13	0.73	-21.42
Heart Rate	230.91	194.43, 267.38	<0.001	235.70	(201.64, 269.76)	<0.001	100.0	1.19	0.74	234.67	

468 Parenchymal Resistance, R_p; Heart Rate, HR; Contrast Enhancement, CE; 95% Confidence Interval, CI; Backward Elimination, BE;
469 Root-Mean Square Deviation, RMSD; within ROI variability, σ^2 ; inter-ROI variability, T_{00 ROI}. **Bolded P values reflect significant**
470 **associations at P < 0.05.** Shaded cells demark the **null model** that includes blood CE, CSF CE and potential biological
471 confounders.

472 We used bootstrap analysis of the backward elimination algorithm for stability investigations on
473 the impact of variable selection on bias and variance of the regression coefficient and bootstrap
474 inclusion frequencies. We estimated the multivariate model using the backward elimination
475 algorithm on 500 bootstrap data replicates with replacement for each intervention period (**Table**
476 **1**). The bootstrap inclusion frequency represents the percent of the 500 backward elimination
477 models that retained each variable, while the bootstrap median is the median estimate for that
478 variable. The relative conditional bias quantified the omitted variable selection bias of each
479 variable from inclusion/non-inclusion of other variables from the full model. In the overnight
480 sleep opportunity, in addition to vascular and CSF contrast enhancement (each with an
481 inclusion frequency of 100%), R_P (70.2%), EEG beta power (98.4%), and heart rate (93.0%) had
482 high bootstrap inclusion frequencies and bootstrap median estimates comparable to the
483 selected model estimates. Device-measured R_P and ventricular contrast enhancement had the
484 lowest relative conditional bias, and therefore their predictions of parenchymal contrast uptake
485 were least affected by inclusion of the other variables. Findings in the morning sleep opportunity
486 also showed high inclusion frequencies of the variables retained in the backward elimination
487 algorithm on the full data set and bootstrap median estimates comparable to the selected model
488 estimates, with vascular contrast enhancement (99.6%), CSF contrast enhancement (100%), R_P
489 (98.6%), EEG delta power (100%), and heart rate (100%). These regressors also had low
490 relative conditional bias. These analyses suggest high model stability to perturbations of the
491 data set²⁹.

492
493 Lastly, we computed the percent of the residual variance of the null model that was explained by
494 including EEG power band, heart rate and R_P regressors for each intervention and computed
495 the LRT between the null model and the intervention models. For the overnight sleep and sleep
496 deprivation interventions, 24.5% and 12.7% of the residual null model variance was explained
497 by including these regressors, respectively. The null hypothesis that parenchymal contrast

498 enhancement is not influenced by these variables was rejected for the overnight sleep model
499 (likelihood ratio 52.6, p-value < 0.001) and the sleep deprivation model (likelihood ratio 14.1, p-
500 value = 0.015). Including the regressors in morning sleep and awake models explained 38.3%
501 and 74.8% of the residual null model variance, respectively. The null hypothesis that the
502 parenchymal contrast enhancement is not influenced by these variables during the morning
503 sleep (likelihood ratio 79.5, p-value < 0.001) and awake condition (likelihood ratio 149.6, p-value
504 < 0.001) were also both rejected.

505

506 ***Combined effects of parenchymal resistance and sleep stages on glymphatic function***

507 We developed a second comprehensive mixed model to define the relationship among R_p ,
508 sleep stages, heart rate and parenchymal contrast enhancement. As above, this comprehensive
509 model extended the null model that contained contrast enhancement in the blood and cerebral
510 ventricles as regressors, and age, APOE4 status, and gender as confounding biological
511 variables. We evaluated WASO time, and time in N1, N2, N3 and REM sleep stages.

512 **Supplemental Table 3** provides the model output for the overnight sleep opportunity (top) and
513 the morning sleep opportunity (bottom). In the overnight sleep opportunity model selected by
514 backward elimination, as before lower R_p was significantly associated with greater parenchymal
515 contrast enhancement (mean -67.17; 95% CI -87.78, -46.56; $P < 0.001$). In this model, more time
516 in REM sleep (mean 0.16; 95% CI 0.09, 0.23; $P < 0.001$), and less time in N1 (mean -0.32; 95%
517 CI -0.43, -0.21; $P < 0.001$), N2 (mean -0.10; 95% CI -0.15, -0.06; $P < 0.001$), N3 (mean -0.07; 95%
518 CI -0.12, 0.02; $P = 0.007$) sleep and WASO (mean -0.07; 95% CI -0.12, -0.02; $P = 0.006$) were
519 each associated with greater contrast enhancement. Bootstrap analysis showed that blood and
520 CSF contrast enhancement (each with an inclusion frequency of 100%), as well as R_p (100%),
521 REM sleep time (99.0%), N1 sleep time (98.8%) and N2 sleep time (98.0%) were the most
522 stable elements of the model relating sleep stages to parenchymal glymphatic function, while
523 the RMSD ratio for N2 sleep time, N3 sleep time and WASO showed substantial variance

524 deflation following backward elimination (**Supplemental Table 3**) that is associated with weak
525 or noise predictors.

526

527 In the morning sleep opportunity model selected by backward elimination, lower R_P was
528 significantly associated with greater parenchymal contrast clearance (mean 34.42; 95% CI 5.25,
529 63.59; $P = 0.025$), similar to the EEG band power model for this intervention. In this model, less
530 time in REM sleep (mean 0.41; 95% CI 0.20, 0.62; $P < 0.001$), and more time in N1 (mean -0.26;
531 95% CI -0.50, -0.02; $P = 0.04$) and N3 (mean -0.17; 95% CI -0.33, -0.021; $P = 0.031$) were
532 associated with less contrast enhancement, or greater contrast clearance. N3 sleep did not
533 survive bootstrap analysis while R_P , REM and N1 sleep had inclusion frequencies of 65.4%,
534 88.2% and 61.6%, respectively (**Supplemental Table 3**).

535

536 ***Effects of sleep stages on brain parenchymal resistance***

537 To understand if sleep stages had a differential effect on the overnight change in R_P , we
538 computed the mean of the first-order differences ΔR_P for each sleep stage for the Benchmarking
539 and Replication studies separately and combined (**Figure 5**). The mean ΔR_P was negative and
540 largest for N2, N3 and REM sleep stages reaching significance when the values for both studies
541 were pooled together. This suggests that R_P in **Figure 4a-c** decreases during N2, N3 and
542 REM sleep.

543

544 ***Effects of large changes in EEG spectral power on brain parenchymal resistance***

545 To define the relationships between sleep EEG powerbands, heart rate and R_P , we modeled the
546 relationship between the first-order difference ΔR_P and the difference in spectral band power
547 (Δ delta, Δ theta, Δ alpha, Δ beta) and changes in heart rate Δ HR, during NREM, REM and Wake
548 (**Table 2**). We utilized threshold regression to model the relationships between ΔR_P and large

549 changes in (Δ) band power or heart rate. A custom estimation procedure described in
 550 **Supplemental Information** was used to jointly estimate the threshold regression for the full
 551 positive and negative ranges of Δ band power and Δ HR. The full output of the threshold
 552 regression models is provided for the combined study data in **Table 2**. In both REM and NREM
 553 sleep, a large increase in Δ delta was significantly associated with a decrease in ΔR_P (**Figure**
 554 **6a**). In contrast during REM and NREM sleep, a large increase in Δ beta was significantly

555 **Table 2. The change in parenchymal resistance resulting from large changes in EEG**
 556 **band power and heart rate occurring during REM sleep, NREM sleep, wake, and at NREM-**
 557 **REM and sleep-wake transitions.**
 558

Study Condition	Period	Predictors	Fixed Effects				Threshold Model Parameters		
			Estimate	CI	p	DF	Positive Threshold	Negative Threshold	Slope Ratio
Overnight Sleep Op	NREM	Δ delta	-0.28	(-0.50, -0.058)	0.014	1380	1.5	-1.5	0.7
		Δ theta	-0.08	(-0.23, 0.063)	0.265	1380	1.5	-0.98	0.5
		Δ alpha	-0.14	(-0.30, 0.022)	0.091	1380	1.5	-1.25	0.65
		Δ beta	0.04	(0.0022, 0.080)	0.039	1380	0.18	-1.5	2
		Δ HR	0.10	(-0.0033, 0.19)	0.059	1115	0.43	-0.43	0.5
	REM	Δ delta	-0.57	(-0.77, -0.37)	<0.001	319	1.5	-1.5	2
		Δ theta	-0.41	(-0.70, -0.13)	0.005	319	0	-1.5	0.5
		Δ alpha	-0.09	(-0.21, 0.041)	0.189	319	1.45	0	2
		Δ beta	0.45	(0.14, 0.77)	0.006	319	1.5	-1.3	0.5
		Δ HR	0.31	(-0.057, 0.68)	0.101	271	1.5	-1.15	0.5
	NREM to REM	Δ delta	-0.29	(-0.82, 0.24)	0.293	67	1.5	-1.05	2
		Δ beta	0.77	(0.04, 1.49)	0.046	67	0.6	-1.5	0.5
	REM to NREM	Δ delta	-1.50	(-2.35, -0.66)	0.001	58	1	-1.5	0.5
		Δ beta	-0.05	(-0.24, 0.14)	0.615	58	0.1	-1.5	1.85
Sleep to Wake	Δ delta	0.03	(-0.34, 0.4)	0.885	66	1.5	-0.3	1.95	
	Δ beta	0.73	(0.13, 1.32)	0.021	66	0.35	-1.23	0.5	
Wake to Sleep	Δ delta	-0.20	(-0.64, 0.25)	0.392	113	0.05	-1.35	0.6	
	Δ beta	0.37	(-0.01, 0.76)	0.065	113	1.5	-1.05	2	
Overnight Sleep Deprivation	WAKE	Δ delta	-0.06	(-0.15, 0.034)	0.216	1137	1.5	0	0.5
		Δ theta	-0.07	(-0.17, 0.035)	0.198	1137	1.4	-1.45	2
		Δ alpha	0.06	(-0.030, 0.14)	0.206	1137	1.15	0	0.73
		Δ beta	0.12	(0.0075, 0.23)	0.037	1137	1.5	-1.43	1.93
		Δ HR	-0.10	(-0.20, -0.011)	0.029	1002	0.25	-0.25	0.5

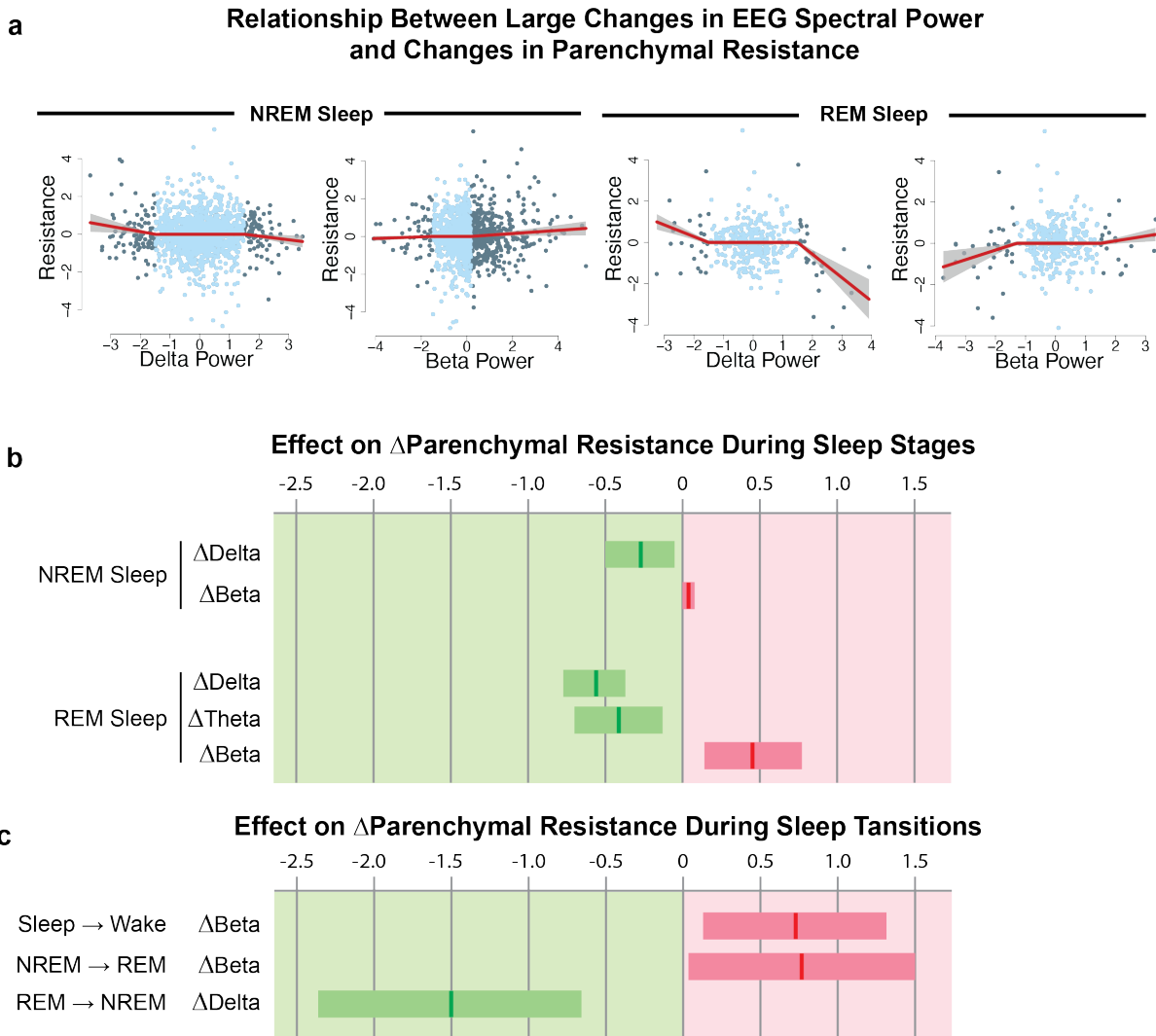
559 Rapid eye movement, REM; non-REM, NREM; Confidence Interval, CI; Degrees of Freedom,
 560 DF; EEG band power predictor units in percent of total band power; HR predictor units beats-
 561 per-minute. **Bolded P values reflect significant associations at P < 0.05.** Predictor and
 562 parenchymal resistance values in regression models were scaled to zero mean and unit
 563 standard deviation with coefficient estimates representing effect size in standard deviations.
 564 Positive and negative thresholds are in units of predictor standard deviation. Models included
 565 confounding biological variables age, gender, and APOE ϵ 4 status.
 566

567 associated with an increase in ΔR_P . The threshold models for the significant estimated effects of
568 Δ band power on ΔR_P are plotted in **Figure 6b**. The full output of the threshold regression model
569 is provided for each site individually in **Supplemental Table 4**. Because the variables were
570 standardized before model estimation, the regression estimates in **Table 2** and **Supplemental**
571 **Table 4** can be interpreted as standardized effect sizes. Note that because of the slope ratio r ,
572 changes that exceed the positive change point t_p have effect sizes given by the regression
573 estimate multiplied by the slope ratio. The positive and negative thresholds are in units of
574 standard deviation.

575
576 The asymmetric effect of EEG band power changes on R_P shown in Figure 5 accounts for the
577 progressive decline in R_P that occurs through the course of the overnight sleep period, shown in
578 **Figure 4a-c**. In the overnight wake state, Δ beta had a significant but small effect on ΔR_P . Δ HR
579 in NREM and wake had a small effect on ΔR_P and a larger but non-significant effect in REM.

580 The threshold model findings in **Table 2** and plots in **Figure 6a** demonstrate that large changes
581 in spectral band power are needed to alter R_P . Because such large changes in EEG
582 powerbands and HR occur at sleep stage transitions, we explored the associations between
583 Δ delta and Δ beta and ΔR_P at NREM-REM and REM-NREM transitions, and at Sleep-Wake and
584 Wake-Sleep transitions. **Table 2** provides the full model output on sleep stage transitions for
585 data pooled from both study sites, while the significant estimated effects of Δ delta and Δ beta on
586 ΔR_P are plotted in **Figure 6c**. The full output of the threshold regression model on sleep stage
587 transitions is provided for each site individually in **Supplemental Table 5**. During the NREM-
588 REM, Wake-Sleep, and Sleep-Wake transitions, changes in EEG beta power and not EEG delta
589 power underlie the observed changes in ΔR_P . In contrast, during the REM-NREM transition,
590 changes in EEG delta power and not beta power were associated with changes in ΔR_P . In total,

591



592
 593 **Figure 6. Brain parenchymal resistance is increased by large changes in EEG beta power**
 594 **and reduced by large changes in EEG delta power. a,** Threshold linear mixed regression
 595 model of R_P against EEG delta and beta power for REM and NREM sleep shown with standard
 596 error after differencing both R_P and powerband values to make data stationary, standardizing
 597 the ΔR_P and Δ powerband values to zero mean and unit standard deviation, and adjusting for
 598 site, age, gender, APOe4 and site-age interaction confounders. Units of ΔR_P and Δ powerband
 599 are in standard deviations. Data in light blue are inside the change points and data in dark blue
 600 are outside the change points. When delta and beta power changes between successive
 601 measurements exceed 1.0 to 1.5 stand deviations, we observe significant changes in ΔR_P . **b,**
 602 95% CI of regression coefficients show that large changes in REM delta, theta and beta, and
 603 NREM delta and beta are significant predictors of ΔR_P . For a 1 standard deviation increase in Δ
 604 powerband, an increase (decrease) in ΔR_P is illustrated in red (green) with units along the top in
 605 standard deviation of ΔR_P . **c,** Large changes in beta and delta powerbands at sleep-wake and
 606 NREM-REM transitions show significant effect on ΔR_P consistent with the step change in beta
 607 and delta power at these transitions. For a 1 standard deviation increase in Δ powerband across
 608 a sleep-wake or NREM-REM transition, an increase (decrease) in ΔR_P is illustrated in red
 609 (green) with units along the top in standard deviation of ΔR_P .

610
611

612 these data show that glymphatic function is enhanced by declining R_P , and that R_P in turn
613 declines with reduced EEG beta power and heart rate, and with increasing EEG delta power.

614

615 **DISCUSSION**

616 We have described a non-invasive multimodal skin-interfaced wireless device for continuous
617 measurement of brain parenchymal resistance R_P using repeated EIS time-multiplexed with
618 EEG and cardiovascular measurements. Through two separate clinical validation studies, we
619 observe that brain R_P measured by the device faithfully captures sleep-active changes in
620 glymphatic flow resistance based on three complementary criteria established from studies in
621 the murine and human brain. Brain R_P declines overnight, paralleling sleep-associated changes
622 in extracellular volume that regulate glymphatic function². Brain R_P is reduced with increasing
623 sleep EEG delta power, and is increased with increasing sleep EEG beta power and heart
624 rate¹¹. Lastly, brain R_P is a robust predictor of glymphatic function, measured by CE-MRI^{12-15,30}.
625 These findings demonstrate that this investigational device provides the first remote, non-
626 invasive, and time-resolved measure of glymphatic flow resistance suitable for defining this
627 sleep-active biology in naturalistic settings.

628

629 Several technological advances have enabled this work. We have developed a technique for
630 low-noise EIS measurements using multiple excitation and sense configurations to determine
631 the brain parenchymal impedances accurately. A signal processing approach enabled the
632 segregation of signal and noise, using the Kramers-Kronig relations^{31,32} between the real and
633 imaginary parts of the impedance to establish if the measured response is related to the
634 excitation signal or has been distorted by noise or other artifact. Unlike applications of EIS to
635 neurological conditions such as seizures, tumors or cerebral edema³³⁻³⁶, the rapid evolution of

636 glymphatic function during sleep and its nightly variability make it suitable for monitoring with
637 longitudinal repeated assessments. Data collected under a variety of scenarios in benchtop
638 testing, agar phantom testing with biological interfaces and in-human testing indicate that this
639 system yields consistent, repeatable results and shows longitudinal stability of the measured
640 impedances.

641
642 A key first step in validating any potential measure of glymphatic function is assessing its
643 performance against established, principally contrast-based, measures of glymphatic exchange.
644 Initial studies characterizing glymphatic function in rodents utilized dynamic in vivo
645 fluorescence-based imaging^{1,2,37}. More recent studies in rodents, and recently in human
646 participants, have utilized CE-MRI following either intrathecal or intravenous GBCA
647 injection^{12,14,15,30,38}. We evaluated whether device-based R_P measures reflect glymphatic
648 function by measuring overnight and morning R_P , EEG, and the movement of GBCA into brain
649 tissue over a four-hour timeframe. In the analysis, both overnight and morning R_P emerged as
650 robust explanatory variables of net contrast movement, in a regression model that included CSF
651 and blood contrast levels, EEG neurophysiological parameters, age, gender and APOE e4
652 confounders. It is important to note that device-based R_P measures are acquired with 2-minute
653 temporal resolution whereas CE-MRI captures overall glymphatic function over a 4-hour
654 window. This fine temporal resolution enabled translational validation of the physiological drivers
655 of glymphatic function in the human brain for the first time. It further revealed that while key
656 events during sleep were necessary to lower parenchymal resistance R_P , low R_P was sufficient
657 to enhance glymphatic function independent of sleep in the morning period. In addition, it
658 showed that sleep-related changes in R_P do not shift with sleep-wake in a stepwise fashion, but
659 rather accumulate through the course of time spent sleeping or awake. These observations are
660 not inconsistent with prior studies in rodents that used real-time iontophoresis to measure sleep-
661 associated increases in brain extracellular volume fraction², as these observational studies did

662 not directly test the causal effect of these changes in extracellular volume on glymphatic
663 function, and did not monitor changes in extracellular volume fraction in a time-resolved manner
664 over extended period. Future studies of the determinants of glymphatic function in human sleep
665 will likely further refine existing conceptual models of sleep-wake regulation of glymphatic
666 function.

667

668 The physiological mechanisms regulating glymphatic function have been defined almost
669 exclusively through experimental rodent studies^{1,2,10,11,30,37,39,40}, due in large part to invasiveness
670 and poor temporal resolution of contrast-based measures of glymphatic function^{12-15,30}. It is
671 noteworthy that these rodent studies are not all in agreement. While multiple studies have
672 reported more rapid glymphatic exchange under conditions of sleep, or under certain anesthetic
673 regimes^{2,11,41-45}, two studies^{46,47} have reported apparently slower clearance during sleep or
674 under anesthesia. In the present human clinical studies, we demonstrate within-participant
675 longitudinal declines in brain R_p during overnight sleep, but not in awake participants. During
676 morning recovery sleep, we demonstrate within-participant longitudinal declines in brain R_p and
677 during morning wake we observe increases in brain R_p . This pattern is consistent with sleep-
678 wake changes in extracellular volume fraction measured in mice and reported by Xie et al.².
679 Using overnight PSG followed by CE-MRI in human participants, we confirmed that glymphatic
680 function in the human brain is associated with lower EEG beta power and heart rate, and in a
681 simplified model with increasing EEG delta power. These findings sustain the physiological
682 findings in mice from Hablitz et al.¹¹. More broadly, these human CE-MRI-based imaging studies
683 demonstrate that glymphatic solute exchange is more rapid under conditions of natural sleep, at
684 least in human participants, and that these sleep-wake differences are regulated by sleep-
685 related changes in R_p , heart rate, and EEG spectral band power.

686

687 Linking changes in R_P with sleep EEG features, we further demonstrate that the investigational
688 device-based measure of R_P exhibits the same dependence upon EEG delta power, EEG beta
689 power, and heart rate during sleep. Conducting parallel time-resolved sleep EEG and R_P
690 measurements, we observed that rapid changes in R_P occurred at sleep stage transitions
691 between REM and NREM, and between sleep and wake. Transitions between REM and NREM
692 exhibit large changes in EEG delta and beta powerbands, and in HR, consistent with our
693 findings. Large changes in an EEG power within a frequency band can occur because of
694 sudden bursts of oscillatory activity within the band's frequency range. In rodents, recent
695 experiments support a role for such synchronized oscillatory activity as a mechanism driving
696 glymphatic flow by creating propagating ionic waves within the brain interstitium⁴¹. To our
697 knowledge, this is the first time that these physiological drivers of glymphatic function have been
698 confirmed in human participants, within an experimental setting permitting validation against
699 current benchmark CE-MRI-based measures of glymphatic function well established preclinical
700 features.

701
702 There are clear limitations both of the investigational device, and of the present study design.
703 Existing MRI-based measures of glymphatic function remain poorly time-resolved but provide
704 excellent cranium-wide anatomical resolution. In contrast, the present investigational device
705 captures a measure of global brain glymphatic flow resistance with high temporal resolution.
706 While finer anatomical resolution may have value in future iterations of the investigational
707 device, it is important to note that the present design was sufficient to capture sleep-wake
708 changes in glymphatic function, and to define novel neurophysiological drivers of these
709 processes in the human brain. Study methodological limitations include protocol differences
710 between the Benchmarking Study and Replication Study. The Benchmarking Study included
711 CE-MRI as part of the neuroimaging package and gold-standard PSG concurrent with the
712 device usage whereas the Replication Study did not include CE-MRI and used the device's

713 single-derivative EEG. Furthermore, the Benchmarking Study enrolled participants 55-65 years
714 old living in Florida whereas the Replication Study enrolled participants 50-65 years old living on
715 the West Coast. Despite these differences, after adjusting for age, study site and age-site
716 interaction effects, we confirmed that the device's single-derivative EEG showed good
717 agreement with the PSG of the Benchmarking Study. Additionally, the pooled analysis and
718 study-specific analyses of R_P , EEG and HR were all in good agreement between studies. The
719 Benchmarking Study was powered to detect a low to moderate correlation between R_P and CE-
720 MRI measures of glymphatic function, which was confirmed. Quality control of the
721 investigational device filtered out measurements that did not satisfy the Kramers-Kronig
722 relations^{31,32}. Failed measurements were more common in the Benchmarking Study, particularly
723 during the awake conditions. This is attributable to excessive motion, likely due to the technical
724 challenges associated with conducting concurrent PSG and device-based sleep EEG measures
725 in participants being kept awake by study staff. The low rate of quality-control failures in the
726 Replication Study that did not involve PSG instrumentation supports this conclusion.

727
728 The characterization of the glymphatic system in rodents beginning in 2012 has spurred a great
729 deal of interest into its potential mechanistic role linking sleep to cognitive performance, and
730 sleep disruption to a wide range of neurological and psychiatric conditions including Alzheimer's
731 disease, Parkinson's disease, chronic traumatic encephalopathy, stroke, traumatic brain injury,
732 headache and others⁴²⁻⁴⁵. Preclinical studies have demonstrated that glymphatic function is
733 impaired in the setting of aging⁴⁸, sleep disruption², cerebrovascular injury^{49,50}, and traumatic
734 brain injury³, all risk factors for neurodegenerative conditions including Alzheimer's disease.
735 Experimental impairment of glymphatic function is sufficient to promote the development of the
736 amyloid beta⁵¹⁻⁵³ and tau pathology³⁻⁵ characteristic of Alzheimer's disease. In clinical
737 populations, genetic and histological associations support a link between glymphatic dysfunction
738 and the development of clinical disease^{52,54-56}. Yet the technical challenges of real-time dynamic

739 measurements of glymphatic function in human clinical populations have proven a challenging
740 barrier to defining the causal role of glymphatic function and dysfunction in the development of
741 neurological and psychiatric conditions in these populations. Whether glymphatic dysfunction
742 contributes to development of conditions such as Alzheimer's disease remains to be directly
743 tested. The present investigational device may permit the continuous and time-resolved
744 assessment of glymphatic function in naturalistic settings necessary to define whether
745 glymphatic impairment contributes to risk and progression of Alzheimer's disease and its
746 underlying pathological processes. The ability to assess glymphatic function over short
747 timescales may enable target-engagement studies to identify and test pharmacological, device-
748 based and lifestyle/behavioral interventions for modulating glymphatic function in humans.
749 Assessment of these processes may also permit the identification of clinical populations with
750 impaired glymphatic function, at risk for the development of Alzheimer's disease, and who would
751 thus be ideal candidates for therapeutic approaches targeting glymphatic clearance. Similar
752 avenues now remain open outside the realm of neurodegenerative conditions as glymphatic
753 dysfunction is implicated in an ever-increasing list of sleep-related neurological and psychiatric
754 conditions.

755 **METHODS**

756 ***Investigational Device***

757 *System Architecture*

758 The Applied Cognition device is a wearable multi-sensor acquisition system that uses an
759 STM32WB5MMG microcontroller (ST Microelectronics, NV). It consists of a primary module
760 housing the main electronics board and a 430 mAh Li-ion battery, two earpieces each housing
761 one electrode, one accelerometer and one photoplethysmogram sensor, and two separate
762 mastoid electrodes. A device schematic and visualization of signal outputs is provided in
763 **Figure 2a-f**. Sensor data is stored in on-board FLASH memory and is downloaded via a USB
764 port for offline analysis. The relevant sub-systems are further described below.

765

766 *Electrical Impedance Spectroscopy*

767 Electrical impedance spectroscopy (EIS) was used to measure electrical impedance using the
768 AFE4500 analog front-end (AFE) from Texas Instruments. Four electrodes – two in-ear and two
769 mastoid – were used to deliver the excitation current across the head and sense the resulting
770 voltage. The two mastoid current injection sources were initially co-located inside the ear next to
771 the Ag/AgCl sensors but because of salt-bridging were externalized to the mastoids. In a
772 departure from traditional four-electrode measurements, where excitation and sense electrodes
773 are fixed, the AFE4500 was programmed to implement a technique developed by Texas
774 Instruments where multiple excitation and sense configurations are used to determine the
775 contact impedance and body impedance accurately.

776

777 Measurements were successively performed at eighteen frequencies ranging from 1 kHz to
778 256 kHz following a logarithmic series, all with excitation current below 50 μ A root-mean-square
779 (rms). Frequencies were in alternating order from high-low to minimize any impact on
780 impedance drift during each scan. Sensed voltages were quadrature-demodulated, filtered and

781 digitized internally by the AFE4500 to provide in-phase and out-of-phase components.

782 Measurement time for each frequency was adjusted to give consistent signal-to-noise ratio
783 across the frequency range, resulting in a scan time of 106 seconds.

784

785 *Electroencephalogram*

786 Electroencephalogram (EEG) was measured with an ADS1299-4 AFE from Texas Instruments,
787 between the two in-ear electrodes (differential measurement). A third electrode (left mastoid)
788 was used to drive the common mode. While these electrodes were shared with the EIS, the two
789 measurements were time-multiplexed and a pair of analog multiplexers (TMUX1136, Texas
790 Instruments, Inc.) effectively decoupled EEG and EIS sub-circuits and respective
791 measurements. For EEG, both in-ear electrodes were also buffered (OPA376, Texas
792 Instruments, Inc.) in the earpiece. These buffers were bypassed (analog multiplexer
793 TMUX1136, Texas Instruments, Inc.) for EIS or electrode impedance measurement.

794

795 The ADS1299-4 was programmed to have a sampling rate of 250 samples-per-second (24-bit
796 samples) and an input range of ± 180 mV. The common mode drive was actively derived from
797 the in-ear electrodes. Both mastoid electrodes were also connected to an input channel so that
798 the low-frequency (31.25 Hz) impedance of each electrode could be measured using the
799 internal current source of the ADS1299-4. Such impedance measurements were performed
800 before starting a recording session, and then automatically between EEG periods and EIS. EEG
801 measurement periods were 170 seconds long, and the sequence EEG-EIS-Electrode
802 impedance repeated until the end of the recording session. A sample EEG spectrogram and
803 hypnogram, derived from the device EEG is shown in **Figure 2b**.

804

805 *Impedance Plethysmogram*

806 In addition to impedance spectroscopy, real-time bioimpedance was acquired simultaneously
807 with the EEG, using the MAX30001 AFE (Analog Devices, Inc.). The four-electrode
808 configuration shared electrodes with the EEG, with the two mastoid electrodes used for current
809 injection and the two in-ear electrodes for voltage sensing. A 96 μA current at 82 kHz was used
810 for excitation. Such high frequency excitation is effectively filtered by the ADS1299-4 and does
811 not corrupt the EEG signal. The MAX30001 built-in synchronous demodulator filtered and ADC
812 recovered the in-phase component of the sensed voltage and digitized it at 64 samples-per-
813 second (20-bit resolution). The resulting impedance measurements had a noise floor of 3 m Ω
814 rms (100 Ω load), enabling the detection of blood pulsations. A sample trace from a study
815 participant, derived from the device IPG is shown in **Figure 2d**. Note that the impedance shifts
816 measured in either the respiratory or cardiac frequency bands range between 50 to 150 m Ω . In
817 contrast, impedance shifts detected by EIS were at least an order of magnitude greater.

818

819 *Photoplethysmogram and Acceleration*

820 In-ear reflective photoplethysmogram (PPG) was measured with two miniature, fully-integrated
821 optical sensors MAXM86161 (Analog Devices, Inc.) located in each earpiece, facing the anterior
822 wall of the ear canal. One side was programmed to use green light (530 nm), while the other
823 used alternatively red (660 nm) and infrared (880 nm) lights. To achieve a tight synchronization
824 with EEG samples, the sensors ran at 1024 Hz for each color, and the most recent samples
825 available at the time of the EEG read were averaged, resulting in a 250 Hz output rate and a
826 phase variation <1 ms. A sample trace of the left (red) and right PPG (green) from a study
827 participant is provided in **Figure 2f**.

828

829 In-ear acceleration (X,Y,Z) was measured using two miniature MEMS Inertial Measurement Unit
830 (IMU) LSM6DSOX (ST Microelectronics, NV) located in each earpiece. Similar to the PPG, the

831 sensors were run at 833 Hz (each axis) and averaged to ensure tight time synchronization
832 between sensors. A noise floor of 1 mg rms enabled the resolution of cardiac/blood pulsations,
833 in addition to posture and activity. From these accelerometer data, a ballistocardiogram is
834 derived, as shown for a study participant in **Figure 2e**.

835

836 *Electrodes*

837 In-ear electrodes were laser-cut from silver sheets 100 microns thick and 99.9% purity. The
838 electrodes were 4.5 mm diameter plates with a 1 mm-wide stem. The electrodes were abraded
839 and sonicated in distilled water, dip-coated with Ag/AgCl ink provided by Creative Materials Inc
840 (SKU EXP 2653-138-1) and cured at 100°C for 60 min. Following curing, they were sintered at
841 427°C for 60 minutes under low-flow argon gas.

842

843 Once fabricated, all electrodes were characterized according to the ANSI/AAMI EC12 standard
844 for AC impedance⁵⁷, DC offset voltage, combined offset instability and internal noise, and bias
845 current tolerance (**Supplemental Table 7**). Pairs of electrodes were also connected to the
846 earpiece circuits with clip-on wires and tested on an agar phantom as described in the *Device*
847 *Testing* section.

848

849 *Electrical Impedance Spectroscopy Validation*

850 Measurement accuracy was first evaluated using a test fixture simulating the load and the four
851 electrodes (**Supplemental Figure 2**). The load was either purely resistive (R , 20-100 Ω), or
852 slightly reactive ($2R1C$, 20-100 Ω in parallel with 470 Ω and 22 nF in series) to mimic the brain
853 parenchyma. The electrodes were implemented as either (i) low impedance (270 Ω resistor in
854 series with a 1 k Ω resistor and 180 nF capacitor in parallel), or (ii) high impedance (620 Ω
855 resistor in series with a 3.3 k Ω resistor and 82 nF capacitor in parallel), in order to simulate the

856 frequency-dependence of typical Ag/AgCl electrodes, but also to ensure a minimal impedance
857 at high frequencies. Two 10 Ω resistors were added between the electrodes connected to the
858 same side of the load to simulate the tissue impedance between these electrodes as well.

859 **Supplemental Table 8** describes the benchtop tests performed and **Supplemental Table 9**
860 and **Supplemental Table 10** contain the results.

861

862 *Device Testing*

863 In addition to the EIS test fixture, stability and reproducibility of EIS measurements over twelve
864 hours were evaluated with an agar phantom. A slab (5-10 mm thick) of conductive agar was first
865 cast using a solution of 2.5% weight agar (Living Jin USA, Inc.), 0.64% weight NaCl (RND
866 Center, Inc.) and distilled water. Electrodes (mastoids and earpieces for the final testing) were
867 then coated with conductive gel (Electro-Gel, Electro-Cap International) to reduce the contact
868 resistance, and placed on the agar slab in a pattern geometrically similar to the electrode
869 location on the head. A 12-hour recording was performed, resulting in a total of 450 minutes of
870 EEG recording, 159 EIS cycles and 160 electrode impedance checks. The results of a 12 hr
871 agar phantom EEG test is shown in **Supplemental Figure 3**.

872

873 *Signal Processing – Parenchymal Resistance*

874 A python neuroprocessing pipeline developed by Applied Cognition performed the data analysis
875 of the signals captured by the investigational device. The neuroprocessing pipeline runs in the
876 Amazon Web Services cloud on a distributed architecture allowing for fast parallel execution of
877 participant device readings.

878

879 An EIS scan by the investigational device measured impedances $Z(\omega)$ at 18 frequencies f ($\omega =$
880 $2\pi f$) ranging from 1,000 Hz to 256,000 Hz and took 106 seconds. The frequencies were
881 measured in the following permuted order for each scan (all in Hz): 2276, 102400, 1600, 64000,

882 4551, 51200, 12800, 85333, 3200, 25600, 1000, 32000, 6400, 8533, 128000, 204800, 256000.

883 During the EIS scan, all other device sensors were powered off except the left-in-ear IMU that
884 sampled at 1Hz to detect head motion and position. The EIS scans were duty-cycled throughout
885 the recording period with 165 second neurophysiology scans that captured data from the other
886 sensors: EEG, PPGs and IMUs. Four electrode impedance checks at 30Hz and lasting 7
887 seconds were performed during the neurophysiology scan and immediately preceding the EIS
888 scan.

889

890 The Cole-Cole model⁵⁸⁻⁶⁰ is commonly used to analyze EIS data. The analysis is based on the
891 four parameters contained in the Cole equation R_0 , R_∞ , α and τ .

892
$$Z(\omega) = R_\infty + \frac{R_0 - R_\infty}{1 + (j\omega\tau)^\alpha}$$

893 As the excitation frequency ω ($\omega = 2\pi f$) increases to large values, the capacitive cell
894 membranes are invisible to the excitation frequency and the impedance $Z(\omega)$ approaches R_∞ .
895 The four excitation and response electrodes are positioned trans-cranially and at large ω
896 measure total intracranial brain volume. As the excitation frequency ω decreases approaching
897 DC values, the capacitive cell membranes prevent any transmembrane conduction and the
898 impedance $Z(\omega)$ approaches R_0 the measure of electrical resistance through extracellular fluid.

899

900 The value of τ in the Cole-Cole model is the inverse of tissue characteristic frequency $2\pi f_c$. The
901 Cole-Cole α describes the divergence of a measured dielectric dispersion from the ideal
902 dispersion exhibited by a Debye type of dielectric relaxation, and is widely assumed to be
903 related to a distribution of the relaxation times in the system involved. The value of α ranges
904 from 0.5 to 1 with a value of 1 reducing the Cole-Cole model to the Debye model.

905

906 For each EIS scan, the four parameters were estimated using a non-linear least-squares fit
907 (Python SciPy's `least_squares`) with the Trust Region Reflective algorithm that is a robust
908 method suitable for large sparse problems with bounds. The α parameter was found to be close
909 to one in the estimations and thereafter set to one, reducing the Cole-Cole model to the Debye
910 model. The remaining three parameters were estimated with bounds of 0 to 90Ω for R_0 , 0 to 70Ω
911 for R_∞ and bounds for $\tau = \frac{1}{2\pi f_c}$ determined by requiring the characteristic frequency f_c to lie
912 between 16kHz and 160kHz. The parameter bounds were confirmed to encompass
913 neurophysiological values in all participants by plotting all EIS scan resistance (real values of
914 impedances $Z(\omega)$) and reactance (imaginary values of impedance $Z(\omega)$). Furthermore, no
915 parameter solutions lay on a boundary for each scan across the range of dynamic impedance
916 spectroscopy measurements for all participants.

917

918 Prior to fitting the Debye model to the EIS scan data, to compensate for stray capacitance, time
919 delay effects from signal transmission and electrical components, the impedances Z from each
920 scan were rotated by multiplying by the factor $e^{-j\omega T}$ with the value T chosen so that the
921 reactance at the highest frequency of the scan was zero⁵⁹. This rotation was independently
922 validated using EIS scans recorded on the benchtop tests using known impedance loads
923 (**Supplemental Table 10**). The root-mean-squared-error (RMSE) of the Debye model fits to the
924 benchtop tests (**Supplemental Table 8**) are reported in **Supplemental Table 11**.

925

926 Each EIS scan measures R_P at a point in time and to evaluate glymphatic function the Debye
927 model fits need to detect small changes in R_P . With the device time-multiplexing settings, the
928 device completes approximately 84 scans over a 7-hour night of sleep. The statistical models
929 require significance testing of the mean change in R_P between sleep and wake, and testing
930 significance of predictors of R_P in linear mixed models. These tests depend on the SD of the

931 Debye model dispersion and the number of EIS scans (**Supplemental Table 12**). Details of
932 these analyses are found in **Supplemental 4**.

933

934 During EIS, tissue behaves as a linear, time-invariant and causal system allowing the use of

935 Kramers-Kronig relations to identify electrical impedance measures that are corrupted by

936 artifacts from motion, electrode impedances and other sources^{31,32}. The Kramers-Kronig

937 transform allows the real part of the electrical impedance measure to be derived from the

938 imaginary part and vice versa³¹. These relations are used as validity tests for measured

939 spectrums. When the real and imaginary impedance measures do not satisfy the Kramers-

940 Kronig relation the measure is discarded. The Python PyEIS1.0.10 repository was used for

941 Kramers-Kronig impedance validation. The validation uses the method of Schönleber³² to avoid

942 ambiguities in the linear Kramers-Kronig validity tests due to under- and over-fitting.

943

944 In addition to the Kramers-Kronig validity tests, EIS measures were discarded if for any of the

945 four electrode impedances, the difference across successive time measures exceeded 1k Ω or if

946 the EIS scan was collected during a wake interval on a participant randomized to sleep. The first

947 condition ensured that the electrode impedances were maintained within a narrow range during

948 the EIS scans and the second condition ensured that the EIS scans were representative of

949 sleep physiology for participants randomized to sleep.

950

951 *Signal Processing – Electroencephalography*

952 The raw EEG tracings from the device and the commercial PSG (Philips Respironics Alice 6

953 LDx Diagnostic Sleep System) were time-synchronized by time-aligning a 100-ms square pulse

954 generated by the device every 10 seconds and stored both in the device flash memory and in

955 the PSG recording through as an unused auxiliary analog input channel. Each raw tracing was

956 notch filtered at 60 Hz using a second-order infinite impulse response (IIR) notch digital filter

957 (Python SciPy *iirnotch*). The digital filter was applied to the signal forward and backward with a
958 combined filter phase of zero (Python SciPy *filtfilt*). The signal was then bandpass filtered
959 between 0.3 Hz and 50 Hz using a finite impulse response (FIR) filter with a Hann window
960 (Python SciPy *firwin*). The length of the low-pass filter was 501 and the length of the high-pass
961 filter was 2,401.

962

963 During the observation periods, participants were not allowed to touch devices that were
964 plugged to power outlets. Other non-physiologic sources included excessive head motion that
965 led to signal artifacts from the electrode-skin interface. Physiologic sources of signal artifact
966 included electrooculogram, electrocardiogram and electromyogram. The signals were
967 partitioned into time-aligned 30-second epochs. Epochs containing one or more peak-to-peak
968 signal amplitude exceeding 350 μV or maximum power in the Welch power spectrum exceeding
969 1,000 $\mu\text{V}^2/\text{Hz}$ were removed. In addition, the device left in-ear and right-in ear IMU signals were
970 used to filter excessive motion by filtering epochs with peak-to-peak values on an x-, y-, or z-
971 axis on either ear that exceeded 100 milli-g during sleep and 200 milli-g during wake.

972

973 The power spectral density of each 30-second epoch was computed using Welch's method⁶¹
974 (Python Scipy *welch*) using 10-second segments and 50% overlap across successive
975 segments. Relative power bands were computed for delta power (1-4 Hz), theta power (4-8 Hz),
976 alpha power (8-12 Hz), sigma power (12-15 Hz), beta power (15-30 Hz) and low gamma power
977 (30-50 Hz), each normalized to the total power in the power spectral density. Simpson
978 integration of the power spectral density was used for computing the total power and respective
979 band powers.

980

981 Hypnogram staging of each 30-second epoch used automated scoring (Python yasa 0.6.3
982 *SleepStaging*) trained and validated on 3,000 nights of data from the National Sleep Research

983 Resource⁶². The automated scoring uses a single EEG derivative and a single EOG channel.
984 For device hypnogram staging the single in-ear transcranial derivative was used and for the
985 commercial PSG, hypnogram staging using C3-A2 and C4-A1 derivatives were recorded
986 separately. The PSG left EOG channel was used for commercial PSG hypnogram staging. An
987 additional T3-T4 transcranial PSG derivative was used for hypnogram staging as another
988 comparison to the device's transcranial in-ear derivative. The internal agreement of commercial
989 PSG and agreement between investigational device-based EEG and PSG are presented in
990 **Supplemental Table 6.**

991

992 *Signal Processing – Heart Rate*

993 The photoplethysmography (PPG) left and right raw signals were bandpass filtered between 0.5
994 Hz and 10 Hz using a finite impulse response (FIR) filter with a Hann window (Python SciPy
995 *firwin*). Empirical mode decomposition was used to identify peaks in the raw signals (Python
996 *emd* 0.6.2) using a box-car rolling window of 100 observations⁶³. Heart rate variability metrics
997 were computed after removing outliers, ectopic beats and interpolating missing values (Python
998 *Aura-healthcare hrvaranalysis*). Both time-domain features (standard deviation (SD) of the inter-
999 beat-interval of normal sinus beats, *snnn*) and frequency-domain features using the Lomb-
1000 Scargle periodogram [ref] (low-frequency signal power *lf* between 0.04-0.15 Hz considered a
1001 mixture of sympathetic and parasympathetic activity, high-frequency signal power *hf* between
1002 0.15-0.4 Hz representing beat-to-beat changes from parasympathetic vagal activity, and the
1003 low-frequency to high-frequency ratio (*lf-hf-ratio*) were computed⁶⁴.

1004 The device inertial-measurement units (IMU) were located inside the left and right ear canal and
1005 provided left and right cartesian coordinates of acceleration measured in milli-g where 1,000
1006 milli-g is the acceleration caused by earth's gravitational force. Each in-ear component from the
1007 device is uniquely and reproducibly oriented on account of the ellipsoidal shape of the human

1008 ear-canal and the matching shape of the in-ear component. From this orientation, head position
1009 and motion (acceleration) were resolved from each set of IMU samples that included gross
1010 positions such as *supine*, *reclined*, *upright*, *left* and *right*.

1011

1012 ***Clinical Study Design***

1013 The Investigational Device was evaluated in two studies, a Benchmarking Study conducted in
1014 The Villages community in Florida in partnership with the UF Health PHRC, and a Replication
1015 Study conducted at the University of Washington in Seattle. These studies were reviewed and
1016 approved by University of Florida Institutional Review Board (IRB No. 202201364) and Western
1017 Institutional Review Board (IRB No. 20225818), respectively. Written informed consent was
1018 obtained from all study participants during a screening visit, prior to any study activities.

1019

1020 ***Participant Recruitment***

1021 Following distribution of study flyers in public-facing locations in senior recreation and/or local
1022 medical centers, the Benchmarking Study enrolled 34 healthy participants 56-66 years of age
1023 and the Replication Study enrolled 14 healthy participants 49-63 years of age. Participants were
1024 cognitively intact and had no history of clinical depression, confirmed during screening using the
1025 Montreal Cognitive Assessment (MOCA) and Geriatric Depression Scale (GDS). Other
1026 exclusion criteria included a history of diabetes, hypertension, coronary artery disease,
1027 pulmonary disease, neurological disease, or anxiety. Participants planning travel to alternate
1028 time zones within two weeks of study participation were also excluded. Consolidated Standards
1029 of Reporting Trials (CONSORT) diagram for the Benchmarking Study and Replication Study is
1030 provided in **Figure 3** (bottom), and participant exclusions are detailed in the Results section.

1031 Demographic data including age, sex, APOE4 allele status, MOCA and GDS for the

1032 Benchmarking Study, Replication Study, and Combined Studies are provided in **Supplemental**

1033 **Table 1.**

1034

1035 *Study Protocol*

1036 As shown in the study schematic (**Figure 3**, top), this is a cross-over study in which participants
1037 took part in two overnight study visits, one undergoing normal sleep and the other undergoing
1038 overnight sleep deprivation, at a 2-4 week interval. Each overnight study visit consisted of three
1039 study periods beginning at 1900 hrs, 0700 hrs, 1330 hrs separated by two intervals – an
1040 overnight interval (2300-0630 hrs), and a morning interval (0800-1130 hrs).

1041

1042 Benchmarking Study: Beginning with arrival to the study suite at 1900, participants underwent a
1043 blood draw for APOE genotyping and assessment of amyloid β and tau biomarkers ($A\beta_{1-40}$, $A\beta_{1-42}$,
1044 phospho-tau181, phospho-tau217, non-phospho-tau181, non-phospho-tau217; C₂N
1045 Diagnostics⁶⁵⁻⁶⁷) and 60 min of non-contrast magnetic resonance imaging (MRI) scanning
1046 (sequences detailed below). On completion, participants were instrumented for commercial
1047 polysomnography (PSG, Philips Resironics Alice 6 LDx Diagnostic Sleep System) that
1048 included a 10-20 EEG montage with electro-oculogram (EOG) and submental electromyogram
1049 (EMG). Electrode impedances were required to be below 5 k Ω . Participants were last
1050 instrumented with the Investigational Device, and device electrode impedances required to be
1051 below 5 k Ω .

1052

1053 The Overnight interval lasted from 2300-0630 hrs the following morning. To support study
1054 planning, participants were randomized to undergo either normal sleep or sleep deprivation for
1055 their initial overnight visit following completion of their informed consent, however this
1056 information was not shared with the participants. To reduce likelihood of preparation bias on the
1057 part of participants (i.e. altering sleep schedules or taking naps in anticipation of sleep
1058 deprivation visits) participants were not informed of their initial visit assignment until 4pm the

1059 day of their arrival. Both PSG and Investigational Device recordings took place continuously
1060 throughout the Overnight interval. Throughout the overnight period, sleep-assigned participants
1061 were allowed to sleep normally without interruption. Participants assigned to the sleep
1062 deprivation were monitored by study staff to ensure adherence to the sleep deprivation protocol.
1063
1064 Between 0700-0745 hrs the next morning, all participants were administered a cognitive battery
1065 that included the 5-minute psychomotor vigilance test for sustained attention^{68,69}, symbol-digit
1066 modality test of processing speed, trail making test part A and part B for assessing executive
1067 function⁷⁰, and digit span forward test of working memory⁷¹. Following the cognitive battery,
1068 participants underwent a blood draw for amyloid β and tau biomarkers and a second non-
1069 contrast MRI scanning session (denoted T₀ in Results section). Immediately following the
1070 second non-contrast MRI scan, participants underwent intravenous gadolinium-based contrast
1071 agent (GBCA) injection (Gadavist, 0.1 mmol/kg), followed by T1- and T2-weighted contrast-
1072 enhanced MRI scans 7-10 min after GBCA injection (denoted T₁₀ in Results section).
1073
1074 Participants were escorted back to the study suite where they were re-instrumented with the
1075 commercial PSG and the Investigational Device. The Morning Interval ran from 0800 to 1130.
1076 Participants who assigned to the sleep condition in the Overnight Interval were required to
1077 remain awake and were monitored by study staff to ensure adherence; those assigned to the
1078 sleep deprivation condition in the Overnight were allowed to sleep. During this interval both the
1079 PSG and Interventional Device recorded data. The third assessment period commenced at the
1080 end of the Morning Interval. Participants underwent a final blood draw for amyloid β and tau
1081 biomarker assessment and then had a third MRI scanning session, including non-contrast
1082 sequences and T1- and T2-weighted contrast-enhanced sequences at approximately 4 hrs
1083 post-GBCA injection (denoted T₂₄₀ in Results section).

1084

1085 Replication Study: The Replication protocol was an abridged version of the Benchmarking
1086 protocol. The inclusion/exclusion criteria were identical to the Benchmarking study except for
1087 the lower age cut-off. Participants were similarly randomized to a night of sleep or a night of
1088 sleep deprivation on their first visit, with a crossover to the alternative sleep/sleep deprivation
1089 assignment on their second visit. The protocol for the Replication Study was identical to that of
1090 the Benchmarking Study excepting that 1) Participants did not undergo commercial PSG, sleep
1091 was assessed by Investigational Device EEG; 2) Participant sleep deprivation adherence in the
1092 Overnight Interval was assessed retrospectively using the sleep EEG; 3) The cognitive battery
1093 did not include the digits forward working memory test; 4) Participants underwent only non-
1094 contrast, and not contrast-enhanced MRI.

1095

1096 Cognitive Assessments: The 5-minute PVT from Texas A&M University System CSE⁷² and
1097 digits forward recall from Cambridge Cognition⁷¹ were administered on an iPad. The paper-
1098 based SDMT from Western Psychological Services⁷³, the TMT A and TMT B⁷⁴, were
1099 administered by a clinical coordinator trained in administering these tests. The cognitive battery
1100 was administered in a quiet room with minimal distractions on the morning following sleep/wake
1101 and prior to the neuroimaging and phlebotomy. The administration of each test was preceded by
1102 the corresponding practice test. We have included a description of these tests within the overall
1103 protocol for completeness. The results of these cognitive tests, and their relationship to
1104 Investigational Device outputs, sleep parameters, fluid biomarkers, and MRI measures of
1105 glymphatic function will be reported elsewhere.

1106

1107 Plasma Biomarkers: The APOE genotyping, amyloid β and tau plasma biomarkers were
1108 analyzed using mass spectrometry by C₂N Diagnostics⁷⁵. The sample collection procedure was
1109 provided by C₂N Diagnostics. Venipuncture and blood draw from the antecubital fossa were

1110 performed using a 22-gauge butterfly needle to minimize red blood cell hemolysis. A total of 10
1111 ml of blood was drawn into a K₂ EDTA Vacutainer. The blood was centrifuged for 15 min using a
1112 swinging bucket rotor at 500-700 x g with the brake on. Immediately after centrifugation, four 1.0
1113 mL plasma samples were aliquoted into four Sarstedt 2.0 ml Micro Tube without disrupting the
1114 plasma/cell interface when transferring plasma. A calibrated air-displacement hand-held pipette
1115 with a polypropylene pipette tip was used. After aliquoting plasma into the Sarstedt Micro
1116 Tubes, the tubes were immediately capped and frozen at -40°C. When the tubes were ready to
1117 be shipped to C₂N Diagnostics, they were packed into a plastic zip-lock bag with plenty of dry
1118 ice, placed in an absorbent towel and cryobox, and express couriered to C₂N Diagnostics
1119 priority overnight. In the present report, we utilize APOE4 allele status as a covariate in our
1120 analysis, and we have included a description of plasma biomarker assessment within the overall
1121 protocol for completeness. However, the fluid biomarker levels, and their relationship to
1122 Investigational Device outputs, sleep parameters, cognitive tests, and MRI measures of will be
1123 reported elsewhere.

1124

1125 *Magnetic Resonance Imaging Approach*

1126 MRI scanning at The Villages site was conducted on a 3T Siemens Vida system at Lake
1127 Medical Imaging, while scanning at the University of Washington site was conducted on a 3T
1128 Philips Ingenia Elition X at the Diagnostic Imaging Sciences Center. In the present report, to
1129 define the relationship between brain R_P and glymphatic function, we utilize CE-MRI from
1130 Benchmarking Study participants following the overnight sleep condition. We have included a
1131 description of the other MRI-based approaches within the overall protocol for completeness.
1132 However, the relationship between these different MRI measures of glymphatic function,
1133 Investigational Device outputs, sleep parameters, cognitive tests, and fluid biomarker levels will
1134 be reported elsewhere.

1135

1136 Contrast-Enhanced MRI: Contrast-enhanced MRI involves intravenous administration of a
1137 Gadolinium chelate that shortens T1, T2, and T2* relaxation parameters of the tissue it
1138 traverses through. Specifically, in this study, shortening of the T1 relaxation parameter
1139 enhances MRI signal that is proportional to the amount of Gadolinium and its characteristic
1140 relaxivity. Gadolinium passes quickly through the cerebral and peripheral vasculature within the
1141 first 5-30 minutes. A fraction of the contrast enters the CSF and ISF^{14,15} over many hours and
1142 finally almost 99% of the contrast exits the body by renal clearance. The passage of intravenous
1143 GBCA from the vasculature to the CSF and ISF was measured in terms of a delayed signal
1144 enhancement at approximately 4 hours after administration. Two prior studies have shown that
1145 delayed enhancement following contrast injection between 3 and 6 hours is indicative of solute
1146 (in this case, GBCA) transport via the CSF-ISF glymphatic exchange^{14,15}. At the Villages®, we
1147 performed 3D T1-weighted magnetization-prepared rapid acquisition with gradient echo
1148 (MPRAGE) with TR/TI/TE = 2300/900/2 ms, resolution = $1 \times 1 \times 1$ mm³, field-of-view =
1149 $256 \times 256 \times 208$ mm³, total acquisition time = 5:12 min before contrast injection. The post-contrast
1150 MRI image (T₁₀) was acquired approximated 7-10 minutes after contrast injection and its
1151 acquisition was identical to the pre-contrast image. A second post-contrast scan was acquired
1152 about 4 hours (T₂₄₀) later using identical imaging parameters.

1153
1154 Structural MRI: Structural T1 MRI was used for classifying the brain tissue into lobar gray
1155 matter, lobar white matter, and CSF as well as for segmenting regions-of-interests including the
1156 hippocampus, sagittal sinus, internal carotid arteries, lateral ventricle, and subarachnoid space.
1157 The T1 images were also used for registration purposes for all other imaging modalities. The T1
1158 images were used for determining PVS morphometry^{76,77}. Scanning parameters for the
1159 Benchmarking Study are identical to the contrast-enhanced MRI. Scanning parameters for the
1160 Replication Study were TR/TI/TE = 12/1000/4.5 ms, resolution = $0.8 \times 0.8 \times 0.8$ mm³, field-of-view

1161 = 256×240×166 mm³, total acquisition time = 5:24 min. Since inclusion of T2 MRI significantly
1162 improves PVS detection, a T2 MRI with TR/TE = 3200/561 ms, resolution = 0.8×0.8×0.8 mm³,
1163 field-of-view = 256×240×166 mm³, total acquisition time = 4:32 min was also added.

1164

1165 Intravoxel Incoherent Motion MRI: Intravoxel incoherent motion (IVIM) MRI is a multi-shell
1166 diffusion imaging approach to measure water movement at different scales of distance and time.
1167 Glymphatic transport includes movement of CSF in the subarachnoid space and the interstitium
1168 at a slow speed (~1 mm/s) over large distances (~100-200 μm)^{1,30,40}. This perivascular
1169 movement of CSF through the subarachnoid compartment is upstream of its exchange with the
1170 ISF along the penetrating intraparenchymal vasculature and hence could serve as an important
1171 correlate of glymphatic function⁷⁸. The imaging parameters for the Benchmarking Study were:
1172 TR/TE = 5500/124 ms, resolution = 1×1×5 mm³, field-of-view = 250×250×150 mm³, parallel
1173 imaging factor = 2, multi-band factor = 3, fat suppression with Spectral Presaturation with
1174 Inversion Recovery (SPIR), b values = 0, 50, 100, 150, 200, 250, 300, 350, 400, 500, 700, 800,
1175 and 1000 s/mm², and total acquisition time = 7:01 min. The b = 0 s/mm² was acquired with
1176 reverse phase encoding to correct for field distortions. The imaging parameters for the
1177 Replication Study were TR/TE = 2978/90 ms, resolution = 1×1×5 mm³, parallel imaging factor =
1178 2.2, field-of-view = 230×196×115 mm³, fat suppression with SPIR, b values = 0,
1179 10, 40, 80, 100, 150, 200, 300, 500, 700, 800, 900, 1000 s/mm², and total acquisition time = 8:08
1180 min. A Split echo (SPLICE) acquisition was used to eliminate the need for distortion correction.

1181

1182 Multi-Echo, Multi-Delay Arterial Spin Labeling (ASL) MRI: Multi-echo, multi-delay ASL measures
1183 perfusion and time for exchange of water across the endothelium. This time metric is dependent
1184 on perfusion, endothelial permeability, and the glial vascular unit including the AQP4 water
1185 channels that are critical to the perivascular CSF-ISF exchange^{78,79}. This protocol was

1186 implemented only for the Replication Study as a Hadamard-encoded ASL acquisition, TR/TE =
1187 5000 ms, resolution = $1 \times 1 \times 5 \text{ mm}^3$, field-of-view = $230 \times 196 \times 115 \text{ mm}^3$, post labeling delay = 650,
1188 950, 1210, 1510, 2083, 2383 ms with background suppression, label duration = 3400 ms, and TE
1189 = 0, 40, 80, 120 ms. Total acquisition time = 12:40 min. A conventional arterial spin labeling
1190 (ASL) protocol was implemented in the Benchmarking Study due to the lack of availability of the
1191 multi-echo component. The parameters were: TR/TE = 4420/22 ms, resolution = $1.7 \times 1.7 \times 4$
1192 mm^3 , field-of-view = $220 \times 220 \times 96 \text{ mm}^3$, post labeling delay = 500,
1193 900, 1000, 1100, 1200, 1400, 1600, 1800, label duration = 1800 ms. Total acquisition time = 2:37
1194 min. The sequence was acquired twice. A reference M0 images was acquired in both studies
1195 with identical parameters but without background suppression or labeling.

1196

1197 Fast Functional MRI: A sub-second functional MRI sequence was implemented to separate and
1198 regress physiological noise (cardiac and respiratory signals) as well as to capture slow CSF
1199 oscillations in the ventricles⁸⁰. The protocol for the Benchmarking Study was TR/TE = 400-
1200 500/30 ms, resolution = $3.6 \times 3.6 \times 3.6 \text{ mm}^3$, flip angle = 70° , multi-band factor = 4, field-of-view =
1201 $230 \times 2430 \times 101 \text{ mm}^3$, fat suppression, no. of volumes = 365 using SPIR, total acquisition time =
1202 2:37 min. Heart rate and respiration were monitored using the BIOPAC MR160 and
1203 synchronized with MRI acquisition. The Replication Study used a gradient-echo, echo planar
1204 imaging sequence with TR/TE = 400-500/30 ms, resolution = $3 \times 3 \times 4 \text{ mm}^3$, flip angle = 42° , multi-
1205 band factor = 6, field-of-view = $240 \times 240 \times 123 \text{ mm}^3$, slice gap = 0.4 mm, fat suppression using
1206 SPIR, no. of volumes = 450, total acquisition time = 3:00 min. Two single volume, spin echo
1207 acquisitions were also acquired with opposite phase encoding to allow for distortion correction.
1208 Heart rate and respiration were monitored using the sensors built into the Philips scanner and
1209 synchronized with MRI acquisition. Glymphatic CSF-ISF exchange is at least partly driven by
1210 vasomotion, which may be reflected by periodic motion in the CSF spaces. This CSF motion

1211 correlates well with sleep stages, with power of the slow CSF oscillation increasing from
1212 wakefulness to the N1 and finally to the N2 stage⁸⁰.

1213

1214 Phase-Contrast MRI: The phase contrast MRI is used to quantify CSF efflux from the Aqueduct
1215 of Sylvius. The peristaltic motion of CSF at the Aqueduct is measured by gating the MRI signal
1216 to the participants and calculating the CSF motion into and out of the brain over a cardiac
1217 signal. Variations in CSF efflux velocity appear to follow the cardiac and respiratory signals and
1218 may impact glymphatic CSF-ISF exchange. The Benchmarking Study protocol for this MRI was
1219 the following: a single slice acquisition perpendicular to the Aqueduct of Sylvius, TR/TE = 21/6.6
1220 ms, resolution = 30.6×0.6×6 mm³, flip angle = 10°, 40 phases per cardiac cycle, and velocity
1221 encoding for 12 cm/s, total acquisition time: 2:00 min. The Replication Study protocol included
1222 the following: a single-slice acquisition perpendicular to the Aqueduct of Sylvius, TR/TE = 12/7.9
1223 ms, resolution = 30.6×0.6×4 mm³, flip angle = 10°, 15 phases per cardiac cycle, and velocity
1224 encoding for 12 cm/s, total acquisition time: 2:02 min

1225

1226 *Statistical Approach*

1227 The Benchmarking study was designed to have 80% power at a significance level of 5% to
1228 detect a low-to-moderate correlation r ($r=0.5$) between the device measurements and CE-MRI
1229 measurement of glymphatic function. The Replication study was designed to have 80% power
1230 at a significance level of 20% to detect a low-to-moderate correlation r ($r=0.5$) between the
1231 device measurements and non-contrast MRI measurement of glymphatic function and to detect
1232 overnight sleep/wake differences in brain parenchymal resistance.

1233

1234 The parenchymal resistances R_p computed from each EIS scan from the device were
1235 normalized to the sleep/wake onset values to allow comparison across visits and participants.

1236 To reduce measurement variability of the sleep/wake onset value, the value was inferred from a
1237 linear regression to the initial R_P values. The overnight change in R_P per participant visit was
1238 taken as the average of the normalized values for that visit. For example, a value of 1 indicated
1239 that there was no overnight change from the onset value and a value of 0.8 indicated a 20%
1240 overnight reduction from onset. A Student's T-test group comparison between sleep/wake visits,
1241 group mean and SD were calculated.

1242

1243 Contrast-enhanced MRI of sleep-related glymphatic function was analyzed using a random
1244 intercept linear mixed effect model (R, lme in the lme package). Glymphatic function was
1245 defined by measuring brain parenchymal contrast enhancement, the % change in T1-weighted
1246 signal intensity between 10-240 min post-GBCA injection ($100\% * (T_{240}-T_{10})/T_0$) at each of eight
1247 regions of interest (ROIs): frontal cortical gray and white matter, parietal cortical gray and white
1248 matter, temporal cortical gray and white matter, and occipital gray and white matter. Only sleep
1249 visits were analyzed leading to a one level of grouping, the eight ROIs, for the participant sleep
1250 visit. All models included regressors in the mixed model for the $T_{10}-T_{240}$ change in blood signal
1251 within the internal carotid artery, and the $T_{10}-T_{240}$ change in CSF signal within the cerebral
1252 lateral ventricles to compensate for the influence of vascular and CSF contrast on parenchymal
1253 enhancement. Potentially confounding biological variables age, gender, and APOE $\epsilon 4$ status
1254 were also included in all models.

1255

1256 To evaluate different sleep-related contributions to glymphatic function, overnight changes from
1257 sleep onset for each of the four recorded EEG relative band powers (delta, theta, alpha, beta)
1258 and for HR were computed. The recorded values were normalized to their respective value at
1259 sleep onset and a single statistic, the average of the overnight normalized values, computed per
1260 participant visit. The four hypnogram sleep stages (N1, N2, N3, REM) and WASO were each
1261 summed into single total sleep stage durations and total WASO duration per participant visit.

1262 The device R_P normalization and averaging has been previously described. Models were run
1263 separately for each of the four EEG relative band powers (delta, theta, alpha, beta), for each of
1264 the four hypnogram sleep stages (N1, N2, N3, REM), for WASO, for HR and for device R_P . Two
1265 full models were then fit to the data, with the EEG band power and the hypnogram sleep stages
1266 separated into distinct models because of collinearity across those predictors. The variance
1267 inflation factor (R 'vif' function from the 'car' package) was used to test for predictor collinearity
1268 using a threshold of 5. The EEG powerbands included were limited to delta, theta and beta
1269 because of collinearity among the four relative band powers. HR and the device R_P were
1270 included in both full models. Each full model was reduced to a selected model using backward
1271 elimination of predictors with a threshold Wald's p-value of 0.05.

1272
1273 Model selection stability, or robustness of the selected model to perturbations in the dataset,
1274 was tested using resampling-based multi-model inference²⁹. The dataset was bootstrapped
1275 resampled with replacement to generate 500 bootstrapped datasets. For each of these datasets
1276 the two full models were estimated and reduced to a selected model using backward
1277 elimination. The bootstrap inclusion frequency (the percent of bootstrap datasets that included
1278 the predictor), the RMSD ratio (the RMSD of the predictor bootstrap estimate divided by the
1279 standard error of that coefficient in the full model and expressing the variance inflation or
1280 deflation caused by variable selection), the relative conditional bias (quantifying the variable-
1281 selection-induced bias to expect if a predictor is selected) and the bootstrap median of each
1282 predictor coefficient were reported.

1283
1284 The analyses of device R_P values with EEG band powers, heart rate and hypnogram staging
1285 were performed on the overnight sleep recordings. Analyses were grouped into REM sleep and
1286 NREM sleep (N1, N2 and N3). The device resistances were computed repeatedly throughout
1287 the night from each EIS scan. During sleep recordings, these data were non-stationary. After

1288 normalization to sleep onset as previously described, first-order differences ΔR_P and ΔX for X
1289 one of the EEG band powers or HR were incorporated into individual random intercept linear
1290 mixed models to evaluate their relationship. Threshold regression models were used in the
1291 linear mixed model. A custom estimation procedure described in **Supplemental Information**
1292 was used to jointly estimate the threshold regression for the full positive and negative range of
1293 the predictors. The hinge threshold model was analytically reduced to estimation by linear
1294 regression which allowed it to be used in a random intercepts linear mixed effects regression
1295 model. The autocorrelation function and augmented Dickey Fuller tests were used to confirm
1296 stationarity of the differenced variables ΔR_P and ΔX and also of the fitted model residuals (R,
1297 acf and adf functions).

1298

1299 In addition to the analyses of ΔR_P and ΔX for X one of the EEG powerbands or HR during REM
1300 sleep and NREM sleep, these were analyzed at hypnogram transitions NREM to REM, REM to
1301 NREM, sleep to wake and wake to sleep. The analysis was similar, using threshold regression
1302 models in a random intercept mixed linear model.

1303

1304 Univariate outliers were trimmed at the 0.5 and 99.5 percentile. For multivariate analysis, the
1305 Mahalanobis distance was computed and outliers trimmed at the 0.5 and 99.5 percentile of the
1306 Mahalanobis distance. All regressions were adjusted for potential confounding effects of age,
1307 sex and APOE genotype. All tests were considered significant at a 5% level if the 95%
1308 confidence interval (CI) did not contain the null hypothesis. All statistical analyses were
1309 performed in R version 4.2.1 (2022-06-23) or Graphpad Prism 8.0.0.

1310

1311 We reported the pooled findings of the Benchmarking and Replication study for both the
1312 investigational device transcranial resistance measurements and EEG parameters.

1313

1314

1315 **SUPPLEMENTAL INFORMATION**

1316 ***Supplemental 1: Analysis of device EEG and commercial polysomnography***

1317 The single derivative device EEG was validated against the commercial PSG (Philips
1318 Respiroics Alice 6 LDx Diagnostic Sleep System) in participants that underwent concurrent
1319 device and PSG sleep recording as part of the Benchmark study. Both hypnogram sleep staging
1320 and sleep parameters were validated using a confusion matrix between the device prediction
1321 and the PSG prediction both per participant and pooled across participants. Prediction metrics
1322 computed included sensitivity, specificity, precision, accuracy and F1 score. The device EEG
1323 with EOM and the PSG C3-A2, C4-A1 derivatives were individually input into the automated
1324 hypnogram scoring (Python yasa 0.6.3 *SleepStaging*). Manual scoring of the PSG by a sleep
1325 physician (YC) was used as the gold-standard. The results of these comparisons are provided
1326 in **Supplemental Table 6**.

1327

1328 ***Supplemental 2: Threshold regression model and estimation***

1329 Threshold regression models were fit on data that spanned the full positive and negative range
1330 of abscissa values. These models are defined by a positive turning point $t_p \geq 0$ where for $x \geq$
1331 t_p the regression line goes from $f(x) = 0$ to $f(x) = m_p(x - t_p)$ and a negative turning point
1332 $t_n \leq 0$ where for $x \leq t_n$ the regression line goes from $f(x) = 0$ to $f(x) = m_n(x - t_n)$. These
1333 models can be reduced to linear regression. First transform the data $(x, y) \rightarrow (w, y)$ were

1334
$$w = \begin{cases} x - t_n & \text{if } x \leq t_n \\ 0 & \text{if } t_n < x < t_p \\ r(x - t_p) & \text{if } x \geq t_p \end{cases}$$

1335 For values of t_p , t_n and r , a least squares estimator can be used to fit a linear model to the
1336 transformed data values (w, y) . With $r = \frac{m_n}{m_p}$, the transformed data is linear, through the origin
1337 and has slope m_n . When $r = 1$ both slopes are identical; for $r \neq 1$ the positive half-space slope
1338 equals the regression estimate multiplied by r . Hence, for $r < 1$ the positive half-space slope is

1339 less than the negative half-space slope and for $r > 1$ the positive half-space slope is greater
1340 than the negative half-space slope.

1341

1342 The linear fit was estimated using an F-statistics, the ratio of the explained variance (due to the
1343 model) and the unexplained variance (residuals). Grid search over the parameter space t_p , t_n
1344 and r was carried out and the values that minimized the mean sum of squared residuals (and
1345 hence maximized the F-statistic) was reported⁸¹. To avoid edge effects, t_p and t_n were set to
1346 ± 1.5 standard deviations⁸². Random intercept linear mixed models were similarly fit to the
1347 transformed data and grid search used to solve for the parameters that minimized the mean
1348 sum of squared residuals for the fixed effects. The autocorrelation function was used to confirm
1349 no residual autocorrelation following model estimation and fit.

1350

1351

1352 ***Supplemental 3: Physiological basis for electrical impedance spectroscopy change with***
1353 ***glymphatic function.***

1354 In normal adult men (women) between the ages of 60-86 years, the GM, WM and total
1355 intracranial volumes (TIV) are 614.3 ± 60.1 (562.6 ± 50.1 ml), 534.0 ± 57.2 ml (476.6 ± 44.7 ml)
1356 and 1603.0 ± 133.0 ml (1425.9 ± 109.0 ml)⁸³. Average adult cerebral blood flow (CBF) is
1357 approximately 750 ml/min or 12.5 ml/sec. Assuming HR of 60 bpm, 12.5 ml of blood injected
1358 into the brain causes an approximate 50 m Ω decrease in the device IPG sampled at 80 kHz
1359 (see for example **Figure 2d**, IPG-Impedance Plethysmograph data taken from a female study
1360 participant). At 80 kHz, EIS measures the extracellular compartment and most of the
1361 intracellular compartment. Thus, the 12.5 ml increase in blood volume, representing a
1362 $12.5/1425.9 = 0.88\%$ change in TIV, would be measured as a 50 m Ω decrease in resistance by
1363 EIS.

1364

1365 At low frequencies, EIS measures changes in extracellular volume. The interstitial cortical
1366 volume fraction α in awake rodents has been shown to be 14.1% and in sleeping rodents 23.4%
1367 whereas the tortuosity λ of the interstitial space remained unchanged across sleep and wake^{2,84}.
1368 This suggests that in rodents, the sleep-induced volume expansion of the interstitial space
1369 occurs from a change in the cross-sectional area and not length. This is noteworthy because
1370 resistance of a conductor is proportional to $\frac{l}{A}$ where l is the length and A the cross-sectional
1371 area. Therefore, the increase in interstitial space fluid with glymphatic function will increase the
1372 cross-sectional area of the interstitial space channels and proportionally decrease the
1373 transcranial electrical resistance. In humans, the measurements range from 15-20%⁸⁵ but
1374 changes with sleep/wake have not been assessed. Using the rodent data as a proxy to what we
1375 might expect in humans, we would expect a 66% increase in interstitial volume with sleep to
1376 occur from of a 66% increase in cross-sectional area of the interstitial channels. The remaining
1377 extracellular compartment volumes contributing to the resistance at low EIS frequencies are
1378 CSF and blood plasma that occupy a total volume comparable to the awake interstitial volume.
1379 Therefore, the net extracellular compartment volume increase, or effective cross-sectional area
1380 increase, with sleep is 33%. Using the IPG relationship between fluid volume change and
1381 transcranial impedance, a 0.88% increase in fluid volume was measured as a 50 m Ω decrease
1382 in transcranial electrical resistance implying that a 33% volume increase would be measured as
1383 an 1875 m Ω decrease. This analysis uses the conclusion that the interstitial volume increase of
1384 glymphatic function is an increase in the interstitial channel cross-sectional area and similarly
1385 the assumption that the intravascular volume increase of cardiac output is from an increase in
1386 the intravascular cross-sectional area. The preceding analysis assumed a 66% increase in
1387 interstitial volume fraction as seen in rodents. Assuming a smaller 25% volume fraction increase

1388 and using the same analysis, we would expect a 710 m Ω decrease in transcranial resistance
1389 with sleep.

1390

1391 ***Supplemental 4: Benchtop and agar phantom characterization of electrodes and device.***

1392 Electrodes were characterized according to the ANSI/AAMI EC12 standard for AC impedance,

1393 DC offset voltage, combined offset instability and internal noise, and bias current tolerance⁵⁷.

1394 Defibrillation overload recovery was not tested as it is not relevant to the present application.

1395 Pairs of electrodes were immersed in a 140 mM NaCl solution, facing each other and separated

1396 by 3-4 mm. AC impedance at 10 Hz was measured using a multifunction DAQ module (Analog

1397 Discover 2, Digilent) configured for 2-point impedance measurement. An excitation voltage of

1398 100 millivolts peak-to-peak (mVpp) and a 10 k Ω series resistor guaranteed a maximum current

1399 of 10 microamps peak-to-peak (μ App). DC offset voltage was measured with a Fluke 87V

1400 multimeter. Offset instability and internal noise were measured over five minutes using a 24-bit

1401 digitizer module (ADS1299EVM, Texas Instruments, 67 nV resolution) sampling at 2000

1402 samples per second, calibrated using a Keysight EDU33212A Signal Generator. Recorded data

1403 was subsequently filtered with a 0.15-100 Hz first order bandpass (simulating EC12 filtering) or

1404 the 0.3-50 Hz EEG bandpass filter described in **Signal Processing –**

1405 **Electroencephalography**. Peak-to-peak values over the 5-minute period are reported. Bias

1406 current tolerance was measured with a multifunction DAQ module using its 14-bit digitizer

1407 (0.32 mV resolution) as data logger (sampling every 10 seconds for 8 hours), and its power

1408 supply to apply 200 nA DC across the pair of electrodes (2 V across a 10 M Ω resistor in series).

1409 The maximum voltage deviation relative to the initial offset voltage before current application is

1410 reported. All results are found in **Supplemental Table 7**.

1411

1412 Benchtop validation of the investigational device EIS compared the measured to the theoretical

1413 resistance and reactance at each frequency on a circuit model of brain parenchymal impedance

1414 (the load) with separate models for each of the four electrode impedances. The circuit diagram
1415 for these benchtop measurements is shown in **Supplemental Figure 2**. The load was modelled
1416 using 2R1C parallel circuit and the four electrode-skin interfaces were modeled by individual
1417 2R1C circuits with a charge transfer resistance in parallel to a double layer capacitance that was
1418 in series with a resistor embodying the electrolyte and stratum corneum resistance. The
1419 resistance and capacitance values for the load were based on observed participant resistance
1420 and reactance over the EIS frequencies. Two sets of parameters for the electrode impedance
1421 models were used, a low-impedance model and a high-impedance model. These were selected
1422 to cover the observed range of subject electrode impedances over the range of EIS frequencies.
1423 The parameters for the complete set of benchtop tests are found in **Supplemental Table 8** and
1424 included (i) calibration measurements of purely resistive loads, (ii) calibration of a 2R1C load
1425 varying the parallel resistor R_s to simulate changes in the interstitial space resistance, and (iii)
1426 calibration of a fixed 2R1C load while varying the electrode impedances at each electrode
1427 between low and high impedance settings to test the sensitivity to expected variations during
1428 use. The absolute error between the measured and theoretical resistance and reactance for the
1429 benchtop tests are reported in **Supplemental Table 9** and in **Supplemental Table 10**,
1430 respectively. The measured impedances reported were rotated by multiplying by the factor
1431 $e^{-j\omega T}$ with the value T chosen so that the reactance at 256kHz was zero⁵⁹. The absolute error of
1432 the resistance reveals a systematic positive bias implicating contributions to the resistance in
1433 the device or benchtop setup that were not fully compensated by the device calibration. For the
1434 measurements of the 2R1C benchtop tests, the resistance bias is 0.278 Ω and the bias un-
1435 adjusted and adjusted RMSE are 0.321 Ω and 0.144 Ω , respectively. The reactance did not
1436 show a systematic bias. The RMSE of the reactance for the 2R1C benchtop tests is 0.128 Ω .
1437 Because we are interested in the dispersion of the resistance over frequencies, or the difference
1438 between the resistance at a low frequency and at a high frequency, the bias cancels out. Using
1439 the signal processing pipeline to fit the Debye model, **Supplemental Table 11** reports the

1440 dispersion prediction error from theoretical value at each frequency relative to 128 kHz.
1441 Reported values are for the 2R1C electrode impedance sensitivity tests. The 1 kHz minus
1442 128kHz dispersion is representative of the parenchymal resistance R_P computed from the
1443 difference between the extrapolated DC resistance and the infinite frequency resistance. This
1444 dispersion had an RMSE of 0.147 Ω approaching the bias-adjusted RMSE of the 2R1C
1445 benchtop tests in **Supplemental Table 9**, and represents a 3.1% measurement error in the
1446 theoretical dispersion value of 4.766 Ω .

1447

1448 The device EIS showed the accuracy needed to reliably measure a single R_P value but to
1449 evaluate glymphatic function it needs to detect changes in R_P . These changes are small by
1450 comparison to the absolute value of R_P . As discussed, the overnight decrease ranges between
1451 500 m Ω and 2000 m Ω . With the current time-multiplexing settings, the device completes
1452 approximately 84 scans over a 7-hour night of sleep, or 6 to 23 m Ω average decrease between
1453 scans. The statistical models used in the analysis of the Benchmarking Study and Regression
1454 Study required significance testing of the mean change in R_P between sleep and wake, and
1455 testing significance of predictors of R_P in linear mixed models. These tests depend on the SD of
1456 the Debye model dispersion estimate which for the electrode impedance sensitivity tests was
1457 0.113 Ω , slightly less than the bias-adjusted RMSE. **Supplemental Table 12** shows that the
1458 minimum change in R_P with 25 and 100 EIS scans that is statistically significant is 44 m Ω and
1459 22 m Ω , respectively. Note that during sleep, R_P decreases with glymphatic function and
1460 therefore each measurement arises from a distribution with a different mean but the same SD
1461 σ . Using the linearity of expectation and statistical independence of each R_P measurement, the
1462 standard error of the mean of R_P is $\frac{\sigma}{\sqrt{n}}$ for n samples. Using the Fisher transform⁸⁶ to solve for
1463 the minimum significant correlation detectable at a given sample size, **Supplemental Table 11**
1464 reports that weak to moderate correlations of R_P with predictors will be significant at 100 and 25

1465 EIS scans, respectively. These estimates are optimistic since not all sources of error are
1466 accounted by the electrode impedance sensitivity tests.

1467
1468 Agar phantom testing over 12 hours was used as a final quality check for each fully assembled
1469 device. These tests measured the device combined noise level from the electronics,
1470 electrochemical interfaces between the electrodes, EEG gel and agar. **Supplemental Figure 3**
1471 shows the device periodogram, EEG recording and power spectral density from an agar
1472 phantom test.

1473

1474 **Data availability**

1475 The data supporting the results in this study are available from the corresponding author with
1476 Institutional Review Board approval and Data Use Agreement permitting non-commercial use of
1477 data for independent validation, publication and sharing of new findings.

1478

1479 **Code availability**

1480 Code used for the analysis and to produce figures are available upon reasonable request to the
1481 corresponding author.

1482

1483

1484 **Supplemental Table 1. Demographic, genetic and psychometric results of the**
1485 **Benchmarking Study, Replication Study and Combined Study.**
1486

	Benchmarking Study	Replication Study	Combined Study
N	30	14	44
Age ± SD (Range)	61.8 ± 2.7 (56, 66)	55.6 ± 4.6 (49, 63)*	59.8 ± 4.4 (49, 66)
Female (Male)	14 (16)	7 (7)	21 (23)
APOEε4 (not APOEε4)	8 (22)	5 (9)	13 (31)
MoCA ± SD (Range)	27.8 ± 1.1 (26, 30)	28.6 ± 1.2 (26, 30)	28.1 ± 1.2 (26, 30)
GDS ± SD (Range)	0.7 ± 1.1 (0, 4)	0.6 ± 1.2 (0, 4)	0.7 ± 1.1 (0, 4)

1487 Montreal Cognitive Assessment, MoCA; Geriatric Depression Scale, GDS. *P<0.001
1488 Benchmarking vs. Replication Study, unpaired t-test.

1489 **Supplemental Table 2. EEG band power, hypnogram, and R_p as individual predictions of parenchymal contrast**
 1490 **enhancement when added to the null model following overnight sleep.**
 1491

	Predictor	Estimate	95% CI	P Value	LRT	LRT P Value
Predictors Added to Null Model	Delta Band Power	19.121	(5.482, 32.760)	0.007	7.50	0.006
	Theta Band Power	-3.755	(-11.982, 4.473)	0.378	0.81	0.368
	Alpha Band Power	-7.279	(-12.264, -2.294)	0.005	8.12	0.004
	Beta Band Power	-5.329	(-7.786, -2.873)	<0.001	17.49	<0.001
	Heart Rate	-21.624	(-49.814, 6.566)	0.139	2.28	0.131
	WASO Time	-0.003	(-0.045, 0.038)	0.881	0.02	0.879
	N1 Sleep Time	-0.128	(-0.213, -0.042)	0.004	8.46	0.004
	N2 Sleep Time	-0.031	(-0.071, 0.009)	0.139	2.28	0.131
	N3 Sleep Time	0.025	(-0.024, 0.075)	0.322	1.02	0.313
	REM Sleep Time	0.031	(-0.023, 0.086)	0.268	1.28	0.258
	Parenchymal Resistance	-38.080	(-61.348, -14.812)	0.002	10.15	0.001
Null Model Fixed Effects	Blood CE	10.29	(5.45, 15.13)	<0.001	-	-
	CSF CE	148.48	(123.40, 173.56)	<0.001	-	-
	Age	-1.31	(-1.91, -0.71)	<0.001	-	-
	Male Sex	-2.69	(-5.42, 0.063)	0.060	-	-
	APOE ε4	-3.29	(-6.50, -0.091)	0.048	-	-
Null Model Random Effects	σ^2	70.50	-	-	-	-
	T ₀₀ ROI	12.60	-	-	-	-

1492 Wake After Sleep Onset, WASO; Rapid Eye Movement, REM; Confidence Interval, CI; Likelihood Ratio Test, LRT. **Bolded P values**
 1493 **reflect significant associations at P < 0.05.** Likelihood ratio test taken between null model and model with predictor.
 1494

1495
1496
1497

Supplemental Table 3. Multivariate models of morning brain parenchymal contrast enhancement using overnight and morning Rp, HR and EEG hypnogram predictors.

Predictor Period	Fixed Effect Predictors	Full Model			Selected Model			Bootstrap Analysis			
		Estimate	CI	p	Estimate	CI	p	Bootstrap Inclusion Frequency (%)	RMSD Ratio	Relative Conditional Bias (%)	Bootstrap Median
Overnight Sleep Opportunity	Blood CE	0.87	-5.26, 7.00	0.786	–	–	–	11.6	2.14	386.83	0
	CSF CE	221.86	185.38, 258.34	<0.001	225.82	(208.18, 243.47)	<0.001	100.0	0.94	0.01	225.13
	Age	-0.30	-0.82, 0.23	0.286	–	–	–	39.8	1.86	107.95	0
	Male Sex	-2.70	-5.77, 0.36	0.094	–	–	–	41.8	1.07	53.57	0
	APOE ε4	-4.60	-7.86, -1.35	0.008	-5.33	(-8.34, -2.31)	0.001	81.6	0.98	16.33	-4.77
	R _p	-76.16	-99.79, -52.53	<0.001	-67.17	(-87.78, -46.56)	<0.001	100.0	1.16	-5.30	-72.57
	REM Time	0.16	0.08, 0.24	<0.001	0.16	(0.09, 0.23)	<0.001	99.0	1.06	1.30	0.16
	N1 Time	-0.30	-0.43, -0.16	<0.001	-0.32	(-0.43, -0.21)	<0.001	98.8	1.09	0.95	-0.31
	N2 Time	-0.10	-0.14, -0.05	<0.001	-0.10	(-0.15, -0.06)	<0.001	98.0	0.80	-1.01	-0.10
	N3 Time	-0.09	-0.15, -0.03	0.004	-0.07	(-0.12, -0.02)	0.007	86.8	0.72	-1.15	-0.08
	WASO Time	-0.07	-0.13, -0.01	0.037	-0.07	(-0.12, -0.02)	0.006	78.6	0.74	21.00	-0.07
Heart Rate	-13.08	-44.72, 18.57	0.432	–	–	–	24.2	1.84	133.52	0	
Morning Sleep Opportunity	Blood CE	11.33	6.39, 16.28	<0.000	10.84	(5.98, 15.71)	<0.001	98.6	0.97	-5.49	10.59
	CSF CE	132.86	101.23, 164.50	<0.000	140.28	(113.86, 166.71)	<0.001	100.0	1.04	1.82	135.82
	Age	-0.81	-1.47, -0.144	0.022	-0.95	(-1.55, -0.34)	0.003	75.8	1.28	38.20	-0.94
	Male Sex	-4.27	-7.73, -0.82	0.020	-3.24	(-5.93, -0.55)	0.023	69.0	0.84	9.25	-3.57
	APOE ε4	-13.22	-23.65, -2.79	0.017	-9.25	(-13.20, -5.29)	<0.001	92.6	1.06	-13.49	-9.74
	R _p	38.06	7.87, 68.24	0.018	34.42	(5.25, 63.59)	0.025	65.4	0.81	20.18	37.42
	REM Time	0.58	0.10, 1.06	0.024	0.41	(0.20, 0.62)	<0.001	88.2	1.00	-14.04	0.40
	N1 Time	-0.28	-0.59, 0.02	0.080	-0.26	(-0.50, -0.02)	0.040	61.6	0.93	36.23	-0.29
	N2 Time	-0.11	-0.24, 0.022	0.116	-0.13	(-0.26, -0.01)	0.051	41.4	1.30	63.35	0
	N3 Time	-0.18	-0.37, 0.00	0.063	-0.17	(-0.33, -0.021)	0.031	44.2	0.65	15.70	0
	WASO Time	0.19	-0.10, 0.56	0.344	–	–	–	33.4	1.53	57.53	0
Heart Rate	-23.75	-107.49, 59.98	0.591	–	–	–	18.2	2.01	-28.96	0	

1498 Electroencephalography, EEG; Parenchymal Resistance, R_p; Heart Rate, HR; Contrast Enhancement, CE; 95% Confidence Interval,
1499 CI; Backward Elimination, BE; Root-Mean Square Deviation, RMSD; within ROI variability, σ^2 ; inter-ROI variability, T_{00 ROI}. **Bolded P**
1500 **values reflect significant associations at P < 0.05.** Shaded cells demark the **null model** that includes blood CE, CSF CE and
1501 potential biological confounders.
1502

1503
1504
1505
1506
1507

Supplemental Table 4. The change in parenchymal resistance resulting from large changes in EEG band power and heart rate during REM sleep, NREM sleep and wake for each study.

Study / Condition	Sleep Stage	Predictors	Fixed Effects				Threshold Model Parameters		
			Estimate	CI	p	DF	Positive Threshold	Negative Threshold	Slope Ratio
Benchmarking Study / Overnight Sleep Op	REM	Δ delta	-0.42	(-0.62, -0.21)	<0.001	240	1.28	-1.5	2
		Δ theta	-0.41	(-0.91, 0.082)	0.105	240	1.5	-1.3	0.5
		Δ alpha	-0.05	(-0.21, 0.10)	0.504	240	1.5	-0.08	2
		Δ beta	0.54	(0.16, 0.91)	0.006	240	1.5	-1.35	0.5
		Δ HR	0.10	(-0.26, 0.47)	0.588	202	1.5	-0.9	0.5
	NREM	Δ delta	-0.21	(-0.46, 0.039)	0.099	1038	1.5	-1.5	0.95
		Δ theta	-0.12	(-0.33, 0.090)	0.263	1038	1.23	-1.43	0.5
		Δ alpha	-0.14	(-0.30, 0.0063)	0.061	1038	1.5	-1.23	0.98
Benchmarking Study / Overnight Sleep Deprivation	WAKE	Δ delta	-0.07	(-0.18, 0.046)	0.243	631	0.75	0	0.5
		Δ theta	-0.08	(-0.17, 0.0084)	0.076	631	0.73	-1.5	2
		Δ alpha	0.07	(-0.049, 0.19)	0.245	631	1.5	0	0.5
		Δ beta	0.05	(-0.15, 0.26)	0.601	631	1.5	-1	0.83
		Δ HR	-0.10	(-0.20, 0.0017)	0.055	596	0.05	0	0.5
Replication Study / Overnight Sleep Op	REM	Δ delta	-0.69	(-1.1, -0.33)	0.000	78	1.43	-1.38	2
		Δ theta	-0.23	(-0.39, -0.074)	0.006	78	0.1	-1.5	2
		Δ alpha	-0.19	(-0.46, 0.084)	0.183	78	1.1	-0.1	1.25
		Δ beta	0.27	(-0.13, 0.68)	0.196	78	1.48	-0.45	1.08
		Δ HR	1.08	(0.45, 1.7)	0.001	68	1.5	-1.23	0.9
	NREM	Δ delta	-0.32	(-0.57, -0.064)	0.015	341	1.5	-0.8	0.6
		Δ theta	0.03	(-0.043, 0.11)	0.379	341	0	-1.5	2
		Δ alpha	0.03	(-0.049, 0.11)	0.482	341	0.03	-1.5	2
Replication Study / Overnight Sleep Deprivation	WAKE	Δ beta	0.13	(0.045, 0.22)	0.003	341	0.38	-1.5	2
		Δ HR	0.05	(-0.14, 0.25)	0.602	294	0.63	-1.5	1.13
		Δ delta	0.04	(-0.075, 0.16)	0.479	505	0.8	-1.5	2
		Δ theta	0.03	(-0.043, 0.096)	0.460	505	0	-1.5	2
		Δ alpha	0.09	(-0.063, 0.25)	0.247	505	1.15	-1.5	2
Δ beta	0.18	(0.031, 0.34)	0.019	505	1.48	-1.43	2		
Δ HR	-0.11	(-0.27, 0.056)	0.204	405	1	-0.35	0.88		

1508
1509
1510
1511
1512
1513
1514
1515
1516
1517

Rapid eye movement, REM; non-REM, NREM; Confidence Interval, CI; Degrees of Freedom, DF; EEG band power predictor units in percent of total band power; HR predictor units beats-per-minute. **Bolded P values reflect significant associations at P < 0.05.** Predictor and parenchymal resistance values in regression models were scaled to zero mean and unit standard deviation to simplify effect size comparisons across predictors. Positive and negative thresholds are in units of predictor standard deviation. Models included confounding biological variables age, gender, and APOE ϵ 4 status.

1518 **Supplemental Table 5. The change in parenchymal resistance resulting from large**
 1519 **changes in EEG band power and heart rate at NREM-REM and sleep-wake transitions for**
 1520 **each study.**
 1521

Study	Transition	Fixed Effects					Threshold Model Parameters		
		Predictors	Estimate	CI	P	DF	Positive Threshold	Negative Threshold	Slope Ratio
Benchmarking Study	NREM to REM	Δ alpha	0.86	(-0.05, 1.77)	0.073	52	0.725	-1.5	0.5
		Δ beta	1.01	(0.18, 1.85)	0.023	52	0.35	-1.5	0.5
		Δ delta	-0.31	(-0.96, 0.34)	0.359	52	1.5	-1.15	2
		Δ HR	0.10	(-0.27, 0.47)	0.593	37	1.5	0	2
		Δ theta	0.28	(-0.37, 0.93)	0.405	52	0	-1.5	0.5
	REM to NREM	Δ alpha	-0.17	(-0.46, 0.13)	0.276	45	1.5	0	2
		Δ beta	-0.08	(-0.29, 0.13)	0.445	45	0.2	-1.5	1.9
		Δ delta	-0.43	(-0.74, -0.11)	0.011	45	1	-0.9	2
		Δ HR	0.32	(-0.13, 0.78)	0.180	34	1.5	-0.625	2
		Δ theta	-0.03	(-0.17, 0.1)	0.628	45	0	0	2
	Sleep to Wake	Δ alpha	-0.89	(-1.71, -0.08)	0.038	53	0.775	-1.5	0.5
		Δ beta	0.67	(-0.14, 1.47)	0.114	53	0.35	-1.5	0.5
		Δ delta	0.03	(-0.17, 0.23)	0.778	53	0.025	-1.45	2
		Δ HR	-0.32	(-1.01, 0.38)	0.383	39	0	-1.4	0.5
		Δ theta	0.04	(-0.2, 0.29)	0.737	53	0.25	-1.5	1.75
	Wake to Sleep	Δ alpha	-0.31	(-0.98, 0.37)	0.377	89	1.5	-0.975	0.525
Δ beta		0.45	(-0.07, 0.96)	0.095	89	1.5	-1.25	2	
Δ delta		-0.22	(-0.6, 0.17)	0.273	89	0.2	-1.5	0.9	
Δ HR		-0.11	(-0.25, 0.03)	0.145	64	0	0	2	
Δ theta		-0.20	(-0.68, 0.27)	0.409	89	0.05	-1.3	0.5	
Replication Study	REM to NREM	Δ alpha	0.26	(-0.46, 0.97)	0.493	8	1.5	-0.1	2
		Δ beta	-0.75	(-2.45, 0.94)	0.400	8	0.175	-1.325	0.5
		Δ delta	2.23	(-0.7, 5.16)	0.167	8	1.15	-1.475	1.8
		Δ HR	-0.75	(-2.21, 0.71)	0.342	7	0.825	-0.675	0.5
		Δ theta	0.11	(-0.73, 0.95)	0.803	8	1.5	-0.675	1.9
	REM to NREM	Δ alpha	-2.79	(-5.55, -0.04)	0.073	12	1.5	-1.5	0.5
		Δ beta	0.05	(-0.4, 0.51)	0.825	12	0.4	-0.625	2
		Δ delta	-2.05	(-4.21, 0.12)	0.092	12	1.05	-1.5	0.5
		Δ HR	-0.73	(-6.16, 4.7)	0.782	3	0.9	-0.975	0.5
	Wake to Sleep	Δ theta	-2.04	(-2.97, -1.11)	0.001	12	0.05	-1.5	0.5
		Δ alpha	0.23	(-0.5, 0.96)	0.557	17	1.5	-0.225	2
		Δ beta	1.65	(0.54, 2.76)	0.011	17	0.1	-1.5	0.5
		Δ delta	2.55	(-3.56, 8.66)	0.436	17	1.425	-1.5	0.5
	Δ HR	0.36	(-0.2, 0.91)	0.236	17	1.5	-0.025	2	
	Δ theta	0.03	(-0.66, 0.73)	0.931	17	1.5	0	2	

1522 Rapid eye movement, REM; non-REM, NREM; Confidence Interval, CI; Degrees of Freedom,
 1523 DF; EEG band power predictor units in percent of total band power; HR predictor units beats-
 1524 per-minute. **Bolded P values reflect significant associations at P < 0.05.** Predictor and
 1525 parenchymal resistance values in regression models were scaled to zero mean and unit
 1526 standard deviation with coefficient estimates representing effect size in standard deviations.
 1527 Positive and negative thresholds are in units of predictor standard deviation.

1528 **Supplemental Table 6. Comparison of investigational device and polysomnography hypnogram staging to manual scoring.**

1529

Manual Scoring	Device										
	W	REM	N1	N2	N3		sensitivity	specificity	precision	accuracy	f1
W	2653	56	256	156	6		0.828	0.959	0.843	0.932	0.835
REM	121	1334	130	127	2		0.801	0.972	0.776	0.954	0.788
N1	162	44	583	250	0		0.367	0.967	0.558	0.905	0.443
N2	224	224	611	4490	20		0.774	0.886	0.804	0.844	0.789
N3	7	5	2	753	877		0.969	0.945	0.525	0.947	0.681
	PSG C3										
	W	REM	N1	N2	N3		sensitivity	specificity	precision	accuracy	f1
W	2922	56	68	79	2		0.892	0.981	0.928	0.962	0.910
REM	40	1563	37	74	0		0.893	0.989	0.910	0.978	0.901
N1	178	54	467	339	1		0.707	0.961	0.447	0.950	0.547
N2	94	76	85	5188	126		0.870	0.958	0.929	0.924	0.899
N3	4	0	1	262	1377		0.914	0.979	0.825	0.973	0.867
	PSG C4										
	W	REM	N1	N2	N3		sensitivity	specificity	precision	accuracy	f1
W	3035	22	31	39	0		0.974	0.991	0.964	0.987	0.969
REM	3	1665	21	25	0		0.965	0.996	0.969	0.993	0.967
N1	27	20	659	333	0		0.885	0.974	0.631	0.969	0.736
N2	10	12	32	5493	22		0.913	0.990	0.984	0.960	0.947
N3	0	5	0	104	1535		0.985	0.990	0.920	0.990	0.951

1530 Polysomnography, PSG; Wake, W; Rapid eye movement, REM

1531 **Supplemental Table 7: Electrode characterization according to ANSI/AAMI EC12*.**

1532


Electrode Pair #	AC Impedance at 10 Hz [Ω]	DC Offset Voltage [mV]	Combined Offset Instability and Internal Noise [μ V]		Bias Current Tolerance [mV]
			EC12 (0.15-100 Hz)	EEG (0.3-50 Hz)	
1	609	0.5	22.9	9.7	11.2
2	759	0.3	126.4	28.2	10.7
3	1023	3.8	13.3	7.9	10.8
4	1035	1.4	19.6	8.0	7.0
5	583	1.4	7.1	1.9	9.5
6	424	1.1	8.1	3.8	9.3

1533 Alternating Current, AC; Direct Current, DC; EC12, ANSI/AAMI EC12:2000/(R)2020.

1534 *ANSI/AAMI EC12 reference values are as follows: AC impedance under 3000 Ω in any pair, under 2000 Ω on average; DC offset
1535 under 100 mV; offset instability and internal noise under 150 μ V; tolerance to bias under 100 mV.
1536
1537

1538 Supplemental Table 8. Benchtop tests for assessing calibration and sensitivity to electrode impedance.
 1539

		Electrode Configuration				Load	Measured Load Components
		Left		Right		[Ω]	
		Setting	MASTOID	IN-EAR	IN-EAR		
	Cal R 20	Low	Low	Low	Low	20	20.0
	Cal R 40	Low	Low	Low	Low	40.2	40.2
	Cal R 60	Low	Low	Low	Low	60.4	60.3
	Cal R 80	Low	Low	Low	Low	80.6	80.5
	Cal R 100	Low	Low	Low	Low	100	100.4
Calibration 2R1C	Cal 2R1C 20	Low	Low	Low	Low	20 (470 + 22n)	Rs = 20, Rp=468.2, Cp = 23.3n
	Cal 2R1C 40	Low	Low	Low	Low	40.2 (470 + 22n)	Rs = 40.2, Rp=468.2, Cp = 23.3n
	Cal 2R1C 60	Low	Low	Low	Low	60.4 (470 + 22n)	Rs = 60.3, Rp=468.2, Cp = 23.3n
	Cal 2R1C 80	Low	Low	Low	Low	80.6 (470 + 22n)	Rs = 80.5, Rp=468.2, Cp = 23.3n
	Cal 2R1C 100	Low	Low	Low	Low	100 (470 + 22n)	Rs = 100.4, Rp=468.2, Cp = 23.3n
Sensitivity to Electrode Impedance	Low All	Low	Low	Low	Low	50 (470 + 22n)	Rs = 49.9, Rp=468.2, Cp = 23.3n
	High Right Mastoid	Low	Low	Low	High	50 (470 + 22n)	Rs = 49.9, Rp=468.2, Cp = 23.3n
	High Right	Low	Low	High	High	50 (470 + 22n)	Rs = 49.9, Rp=468.2, Cp = 23.3n
	High Right In-Ear	Low	Low	High	Low	50 (470 + 22n)	Rs = 49.9, Rp=468.2, Cp = 23.3n
	High In-Ear	Low	High	High	Low	50 (470 + 22n)	Rs = 49.9, Rp=468.2, Cp = 23.3n
	High Left In-Ear	Low	High	Low	Low	50 (470 + 22n)	Rs = 49.9, Rp=468.2, Cp = 23.3n
	High Left	High	High	Low	Low	50 (470 + 22n)	Rs = 49.9, Rp=468.2, Cp = 23.3n
	High Left Mastoid	High	Low	Low	Low	50 (470 + 22n)	Rs = 49.9, Rp=468.2, Cp = 23.3n
	High Mastoids	High	Low	Low	High	50 (470 + 22n)	Rs = 49.9, Rp=468.2, Cp = 23.3n
	High All	High	High	High	High	50 (470 + 22n)	Rs = 49.9, Rp=468.2, Cp = 23.3n

 Element to change from one benchtop test to the next

1541 **Supplemental Table 9. Absolute error of resistance for benchtop tests (values in ohms).**

	Setting	1kHz	1.6kHz	2.28kHz	3.2kHz	4.55kHz	6.4kHz	8.53kHz	12.8kHz	16kHz	25.6kHz	32kHz	51.2kHz	64kHz	85.3kHz	102kHz	128kHz
Calibration R	Cal R 20	0.125	0.151	0.157	0.119	0.127	0.154	0.182	0.190	0.220	0.308	0.320	0.274	0.094	0.379	0.700	0.702
	Cal R 40	0.220	0.161	0.152	0.192	0.221	0.094	0.164	0.117	0.127	0.151	0.200	0.301	0.134	0.438	0.344	0.396
	Cal R 60	0.333	0.231	0.325	0.307	0.301	0.413	0.411	0.208	0.308	0.326	0.276	0.456	0.327	0.412	0.268	0.301
	Cal R 80	0.104	0.175	0.242	0.205	0.314	0.140	0.154	0.257	0.258	0.332	0.333	0.257	0.284	0.298	0.317	0.230
	Cal R 100	0.301	0.288	0.268	0.251	0.261	0.323	0.236	0.271	0.458	0.380	0.199	0.157	0.387	0.324	0.196	0.134
Calibration 2R1C	Cal 2R1C 20	0.232	0.277	0.244	0.105	0.130	0.125	0.141	0.087	0.211	0.247	0.383	0.355	0.228	0.371	0.522	0.756
	Cal 2R1C 40	0.191	0.117	0.112	0.305	0.207	0.042	0.207	0.149	0.268	0.157	0.134	0.240	0.314	0.242	0.421	0.311
	Cal 2R1C 60	0.372	0.213	0.356	0.292	0.202	0.209	0.263	0.276	0.333	0.475	0.260	0.301	0.522	0.434	0.380	0.318
	Cal 2R1C 80	0.215	0.166	0.249	0.175	0.186	0.252	0.231	0.168	0.348	0.384	0.303	0.211	0.333	0.331	0.280	0.143
	Cal 2R1C 100	0.384	0.304	0.256	0.295	0.195	0.159	0.294	0.283	0.428	0.423	0.339	0.379	0.208	0.172	0.193	0.021
Sensitivity to Electrode Impedance	Low All	0.284	0.159	0.181	0.318	0.227	0.171	0.280	0.263	0.136	0.152	0.165	0.279	0.237	0.192	0.454	0.330
	High Right Mastoid	0.123	0.003	0.165	0.220	0.176	0.210	0.071	0.120	0.128	0.085	0.001	0.300	0.242	0.650	0.362	0.725
	High Right	0.131	0.242	0.079	0.279	0.232	0.253	0.274	0.144	0.202	0.186	0.167	-0.022	0.383	0.586	0.620	0.911
	High Right In-Ear	0.259	0.256	0.249	0.297	0.252	0.347	0.183	0.182	0.279	0.256	0.212	0.315	0.139	0.529	0.457	0.576
	High In-Ear	0.384	0.263	0.109	0.233	0.350	0.236	0.237	0.292	0.266	0.259	0.312	0.327	0.379	0.415	0.446	0.450
	High Left In-Ear	0.210	0.169	0.236	0.313	0.262	0.319	0.229	0.269	0.280	0.332	0.324	0.168	0.303	0.255	0.361	0.310
	High Left	0.266	0.337	0.372	0.241	0.271	0.281	0.252	0.167	0.388	0.501	0.416	0.266	0.128	0.225	0.218	0.006
	High Left Mastoid	0.341	0.325	0.217	0.225	0.222	0.193	0.185	0.242	0.430	0.363	0.269	0.242	0.143	0.097	0.268	0.018
	High Mastoids	0.307	0.227	0.235	0.364	0.286	0.192	0.348	0.363	0.339	0.277	0.238	0.146	0.498	0.455	0.492	0.487
High All	0.517	0.412	0.447	0.374	0.418	0.420	0.342	0.397	0.425	0.461	0.375	0.418	0.527	0.727	0.852	0.843	

1542

1543

1544
1545

Supplemental Table 10. Absolute error of reactance for benchtop tests (values in ohms).

	Setting	1kHz	1.6kHz	2.28kHz	3.2kHz	4.55kHz	6.4kHz	8.53kHz	12.8kHz	16kHz	25.6kHz	32kHz	51.2kHz	64kHz	85.3kHz	102kHz	128kHz
Calibration R	Cal R 20	0.087	-0.031	0.055	-0.046	0.010	-0.016	0.104	-0.030	0.142	0.237	0.172	0.188	0.018	0.250	0.197	0.288
	Cal R 40	0.032	0.042	0.011	0.055	-0.054	-0.057	0.126	0.035	0.018	-0.027	0.027	0.087	-0.070	0.057	0.102	0.040
	Cal R 60	0.103	0.007	-0.025	0.070	-0.052	-0.017	0.025	0.044	0.069	-0.071	0.090	-0.041	-0.032	-0.129	-0.050	-0.107
	Cal R 80	0.036	0.073	0.015	-0.132	-0.042	0.064	0.012	-0.010	0.047	0.072	0.040	-0.010	-0.061	-0.092	-0.162	-0.181
	Cal R 100	-0.066	-0.054	0.028	-0.019	0.011	0.153	0.057	-0.051	-0.002	0.022	0.045	-0.003	-0.133	-0.024	-0.050	-0.121
Calibration 2R1C	Cal 2R1C 20	0.044	-0.039	-0.037	0.019	0.043	0.033	0.031	0.051	0.091	0.143	0.210	0.211	0.237	0.285	0.413	0.380
	Cal 2R1C 40	0.001	-0.070	-0.029	0.084	-0.049	0.030	-0.050	-0.033	0.026	0.000	-0.008	0.020	0.117	0.074	0.097	0.114
	Cal 2R1C 60	0.019	0.006	-0.043	-0.017	0.009	0.032	0.120	-0.120	-0.005	0.034	-0.149	0.089	0.106	0.041	0.204	0.122
	Cal 2R1C 80	0.095	-0.005	0.018	0.145	-0.018	-0.073	0.001	0.017	0.013	0.010	0.145	0.058	0.076	-0.012	-0.028	0.104
	Cal 2R1C 100	-0.030	-0.118	-0.014	0.065	-0.066	0.025	0.070	0.055	0.074	0.037	0.174	0.158	0.012	0.092	0.041	0.105
Sensitivity to Electrode Impedance	Low All	0.015	-0.066	0.047	-0.052	0.046	0.016	0.068	-0.040	-0.032	-0.112	0.006	0.107	0.121	0.006	0.093	0.112
	High Right Mastoid	0.113	0.084	0.030	0.095	0.131	-0.034	0.043	0.043	0.103	0.139	0.160	0.251	0.309	0.388	0.389	0.306
	High Right	0.029	0.059	-0.024	0.159	0.000	0.098	0.028	0.016	0.059	0.124	0.186	0.136	0.243	0.204	0.459	0.335
	High Right In-Ear	0.015	-0.074	-0.001	-0.019	0.073	0.044	0.076	0.042	0.011	0.073	0.047	0.131	0.123	-0.009	0.150	0.133
	High In-Ear	0.071	-0.015	0.000	-0.074	0.026	-0.104	-0.007	0.028	0.087	0.045	0.021	0.103	0.203	0.111	0.043	0.160
	High Left In-Ear	-0.007	0.001	0.015	0.013	-0.042	-0.168	0.045	0.010	-0.049	0.006	-0.032	0.038	0.237	0.150	0.070	0.137
	High Left	-0.150	-0.117	-0.154	-0.178	0.012	-0.104	-0.025	-0.124	-0.172	-0.159	-0.127	-0.253	-0.173	-0.147	-0.124	-0.099
	High Left Mastoid	-0.173	-0.093	-0.169	-0.045	-0.104	-0.073	0.001	-0.104	-0.032	-0.211	-0.271	-0.187	-0.212	-0.076	-0.251	-0.091
	High Mastoids	0.034	-0.002	0.036	-0.023	-0.100	-0.010	-0.054	0.032	-0.042	-0.103	0.008	-0.006	0.083	0.082	0.176	0.058
	High All	-0.041	-0.114	-0.083	-0.109	-0.091	-0.066	-0.051	0.065	0.083	0.103	0.013	0.138	0.278	0.296	0.389	0.401

1546
1547
1548

1549
 1550
 1551

Supplemental Table 11. Debye model absolute prediction error (ohms) of dispersion relative to 128kHz.

	Setting	1kHz	1.6kHz	2.28kHz	3.2kHz	4.55kHz	6.4kHz	8.53kHz	12.8kHz	16kHz	25.6kHz	32kHz	51.2kHz	64kHz	85.3kHz	102kHz
Sensitivity to Electrode Impedance	Low All	-0.037	-0.040	-0.044	-0.051	-0.063	-0.080	-0.093	-0.098	-0.091	-0.058	-0.042	-0.017	-0.010	-0.004	-0.002
	High Right Mastoid	-0.243	-0.250	-0.260	-0.278	-0.309	-0.345	-0.368	-0.352	-0.311	-0.187	-0.133	-0.054	-0.032	-0.014	-0.006
	High Right	-0.247	-0.252	-0.261	-0.277	-0.302	-0.332	-0.350	-0.331	-0.291	-0.175	-0.124	-0.050	-0.030	-0.013	-0.006
	High Right In-Ear	-0.109	-0.113	-0.120	-0.132	-0.152	-0.178	-0.197	-0.197	-0.177	-0.110	-0.079	-0.032	-0.019	-0.008	-0.004
	High In-Ear	-0.128	-0.130	-0.134	-0.140	-0.150	-0.162	-0.168	-0.158	-0.139	-0.084	-0.060	-0.024	-0.015	-0.006	-0.003
	High Left In-Ear	-0.055	-0.053	-0.051	-0.046	-0.039	-0.027	-0.015	0.000	0.005	0.007	0.006	0.003	0.002	0.001	0.000
	High Left	0.065	0.069	0.074	0.082	0.098	0.119	0.136	0.144	0.133	0.087	0.063	0.026	0.016	0.007	0.003
	High Left Mastoid	0.067	0.070	0.075	0.084	0.099	0.118	0.135	0.142	0.131	0.085	0.062	0.026	0.015	0.007	0.003
	High Mastoids	-0.119	-0.120	-0.121	-0.124	-0.127	-0.131	-0.130	-0.116	-0.100	-0.059	-0.042	-0.017	-0.010	-0.004	-0.002
	High All	-0.202	-0.209	-0.221	-0.240	-0.271	-0.311	-0.338	-0.329	-0.293	-0.178	-0.127	-0.052	-0.031	-0.013	-0.006
RMSE		0.147	0.151	0.157	0.168	0.186	0.209	0.224	0.216	0.193	0.117	0.084	0.034	0.020	0.009	0.004
Load Value		4.766	4.724	4.654	4.526	4.282	3.877	3.374	2.461	1.931	0.995	0.685	0.286	0.183	0.099	0.066
Error %		3.1%	3.2%	3.4%	3.7%	4.3%	5.4%	6.6%	8.8%	10.0%	11.8%	12.2%	12.0%	11.1%	8.8%	6.1%

1552

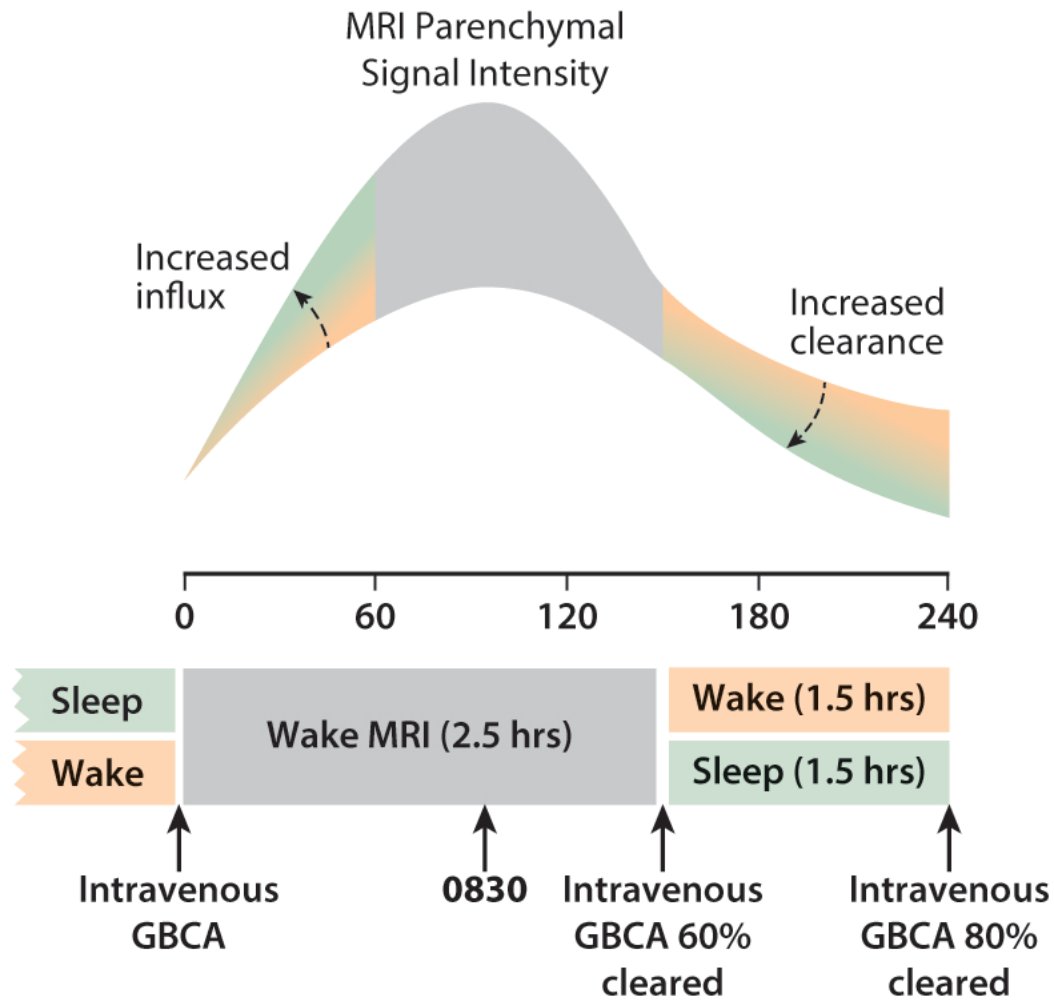
1553 **Supplemental Table 12: Minimum significant change in mean R_p and correlation with a**
1554 **predictor using the R_p standard deviation of the electrode impedance sensitivity tests.**
1555

Number of Samples	25	100
Standard Deviation [Ω]	0.113	0.113
Standard Error [Ω]	0.023	0.011
Minimum Significant Change [Ω]	0.044	0.022
Minimum Significant Correlation	0.39	0.20

1556 Brain parenchymal resistance, R_p .

1557

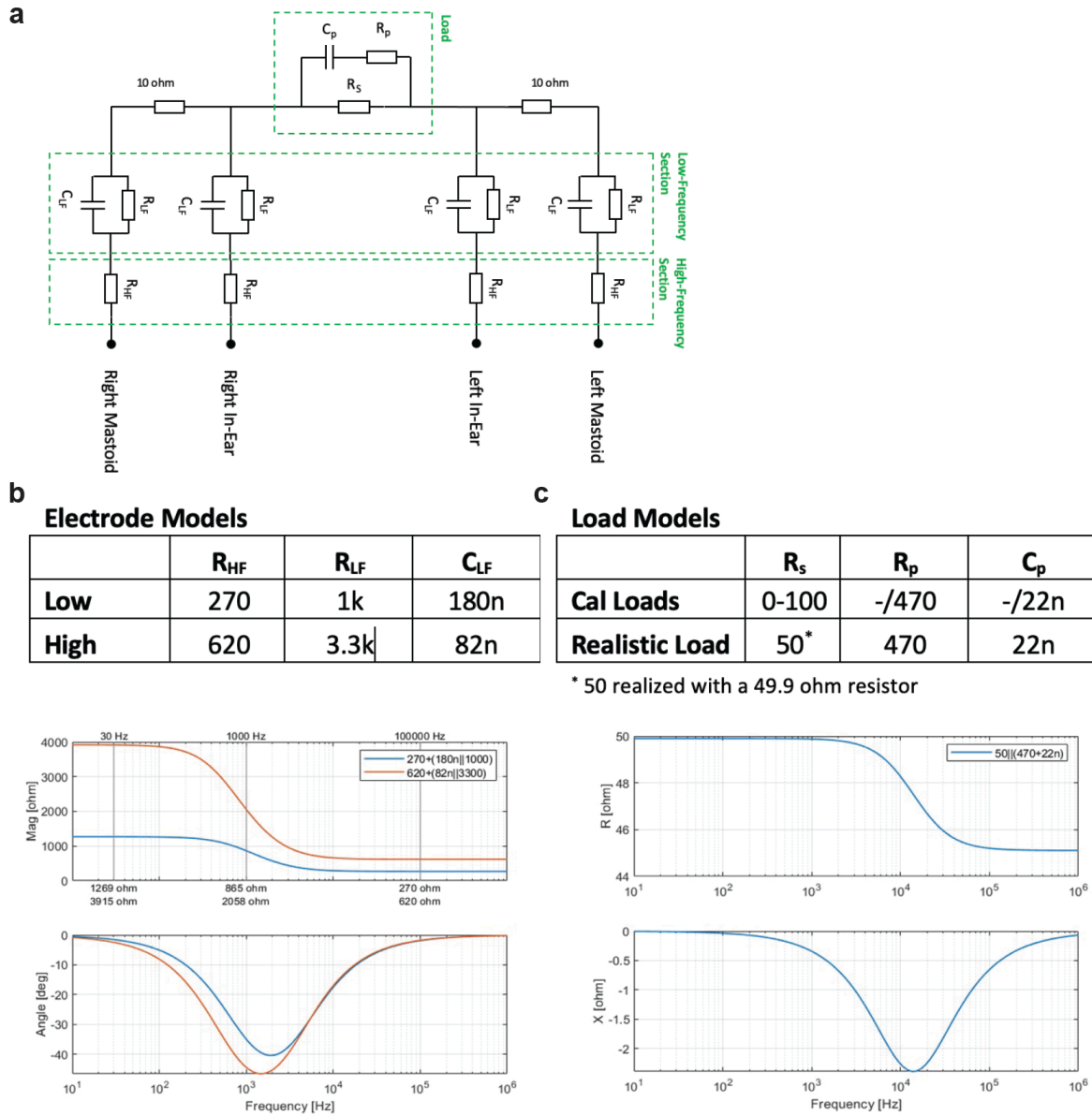
1558



1560
1561

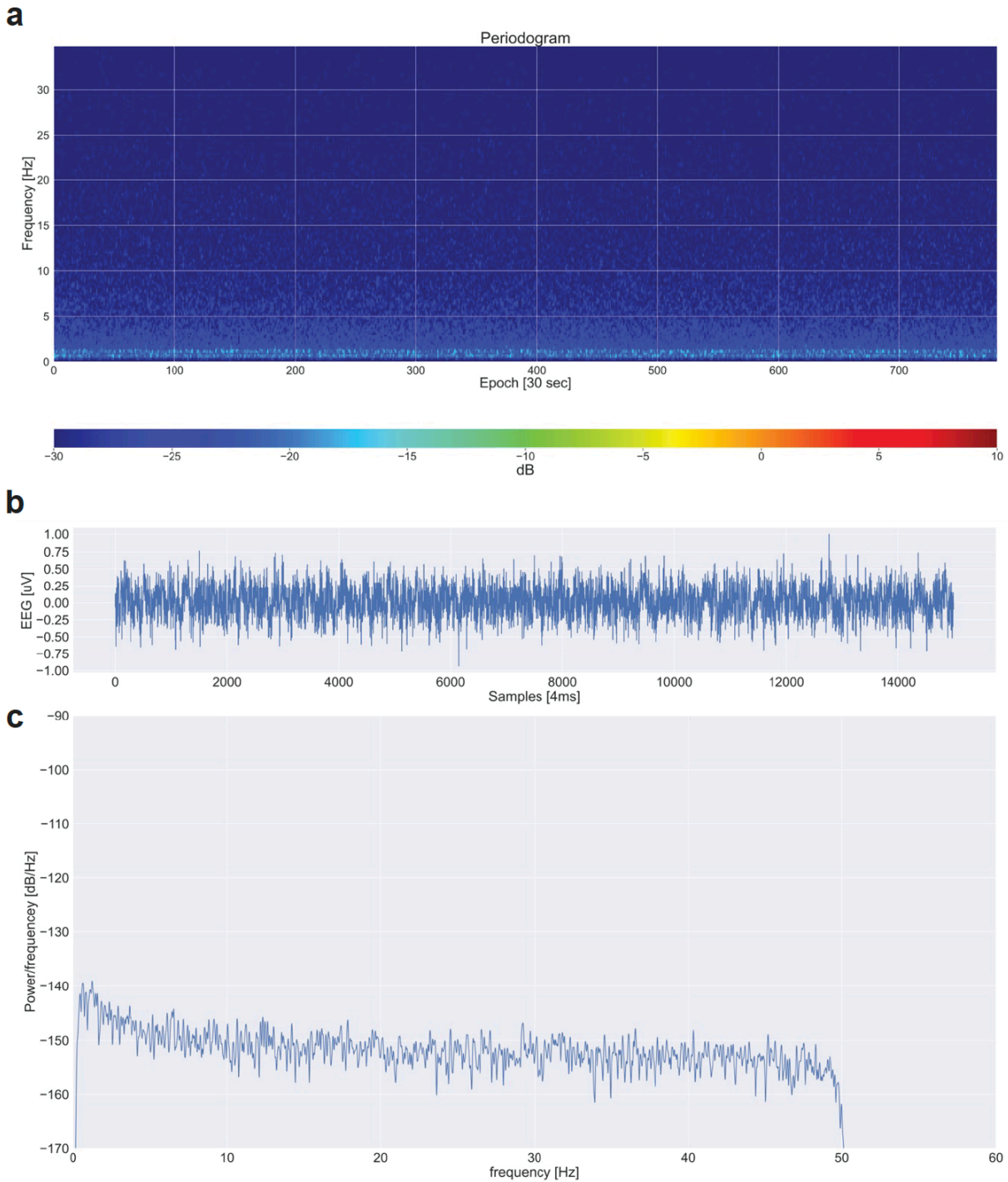
1562 **Supplemental Figure 1.** An illustration of the effect of increased CSF influx into the brain
1563 parenchyma and clearance from the parenchyma on contrast-enhanced MRI signal intensity in
1564 the Benchmarking study. An increase in CSF influx into the brain parenchyma following
1565 intravenous GBCA leads to greater contrast delivery to the brain parenchyma and a
1566 corresponding increase in MRI signal intensity. MRI signal intensity of the brain parenchyma
1567 has been shown to peak at approximately 90 minutes post-injection¹⁵ which occurred at time
1568 0830 in the Benchmarking study. With a terminal half-life of 109 minutes²⁸, intravenous contrast
1569 is 60% cleared at 140 minutes post-injection when the morning sleep/wake intervention begins
1570 and is 80% cleared at the end of the morning intervention when the second post-contrast MRI
1571 scan is acquired. During this morning intervention, an increase in CSF clearance from the brain
1572 parenchyma leads to a corresponding decrease in MRI signal intensity.

1573 **Supplemental Figure 2.**



1574
 1575 **Supplemental Figure 2. a**, Circuit model of transcranial measurements using four-point
 1576 electrical impedance spectroscopy and models for each of the four electrode contact
 1577 impedances. **b**, Electrode impedance models comprised a low impedance and a high
 1578 impedance model, representing the range of in-human impedances. **c**, Calibration loads varied
 1579 the resistance R_S of the free fluid or interstitial fluid compartment from 20 to 100 Ω in increments
 1580 of 20 Ω , with and additional $R_P C_P$ in parallel to simulate complex loads. The realistic load
 1581 parameters were chosen to create a frequency dispersion that approximated the in-human
 1582 measured dispersions. **d**, Electrode impedance dispersion over the measured frequencies for
 1583 the low and high impedance model. **e**, Load impedance dispersion over the measured
 1584 frequencies using the Real Load model.
 1585

1586 **Supplemental Figure 3.**



1587
1588
1589
1590
1591
1592
1593
1594

Supplemental Figure 3. **a**, Periodogram of a device over a 12 hour test using four Ag/AgCl sintered disk electrodes on an Agar phantom with EEG gel. For reference, human EEG beta power during NREM sleep is above -10dB on the device. **b**, EEG recording over an epoch shows 0.5 μ V peak-to-peak noise. **c**, Power spectral density shows a noise floor at -150dB/Hz with a 1/f increase to -140db/Hz below 10Hz.

1595 **REFERENCES**

- 1596 1 Iliff, J. J. *et al.* A paravascular pathway facilitates CSF flow through the brain
1597 parenchyma and the clearance of interstitial solutes, including amyloid β . *Sci Transl Med*
1598 **4**, 147ra111 (2012). <https://doi.org/10.1126/scitranslmed.3003748>
- 1599 2 Xie, L. *et al.* Sleep drives metabolite clearance from the adult brain. *Science* **342**, 373-
1600 377 (2013). <https://doi.org/10.1126/science.1241224>
- 1601 3 Iliff, J. J. *et al.* Impairment of glymphatic pathway function promotes tau pathology after
1602 traumatic brain injury. *J Neurosci* **34**, 16180-16193 (2014).
1603 <https://doi.org/10.1523/JNEUROSCI.3020-14.2014>
- 1604 4 Harrison, I. F. *et al.* Impaired glymphatic function and clearance of tau in an Alzheimer's
1605 disease model. *Brain* **143**, 2576-2593 (2020). <https://doi.org/10.1093/brain/awaa179>
- 1606 5 Ishida, K. *et al.* Glymphatic system clears extracellular tau and protects from tau
1607 aggregation and neurodegeneration. *J Exp Med* **219** (2022).
1608 <https://doi.org/10.1084/jem.20211275>
- 1609 6 Cui, H. *et al.* Decreased AQP4 Expression Aggravates α -Synuclein Pathology in
1610 Parkinson's Disease Mice, Possibly via Impaired Glymphatic Clearance. *J Mol Neurosci*
1611 **71**, 2500-2513 (2021). <https://doi.org/10.1007/s12031-021-01836-4>
- 1612 7 Zou, W. *et al.* Blocking meningeal lymphatic drainage aggravates Parkinson's disease-
1613 like pathology in mice overexpressing mutated α -synuclein. *Transl Neurodegener* **8**, 7
1614 (2019). <https://doi.org/10.1186/s40035-019-0147-y>
- 1615 8 Hablitz, L. M. & Nedergaard, M. The Glymphatic System: A Novel Component of
1616 Fundamental Neurobiology. *J Neurosci* **41**, 7698-7711 (2021).
1617 <https://doi.org/10.1523/JNEUROSCI.0619-21.2021>
- 1618 9 Klostranec, J. M. *et al.* Current Concepts in Intracranial Interstitial Fluid Transport and
1619 the Glymphatic System: Part II-Imaging Techniques and Clinical Applications.
1620 *Radiology* **301**, 516-532 (2021). <https://doi.org/10.1148/radiol.2021204088>
- 1621 10 Hablitz, L. M. *et al.* Circadian control of brain glymphatic and lymphatic fluid flow. *Nat*
1622 *Commun* **11**, 4411 (2020). <https://doi.org/10.1038/s41467-020-18115-2>
- 1623 11 Hablitz, L. M. *et al.* Increased glymphatic influx is correlated with high EEG delta power
1624 and low heart rate in mice under anesthesia. *Sci Adv* **5**, eaav5447 (2019).
1625 <https://doi.org/10.1126/sciadv.aav5447>
- 1626 12 Eide, P. K., Vinje, V., Pripp, A. H., Mardal, K. A. & Ringstad, G. Sleep deprivation
1627 impairs molecular clearance from the human brain. *Brain* **144**, 863-874 (2021).
1628 <https://doi.org/10.1093/brain/awaa443>
- 1629 13 Ringstad, G. *et al.* Brain-wide glymphatic enhancement and clearance in humans
1630 assessed with MRI. *JCI Insight* **3** (2018). <https://doi.org/10.1172/jci.insight.121537>
- 1631 14 Deike-Hofmann, K. *et al.* Glymphatic Pathway of Gadolinium-Based Contrast Agents
1632 Through the Brain: Overlooked and Misinterpreted. *Invest Radiol* **54**, 229-237 (2019).
1633 <https://doi.org/10.1097/RLI.0000000000000533>
- 1634 15 Richmond, S. B. *et al.* Quantification approaches for magnetic resonance imaging
1635 following intravenous gadolinium injection: A window into brain-wide glymphatic
1636 function. *Eur J Neurosci* **57**, 1689-1704 (2023). <https://doi.org/10.1111/ejn.15974>
- 1637 16 Bera, T. K. Bioelectrical Impedance Methods for Noninvasive Health Monitoring: A
1638 Review. *J Med Eng* **2014**, 381251 (2014). <https://doi.org/10.1155/2014/381251>
- 1639 17 Abasi, S., Aggas, J. R., Garayar-Leyva, G. G., Walther, B. K. & Guiseppi-Elie, A.
1640 Bioelectrical Impedance Spectroscopy for Monitoring Mammalian Cells and Tissues

- 1641 under Different Frequency Domains: A Review. *ACS Meas Sci Au* **2**, 495-516 (2022).
1642 <https://doi.org/10.1021/acsmesuresciau.2c00033>
- 1643 18 Stupin, D. D. *et al.* Bioimpedance Spectroscopy: Basics and Applications. *ACS Biomater*
1644 *Sci Eng* **7**, 1962-1986 (2021). <https://doi.org/10.1021/acsbiomaterials.0c01570>
- 1645 19 Gabriel, S., Lau, R. W. & Gabriel, C. The dielectric properties of biological tissues: II.
1646 Measurements in the frequency range 10 Hz to 20 GHz. *Phys Med Biol* **41**, 2251-2269
1647 (1996). <https://doi.org/10.1088/0031-9155/41/11/002>
- 1648 20 Gabriel, C. Dielectric properties of biological tissue: variation with age.
1649 *Bioelectromagnetics Suppl* **7**, S12-18 (2005). <https://doi.org/10.1002/bem.20147>
- 1650 21 Jessen, N. A., Munk, A. S., Lundgaard, I. & Nedergaard, M. The Glymphatic System: A
1651 Beginner's Guide. *Neurochem Res* **40**, 2583-2599 (2015). [https://doi.org/10.1007/s11064-](https://doi.org/10.1007/s11064-015-1581-6)
1652 [015-1581-6](https://doi.org/10.1007/s11064-015-1581-6)
- 1653 22 Nakamura, K. *et al.* Diurnal fluctuations in brain volume: Statistical analyses of MRI
1654 from large populations. *Neuroimage* **118**, 126-132 (2015).
1655 <https://doi.org/10.1016/j.neuroimage.2015.05.077>
- 1656 23 Elvsåshagen, T. *et al.* Cerebral blood flow changes after a day of wake, sleep, and sleep
1657 deprivation. *Neuroimage* **186**, 497-509 (2019).
1658 <https://doi.org/10.1016/j.neuroimage.2018.11.032>
- 1659 24 Dagum, P. Non-invasive assessment of glymphatic flow and neurodegeneration from a
1660 wearable device. (2022).
- 1661 25 Dagum, P. Non-invasive assessment of glymphatic flow and neurodegeneration from a
1662 wearable device. (2022).
- 1663 26 Nasreddine, Z. S. *et al.* The Montreal Cognitive Assessment, MoCA: a brief screening
1664 tool for mild cognitive impairment. *J Am Geriatr Soc* **53**, 695-699 (2005).
1665 <https://doi.org/10.1111/j.1532-5415.2005.53221.x>
- 1666 27 Brown, L. M. & Schinka, J. A. Development and initial validation of a 15-item informant
1667 version of the Geriatric Depression Scale. *Int J Geriatr Psychiatry* **20**, 911-918 (2005).
1668 <https://doi.org/10.1002/gps.1375>
- 1669 28 Administration., U. F. a. D. *Gadavist (gadobutrol) injection, for intravenous use,*
1670 https://www.accessdata.fda.gov/drugsatfda_docs/label/2011/201277s000lbl.pdf
1671 (2011).
- 1672 29 Heinze, G., Wallisch, C. & Dunkler, D. Variable selection - A review and
1673 recommendations for the practicing statistician. *Biom J* **60**, 431-449 (2018).
1674 <https://doi.org/10.1002/bimj.201700067>
- 1675 30 Iliff, J. J. *et al.* Brain-wide pathway for waste clearance captured by contrast-enhanced
1676 MRI. *J Clin Invest* **123**, 1299-1309 (2013). <https://doi.org/10.1172/JCI67677>
- 1677 31 Boukamp, B. A. A Linear Kronig-Kramers Transform Test for Immittance Data
1678 Validation. *Journal of The Electrochemical Society* **142**, 1885 (1995).
- 1679 32 Schonleber, M., Klotz, D. & Ivers-Tiffée, E. A Method for Improving the Robustness of
1680 linear Kramers-Kronig Validity Tests. *Electrochimica Acta* **131**, 20-27 (2014).
- 1681 33 Song, J. *et al.* Electrical Impedance Changes at Different Phases of Cerebral Edema in
1682 Rats with Ischemic Brain Injury. *Biomed Res Int* **2018**, 9765174 (2018).
1683 <https://doi.org/10.1155/2018/9765174>
- 1684 34 Abboud, T., Mielke, D. & Rohde, V. Mini Review: Impedance Measurement in
1685 Neuroscience and Its Prospective Application in the Field of Surgical Neurooncology.
1686 *Front Neurol* **12**, 825012 (2021). <https://doi.org/10.3389/fneur.2021.825012>

- 1687 35 Witkowska-Wrobel, A., Aristovich, K., Crawford, A., Perkins, J. D. & Holder, D.
1688 Imaging of focal seizures with Electrical Impedance Tomography and depth electrodes in
1689 real time. *Neuroimage* **234**, 117972 (2021).
1690 <https://doi.org/10.1016/j.neuroimage.2021.117972>
- 1691 36 Romsauerova, A. *et al.* Multi-frequency electrical impedance tomography (EIT) of the
1692 adult human head: initial findings in brain tumours, arteriovenous malformations and
1693 chronic stroke, development of an analysis method and calibration. *Physiol Meas* **27**,
1694 S147-161 (2006). <https://doi.org/10.1088/0967-3334/27/5/S13>
- 1695 37 Iliff, J. J. *et al.* Cerebral arterial pulsation drives paravascular CSF-interstitial fluid
1696 exchange in the murine brain. *J Neurosci* **33**, 18190-18199 (2013).
1697 <https://doi.org/10.1523/JNEUROSCI.1592-13.2013>
- 1698 38 Ringstad, G., Vatnehol, S. A. S. & Eide, P. K. Glymphatic MRI in idiopathic normal
1699 pressure hydrocephalus. *Brain* **140**, 2691-2705 (2017).
1700 <https://doi.org/10.1093/brain/awx191>
- 1701 39 Mestre, H. *et al.* Aquaporin-4-dependent glymphatic solute transport in the rodent brain.
1702 *Elife* **7** (2018). <https://doi.org/10.7554/eLife.40070>
- 1703 40 Mestre, H. *et al.* Flow of cerebrospinal fluid is driven by arterial pulsations and is
1704 reduced in hypertension. *Nat Commun* **9**, 4878 (2018). <https://doi.org/10.1038/s41467-018-07318-3>
- 1705
- 1706 41 Jiang-Xie, L. F. *et al.* Neuronal dynamics direct cerebrospinal fluid perfusion and brain
1707 clearance. *Nature* **627**, 157-164 (2024). <https://doi.org/10.1038/s41586-024-07108-6>
- 1708 42 Piantino, J., Lim, M. M., Newgard, C. D. & Iliff, J. Linking Traumatic Brain Injury,
1709 Sleep Disruption and Post-Traumatic Headache: a Potential Role for Glymphatic
1710 Pathway Dysfunction. *Curr Pain Headache Rep* **23**, 62 (2019).
1711 <https://doi.org/10.1007/s11916-019-0799-4>
- 1712 43 Nedergaard, M. & Goldman, S. A. Glymphatic failure as a final common pathway to
1713 dementia. *Science* **370**, 50-56 (2020). <https://doi.org/10.1126/science.abb8739>
- 1714 44 Goldman, N., Hablitz, L. M., Mori, Y. & Nedergaard, M. The Glymphatic System and
1715 Pain. *Med Acupunct* **32**, 373-376 (2020). <https://doi.org/10.1089/acu.2020.1489>
- 1716 45 Braun, M. & Iliff, J. J. The impact of neurovascular, blood-brain barrier, and glymphatic
1717 dysfunction in neurodegenerative and metabolic diseases. *Int Rev Neurobiol* **154**, 413-
1718 436 (2020). <https://doi.org/10.1016/bs.irn.2020.02.006>
- 1719 46 Gakuba, C. *et al.* General Anesthesia Inhibits the Activity of the "Glymphatic System".
1720 *Theranostics* **8**, 710-722 (2018). <https://doi.org/10.7150/thno.19154>
- 1721 47 Miao, A. *et al.* Brain clearance is reduced during sleep and anesthesia. *Nat Neurosci* **27**,
1722 1046-1050 (2024). <https://doi.org/10.1038/s41593-024-01638-y>
- 1723 48 Kress, B. T. *et al.* Impairment of paravascular clearance pathways in the aging brain. *Ann*
1724 *Neurol* **76**, 845-861 (2014). <https://doi.org/10.1002/ana.24271>
- 1725 49 Wang, M. *et al.* Focal Solute Trapping and Global Glymphatic Pathway Impairment in a
1726 Murine Model of Multiple Microinfarcts. *J Neurosci* **37**, 2870-2877 (2017).
1727 <https://doi.org/10.1523/JNEUROSCI.2112-16.2017>
- 1728 50 Li, M. *et al.* Impaired Glymphatic Function and Pulsation Alterations in a Mouse Model
1729 of Vascular Cognitive Impairment. *Front Aging Neurosci* **13**, 788519 (2021).
1730 <https://doi.org/10.3389/fnagi.2021.788519>

- 1731 51 Xu, Z. *et al.* Deletion of aquaporin-4 in APP/PS1 mice exacerbates brain A β
1732 accumulation and memory deficits. *Mol Neurodegener* **10**, 58 (2015).
1733 <https://doi.org/10.1186/s13024-015-0056-1>
- 1734 52 Simon, M. *et al.* Loss of perivascular aquaporin-4 localization impairs glymphatic
1735 exchange and promotes amyloid β plaque formation in mice. *Alzheimers Res Ther* **14**, 59
1736 (2022). <https://doi.org/10.1186/s13195-022-00999-5>
- 1737 53 Pedersen, T. J., Keil, S. A., Han, W., Wang, M. X. & Iliff, J. J. The effect of aquaporin-4
1738 mis-localization on A β deposition in mice. *Neurobiol Dis* **181**, 106100 (2023).
1739 <https://doi.org/10.1016/j.nbd.2023.106100>
- 1740 54 Burfeind, K. G. *et al.* The effects of noncoding aquaporin-4 single-nucleotide
1741 polymorphisms on cognition and functional progression of Alzheimer's disease.
1742 *Alzheimers Dement (N Y)* **3**, 348-359 (2017). <https://doi.org/10.1016/j.trci.2017.05.001>
- 1743 55 Zeppenfeld, D. M. *et al.* Association of Perivascular Localization of Aquaporin-4 With
1744 Cognition and Alzheimer Disease in Aging Brains. *JAMA Neurol* **74**, 91-99 (2017).
1745 <https://doi.org/10.1001/jamaneurol.2016.4370>
- 1746 56 Simon, M. J. *et al.* Transcriptional network analysis of human astrocytic endfoot genes
1747 reveals region-specific associations with dementia status and tau pathology. *Sci Rep* **8**,
1748 12389 (2018). <https://doi.org/10.1038/s41598-018-30779-x>
- 1749 57 Instrumentation, A. N. S. I. A. f. A. o. M. Vol. EC12:2000/(R)2020 (2020).
- 1750 58 Ayllon, D., Seoane, F. & Gil-Pita, R. Cole equation and parameter estimation from
1751 electrical bioimpedance spectroscopy measurements - A comparative study. *Annu Int*
1752 *Conf IEEE Eng Med Biol Soc* **2009**, 3779-3782 (2009).
1753 <https://doi.org/10.1109/IEMBS.2009.5334494>
- 1754 59 De Lorenzo, A., Andreoli, A., Matthie, J. & Withers, P. Predicting body cell mass with
1755 bioimpedance by using theoretical methods: a technological review. *J Appl Physiol*
1756 (1985) **82**, 1542-1558 (1997). <https://doi.org/10.1152/jappl.1997.82.5.1542>
- 1757 60 Gabriel, S., Lau, R. W. & Gabriel, C. The dielectric properties of biological tissues: III.
1758 Parametric models for the dielectric spectrum of tissues. *Phys Med Biol* **41**, 2271-2293
1759 (1996). <https://doi.org/10.1088/0031-9155/41/11/003>
- 1760 61 Welch, P. The use of the fast Fourier transform for the estimation of power spectra: A
1761 method based on time averaging over short, modified periodograms. *IEEE Trans. Audio*
1762 *Electroacoust* **15**, 70-73 (1967).
- 1763 62 Vallat, R. & Walker, M. P. An open-source, high-performance tool for automated sleep
1764 staging. *Elife* **10** (2021). <https://doi.org/10.7554/eLife.70092>
- 1765 63 Quinn, A. J., Lopes-Dos-Santos, V., Dupret, D., Nobre, A. C. & Woolrich, M. W. EMD:
1766 Empirical Mode Decomposition and Hilbert-Huang Spectral Analyses in Python. *J Open*
1767 *Source Softw* **6** (2021). <https://doi.org/10.21105/joss.02977>
- 1768 64 Heart rate variability: standards of measurement, physiological interpretation and clinical
1769 use. Task Force of the European Society of Cardiology and the North American Society
1770 of Pacing and Electrophysiology. *Circulation* **93**, 1043-1065 (1996).
- 1771 65 Janelidze, S. *et al.* Head-to-Head Comparison of 8 Plasma Amyloid- β 42/40 Assays in
1772 Alzheimer Disease. *JAMA Neurol* **78**, 1375-1382 (2021).
1773 <https://doi.org/10.1001/jamaneurol.2021.3180>
- 1774 66 Roberts, K. F. *et al.* Amyloid- β efflux from the central nervous system into the plasma.
1775 *Ann Neurol* **76**, 837-844 (2014). <https://doi.org/10.1002/ana.24270>

- 1776 67 Liu, H. *et al.* Acute sleep loss decreases CSF-to-blood clearance of Alzheimer's disease
1777 biomarkers. *Alzheimers Dement* (2023). <https://doi.org/10.1002/alz.12930>
- 1778 68 Loh, S., Lamond, N., Dorrian, J., Roach, G. & Dawson, D. The validity of psychomotor
1779 vigilance tasks of less than 10-minute duration. *Behav Res Methods Instrum Comput* **36**,
1780 339-346 (2004). <https://doi.org/10.3758/bf03195580>
- 1781 69 Arsintescu, L. *et al.* Validation of a touchscreen psychomotor vigilance task. *Accid Anal*
1782 *Prev* **126**, 173-176 (2019). <https://doi.org/10.1016/j.aap.2017.11.041>
- 1783 70 Arbuthnott, K. & Frank, J. Trail making test, part B as a measure of executive control:
1784 validation using a set-switching paradigm. *J Clin Exp Neuropsychol* **22**, 518-528 (2000).
1785 [https://doi.org/10.1076/1380-3395\(200008\)22:4;1-0;FT518](https://doi.org/10.1076/1380-3395(200008)22:4;1-0;FT518)
- 1786 71 *Digit Span (DGS)*, <<https://cambridgecognition.com/digit-span-dgs/>> (
1787 72 *PVT Research Tool*, <<https://apps.apple.com/tr/app/pvt-research-tool/id1475726298>> (
1788 73 Smith, A. *Symbol Digit Modalities Test*. (Western Psychological Association, 1992).
1789 74 Reitan, R. *Trail Making Test: Manual for Administration and Scoring*. (1992).
1790 75 Diagnostics, C. N. <<https://c2n.com/>> (
1791 76 Piantino, J. *et al.* Link between Mild Traumatic Brain Injury, Poor Sleep, and Magnetic
1792 Resonance Imaging: Visible Perivascular Spaces in Veterans. *J Neurotrauma* **38**, 2391-
1793 2399 (2021). <https://doi.org/10.1089/neu.2020.7447>
- 1794 77 Boespflug, E. L. *et al.* MR Imaging-based Multimodal Autoidentification of Perivascular
1795 Spaces (mMAPS): Automated Morphologic Segmentation of Enlarged Perivascular
1796 Spaces at Clinical Field Strength. *Radiology* **286**, 632-642 (2018).
1797 <https://doi.org/10.1148/radiol.2017170205>
- 1798 78 Levendovszky, S. R. *et al.* Preliminary cross-sectional investigations into the human
1799 glymphatic system using multiple novel non-contrast MRI methods. *bioRxiv* (2023).
1800 <https://doi.org/10.1101/2023.08.28.555150>
- 1801 79 Ohene, Y. *et al.* Non-invasive MRI of brain clearance pathways using multiple echo time
1802 arterial spin labelling: an aquaporin-4 study. *Neuroimage* **188**, 515-523 (2019).
1803 <https://doi.org/10.1016/j.neuroimage.2018.12.026>
- 1804 80 Fultz, N. E. *et al.* Coupled electrophysiological, hemodynamic, and cerebrospinal fluid
1805 oscillations in human sleep. *Science* **366**, 628-631 (2019).
1806 <https://doi.org/10.1126/science.aax5440>
- 1807 81 Fong, Y., Huang, Y., Gilbert, P. B. & Permar, S. R. chngpt: threshold regression model
1808 estimation and inference. *BMC Bioinformatics* **18**, 454 (2017).
1809 <https://doi.org/10.1186/s12859-017-1863-x>
- 1810 82 Fong, Y., Di, C. & Permar, S. Change point testing in logistic regression models with
1811 interaction term. *Stat Med* **34**, 1483-1494 (2015). <https://doi.org/10.1002/sim.6419>
- 1812 83 Farokhian, F., Yang, C., Beheshti, I., Matsuda, H. & Wu, S. Age-Related Gray and White
1813 Matter Changes in Normal Adult Brains. *Aging Dis* **8**, 899-909 (2017).
1814 <https://doi.org/10.14336/AD.2017.0502>
- 1815 84 Ding, F. *et al.* Changes in the composition of brain interstitial ions control the sleep-wake
1816 cycle. *Science* **352**, 550-555 (2016). <https://doi.org/10.1126/science.aad4821>
- 1817 85 Sun, Y. & Sun, X. Exploring the interstitial system in the brain: the last mile of drug
1818 delivery. *Rev Neurosci* **32**, 363-377 (2021). <https://doi.org/10.1515/revneuro-2020-0057>
- 1819 86 Hotelling, H. New light on the correlation coefficient and its transforms. *Journal of the*
1820 *Royal Statistical Society. Series B (Methodological)* **15.2**, 193-232 (1953).
1821